Fall 12-28-2015

Amyloid Proteins Structure, Dynamics, Interactions and Early Stages of Self-Assembly

Yuliang Zhang
University of Nebraska Medical Center

AMYLOID PROTEINS STRUCTURE, DYNAMICS, INTERACTIONS AND EARLY STAGES OF SELF-ASSEMBLY

by
Yuliang Zhang

A DISSERTATION

Presented to the Faculty of
the University of Nebraska Graduate College
in Partial Fulfillment of the Requirements
for the Degree of Doctor of Philosophy

Department of Pharmaceutical Sciences

Under the Supervision of Professor Yuri L. Lyubchenko

University of Nebraska Medical Center

Omaha, Nebraska

August, 2015

Supervisory Committee:

Howard E. Gendelman, Ph.D.
Jonathan L. Vennerstrom, Ph.D.
Sorin Luca, Ph.D.
Sándor, Lovas, Ph.D.

TABLE OF CONTENTS

ACKNOWLEDGEMENTS

I would like to acknowledge my advisor, Dr. Yuri Lyubchenko, for his mentorship and counseling through my graduate study. I really appreciate that he not only provided the opportunity for me to work in his lab but also offered the finical support to help me finish my four year PhD project. Originally, I worked in his lab as technician. Two years later, he encouraged me to apply for the Pharmaceutical Sciences Graduate Program at our University. At the beginning of the PhD study, my work was mainly focused on the characterization of the interaction of short amyloid fragments using Atomic Force Microscopy (AFM) based single molecular force spectroscopy. In order to obtain the detailed information of such structures, Dr. Lyubchenko sent me to Dr. Sandor Lovas' lab to learn about Molecular Dynamics (MD) simulation. In addition to this, Dr. Lyubchenko also made it possible for me to attend several conferences and workshops, including Biophysical Society Annual meeting, Single Molecule Biophysics Conference in Aspen city, Theoretical and Computational Biophysics Group workshop in Dr. Klaus Schulten's lab, and an Anton Workshop at the Pittsburgh Supercomputing Center as well as many more. From these conferences and workshops, I have learned a considerable amount of novel material and have communicated with many talented Scientists. These activities are beneficial for developing both my academic and professional future. Most importantly, with Dr. Lyubchenko's help, I received a Postdoc job position provided by the University of California, Davis and Lawrence Livermore National Laboratory.

I would also like to give a sincere thanks to all of the Committee members: Dr. Howard E. Gendelman, Dr. Jonathan L. Vennerstrom, Dr. Sorin Luca, and Dr. Sándor

Lovas. During our Committee meetings, they always had great patience and provided me with valuable advice which helped me to fulfill my PhD project smoothly. In particular, Dr. Sándor Lovas taught me how to perform MD simulations under Linux system and generously provided their labs computer cluster to help finish the project. Without Dr. Lovas's help, I couldn't have finished any MD simulations and thus this help allowed me to continue on with further studies. Dr. Gendelman always attempted to attend my Committee meeting even though he had the busy schedule. He and Dr. Sorin Luca also taught the first year class in which I really enjoyed their teaching style. On top of the mentioned help, Dr. Vennerstrom also shared the skating experience on our University ice rink, thereby contributing to my memories of the wonderful winter time in Omaha.

I also want to express my extreme appreciation to our the past and present lab members: Dr. Lyudmila S Shlyakhtenko, Dr. Junping Yu, Dr. Alexey Krasnoslobodtsev, Dr. Alexander Lushnikov, Dr. Alex Portillo, Dr. Zhengjian Lv, Dr. Zhiqiang Sun, Dr. Sibaprasad Maity, Mohtadin Hashemi, and Micah P Stumme-Diers. It is delightful to have their help in both lab life and discussions and it is has been my honor to spend many years with them. I would like to give a special thanks to Dr. Junping Yu, who was from the same lab as me in China. Dr. Yu and her family picked me up from the Eppley Airfield in the midnight when I first arrived at Omaha City. Her family always helped me immensely when I was in trouble.

Tremendous thanks for all the current and former faculty members and students in our Graduate Office and our Department for their patience and help through my four years of PhD study. Particularly, I would like to acknowledge Mrs. Katina M Winters and

Mr. Cody R Phillips for their assistance. Without their help, I could not have finished the scheduling for my Comprehensive Exam and my Final Defense.

I am grateful towards Dr. Dittrich and his colleagues at Pittsburg Supercomputing Center (PSC) for training on Anton supercomputer and advice; Dr. Schulten for the VMD software package and Dr. Swanson for advice in regard to the use University computer cluster.

The simulations in this dissertation were performed using the Cluster in Dr. Lovas' lab, our University facility—Holland Computing Center (HCC), the Texas Advanced Computing Center (TACC), at the University of Texas at Austin, and the Anton supercomputer in Pittsburg Supercomputing Center (PSC).

Finally, I would like to dedicate my PhD work, including this dissertation, to my parents and my brother for their consistent support. I would also like to thank all of my relatives for their encouragement.

Some passages in this dissertation have been quoted verbatim from the following sources with permission:

The chapter 2 is quoted from the source "Lovas, S., Zhang, Y., Yu, J. & Lyubchenko, Y.L. Molecular Mechanism of Misfolding and Aggregation of Aβ(13–23). The Journal of Physical Chemistry B 117, 6175-6186 (2013)." with permission.

The chapter 3 is reformatted from our published paper "Zhang, Y. and Lyubchenko, Y.L. The Structure of Misfolded Amyloidogenic Dimers: Computational

Analysis of Force Spectroscopy Data. Biophysical Journal 107, 2903-2910 (2014). ” with permission.

AMYLOID PROTEINS STRUCTURE, DYNAMICS, INTERACTIONS AND EARLY STAGES OF SELF-ASSEMBLY

Yuliang Zhang, Ph.D.

University of Nebraska Medical Center, 2015

Supervisor: Yuri L Lyubchenko, Ph.D.

The self-assembly and aggregation of amyloid protein are associated with several neurodegenerative diseases. The evidence indicates that the oligomeric intermediates, formed prior to the final fibrillary product, are the primary culprits of neurotoxicity. Although tremendous efforts have been dedicated for the characterization of structures, dynamics and toxic-related hallmarks of the oligomers, to date, yet the mechanism of such assembly from disordered monomers and their structure remain elusive.

In this dissertation, I focused on understanding the dimerization process of amyloid proteins and peptides of different sizes and I combined experimental studies with high-power computer simulations. The AFM force spectroscopy experiments showed that within dimers misfolded states of peptides were characterized by a lifetime as large as ~1 s. Compared with the conformational dynamics of monomers, dimerization stabilized the misfolded states by many orders of magnitude. To characterize structure of the dimers, the all-atom Molecular Dynamics (MD) simulations were employed. These MD simulations indeed revealed the stabilization of dimers when they form antiparallel of β-sheet conformation. The hydrogen bonds, salt bridges, and weakly polar interactions further stabilized the dimer structure. The simulations led to several structures, so to distinguish between them and identify the one that was observed in the experiment, a novel computational approach termed Monte Carlo Pulling (MCP) was developed. The

key property of this approach is the ability to simulate the AFM force spectroscopy experiment at conditions identical ones used in the experiment enabling us to identify the appropriate computational model of the dimer by direct comparison with the AFM experiment. A comparison of experimental results with the computational data for two amyloid peptides allowed us for the first time to identify the dimers analyzed in the experiment and characterize their structure. These studies demonstrated that although hydrogen bonds were the major contributors to dimer dissociation, the aromatic-aromatic interaction also contributed to the dimer rupture process. Entirely unexpected results were obtained in the application of this combined approach to characterization of dimers formed by full-size Aβ42 dimers. The dimers were stabilized primarily by interactions within the central hydrophobic regions and C-terminal region with a contribution from local hydrogen bonding. The dimers were dynamic as evidenced by the existence of a set of conformations and computational analyses of the dimer dissociation process. Although Aβ42 protein formed stable dimers, but their structure was entirely different from the ones reported for the Aβ42 protein in fibrils. In fact a set of structures was identified and we hypothesize that different structures can be nuclei for the Aβ42 assembly in different morphologies. To characterize dimerization of such large amyloid protein as α-Synuclein (α-Syn) (140 residues), a novel combined approach was utilized. The structure and dynamics of the dimers was characterized by high-speed AFM and Monte Carlo modeling was used to characterize the protein structure. These studies showed that the hydrophobic region of α-Syn facilitated the formation of compact structures. Surprisingly, the dynamics of one α-Syn dimers shared a number of similar features with the dissociation process in Aβ42 simulations.

Altogether, our results revealed structure of transiently existing dimeric forms of amyloid proteins. Given the fact that the dimers are the very first oligomers of amyloids, this novel information is indispensable drug design activity and development of novel therapeutic tools for early diagnostic of AD and PD and opens prospects for understanding molecular mechanisms of early onset of AD and PD and development of the preventive means for these devastating diseases.

LIST OF FIGURES

LIST OF TABLES

LIST OF ABBREVIATIONS

Aβ	Amyloid β
AD	Alzheimer's disease
AFM	Atomic force microscopy
aMD	Accelerated Molecular Dynamics
APP	Amyloid precursor protein
APS	Aminopropyl Silatrane
Ar	Aromatic
α-Syn	α-Synuclein
cMD	Conventional Molecular Dynamics
BBB	Blood–brain barrier
CD	Circular Dichroism
COM	Center of mass
DFS	Dynamics force spectroscopy
DMD	Discrete Molecular Dynamics
DMSO	Dmethyl sulfoxide
dPCA	Dihedral principle component analysis
DSSP	Defined secondary structure of protein
EM	Electron microscopy
EGCG	Epigallocatechin-3-gallate
HD	Huntington's disease
HEPES	4-(2-hydroxyethyl)-1-piperazineethanesulfonic acid
HFIP	Hexafluoroisopropanol
HS-AFM	High-speed atomic force microscopy

IDP	Intrinsically disordered protein
MAL-PEG-SVA	Maleimidepolyethylene glycol-succinimidyl valerate
MAS	Maleimide Silatrane
MD	Molecular Dynamics
MC	Monte Carlo
MCP	Monte Carlo pulling
NMR	Nuclear magnetic resonance
NQTrp	1,4-naphthoquinon-2-yl-$_L$-tryptophan
PD	Parkinson's disease
PDB	Protein Data Bank
PDF	Probability density function
PME	Particle-mesh Ewald
PMF	Potential of Mean Force
REMD	Replica Exchange Molecular Dynamics
Rg	Radius of gyration
RMSD	Root-mean-square deviation
RMSIP	Root-mean-square inner product
SMD	Steered Molecular Dynamics
TCEP	Tris (2-carboxyethyl) phosphine
WHAM	Weighted Histogram Analysis Method

LIST OF CONTRIBUTORS

1. In Chapter 2, Dr. Sándor Lovas and Dr. Yuri Lyubchenko and Yuliang Zhang conceived and designed the project. Yuliang Zhang collected AFM imaging and performed all the MD simulations and analysis using the computer cluster in Dr. Sándor Lovas's lab. Dr. Junping Yu did force spectroscopy measurement and finished the analysis with Yuliang Zhang.
2. In Chapter 3, Yuliang Zhang implemented all the simulations in HCC cluster and finished the data analysis. Yuliang Zhang and Dr. Yuri Lyubchenko conceived and designed the project. Dr. Sándor Lovas guided the REMD simulation of Sup35 fragments.
3. In Chapter 4, Yuliang Zhang, Mohtadin Hashemi, Dr. Zhengjian Lv and Dr. Yuri Lyubchenko conceived and designed the overall studies. Yuliang Zhang performed all the simulations and analyzed the simulation data using HCC cluster, Stampede cluster and specialized supercomputer—Anton. Mohtadin Hashemi contributed to the Monte Carlo pulling simulations. Zhengjian Lv performed the analysis of experimental dataset. All the authors discussed the results and wrote the paper.
4. In Chapter 5, Yuliang Zhang performed the HS-AFM experiments as well as MC modeling using HCC cluster. Dr. Zhenjian Lv prepared the α-Synuclein samples.
5. All the chapters were written by Yuliang Zhang. Overall, the project was designed and guided by Dr. Yuri Lyubchenko.

6. The works were supported by NIH grants GM096039 and GM100156, NSF grant EPS–004094, DE-FG02-08ER64579 (DOE) and PSCA14025P award for the Anton computer use to YLL and NIH grants 5P20RR016469 and 8P20GM103427 to SL.

Chapter 1

INTRODUCTION

The aberrant self-assembly of amyloid protein is implicated in several fatal neurodegenerative diseases, including Alzheimer's disease (AD), Parkinson's disease (PD), Huntington's disease (HD) [1, 2]. In the case of AD, the protein is the amyloid β (Aβ) protein, in PD it is α-Synuclein (α-Syn) and in HD it is huntingtin protein containing poly-L-glutamine (Poly-Q) tracts and in this case the protein aggregation depends on the number of glutamine residues. These diseases have a tremendous impact on human health; for instance, it has been appraised that AD alone could affect approximately 5 million people in the US in 2015 (Figure 1.1A), while in 2050 the number of AD patients will exceed 13 million based on the current trend [3]. The annual costs of care of Americans who suffer from AD and other dementias are extremely high (~$226 billion in 2015 and ~$1.1 trillion in 2050) as shown in Figure 1.1B. Unfortunately, there is currently no cure for this kind of diseases. The major reason for this is that the mechanism of self-assembly of amyloid proteins remains elusive, resulting in a lack of efficient approaches that can be utilized for inhibition of the self-assembly. Therefore, the understanding of how the amyloid aggregates assembly and cause the disease is critical for the curing, prevention and eradication of these diseases. Recent data has shown that oligomers rather than large aggregates, such as fibrils widely studied so far, have neurotoxic effects but very little is known about their structure and assembly. In this chapter, we will review the progress of research of amyloid aggregation in regard to their

structures, interaction patterns, dynamics, and kinetics, as well as approaches known to alleviate the neurotoxicity of amyloid aggregations.

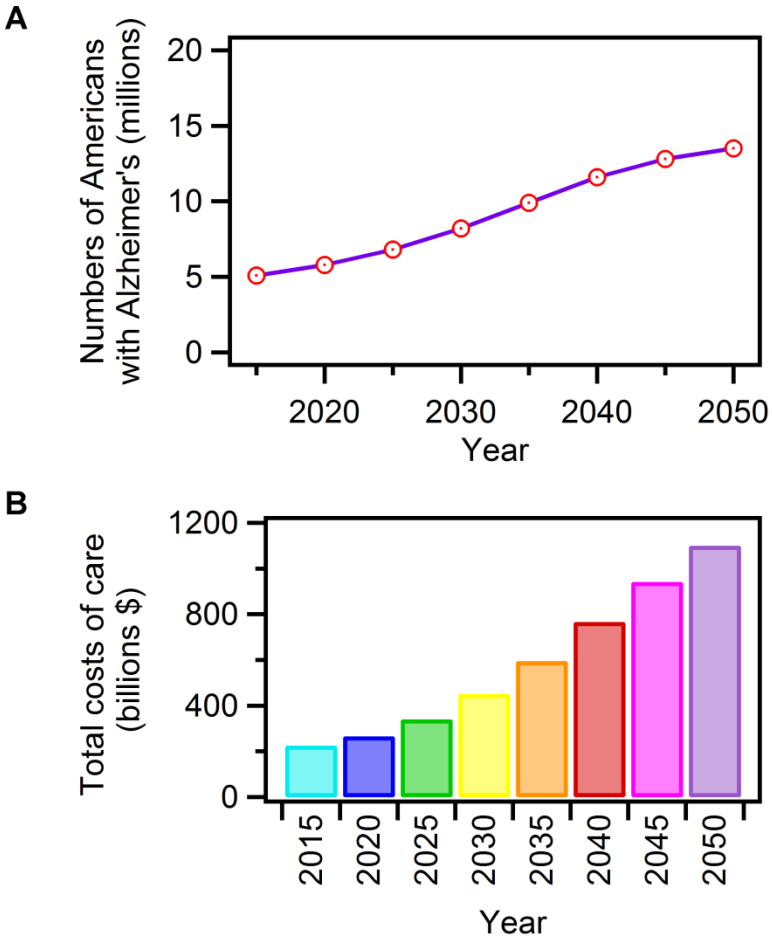

Figure 1.1. The estimated of number of Americans with Alzheimer's disease (**A**) and the annual costs of care (**B**) from 2015 to 2050. The source of this data is ref. [3].

1.1 Molecular basis of amyloid assembly

1.1.1 Amyloid fibril

Generally, the self-assembly process takes place from the natively disordered monomeric state of these amyloid proteins through a transient oligomeric state (Figure 1.2) to highly ordered fibrillar aggregates termed as amyloid fibrils. These amyloid fibrils are the major component of amyloid plaques and Lewy bodies, which are the hallmarks of AD and PD, respectively. Given their structural stability, these fibrils have been well characterized structurally by traditional approaches, such as NMR [4-11], X-ray crystallography [12, 13], AFM [14-18] and EM [11, 14, 19]. Based on these studies, the model with a cross β pattern, in which the β-strands are perpendicular to the long axis of fibril, has been proposed. The parallel orientation is prevalent in the consecutive monomers with an intermolecular distance of ~ 4.8 Å, thus indicating that the parallel orientation is prevalent in the consecutive monomers [13, 20]. However, the orientation of the β-sheet is sequence dependent and may vary from parallel to anti-parallel manners [21]. Meanwhile, the morphology of fibrils is environment dependent, so the fibrils with various overall geometries, such as a U-shape [9], S-shape [4], or triangular shape [22, 23], can allow for even more complex structures to be assembled [24]. Although the majority of structural studies were carried out with assemblies obtained *in vitro*, a structurally similar sample has been extracted from brain tissues [25], thereby suggesting that amyloid aggregates exist in the brain. Not dependent on the fibril's shape, hydrogen bonds formed between adjacent monomers are a general structural feature with electrostatic and hydrophobic interactions also crucial for the thermal and mechanical stability of the fibril. Given the dramatic difference seen in the structure of monomers in

their free state as opposed to in fibrils, it can be assumed that monomers undergo structural transitions during assembly into aggregates; a process that has been confirmed in Molecular Dynamics (MD) simulations termed “dock-lock” mechanism [26-32].

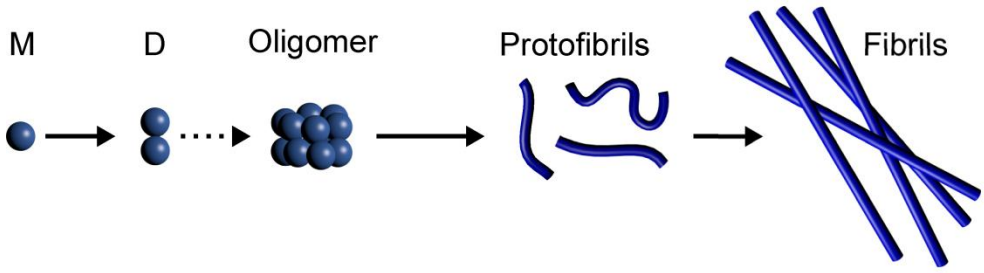

Figure 1.2. The schematic diagram of the self-assembly process for Aβ proteins (adapted from Ref. [33])

1.1.2 Amyloid oligomer

Unlike fibrils, the structures of amyloid oligomers are unknown. Various morphologies have been suggested, including a spherical shape, hollow core oligomer and protofibril structure [34-38]. Prior to forming the final aggregation product, the monomers are assembled in oligomeric intermediates; a nucleated polymerization hypothesis has been proposed to explain the formation of such intermediates [39-46]. According to this hypothesis, the monomers undergo several structural transitions [47] to form a critical oligomeric nucleus followed by the formation of a protofibril, finally resulting fibril formation. Experimentally, Congo red or ThT fluorophores can be utilized to monitor the kinetics of amyloid aggregation and fibril growth; but more importantly, this intensive experimental data proved that amyloid oligomers, including dimers [48, 49] rather than fibrils, are mostly neurotoxic [50-55]. This suggested that the amyloid's secondary structure in oligomers is different from that for fibrils, with the aggregation pathway also considerably different [56]. This assumption is further supported by characterization of oligomers by use of spectroscopic techniques [54, 57, 58] which showed that changes occur at early aggregation states; however, yet to be found is the extensive formation of β-structures. Until now, the neurotoxic oligomers have been accepted as adopting an anti-parallel β-sheet structure with different patterns [55, 59-62]. Nevertheless, due to transient and heterogeneous nature of amyloid protein together with being prone to rapid aggregation, it is still unrealistic to isolate specific aggregation species for their structural studies. A photo cross-linking methodology developed in ref. [52], allowed the authors to isolate individual oligomers for their structural characterization with Circular Dichroism (CD), but effect of the photo cross-linking

procedure on the oligomer's native structure is a big concern. Consequently, the question about how the amyloid structures are different in oligomers of different kinds and what amyloid structures are responsible for the neurotoxicity remained unclear. As discussed below, several hypothesis exist suggesting the toxicity of the oligomeric state.

1.2 Plausible mechanism of toxicity induced by amyloid oligomer

It was proposed that the cytotoxicity of extracellular amyloid oligomers is membrane-related [63, 64]. Indeed, it has been found that amyloid proteins have the potential to interact with the neuronal cell membrane [63, 64]. When accumulating on the cell membrane, the amyloid proteins can form pore like oligomers [65, 66]; subsequently, these pore like structures can serve as a "channel" to change the homeostasis of calcium or other ions [67], thereby accelerating the degenerative processes. Another study pointed out that the cytotoxicity of amyloid oligomers derived from the elevated membrane conductance of lipid bilayer rather than from the formation of nano-pores [38]. A prevalent perspective on this mechanism considers that the binding of extracellular amyloid oligomers to the neuronal cell surface exerts the effect on a number of receptors, thus resulting in synaptic dysfunction and neurodegeneration [68-70]. In addition to the impairment from extracellular amyloid oligomers, there are studies which suggest that intracellular amyloid protein does exist in neuronal cell [71], so the intracellular oligomers can induce the cell death as well [70]. The accumulation of intracellular amyloid protein is governed by cellular proteins; however, the formation and toxicity mechanism of these intracellular amyloid oligomers is still not well understood.

It is proposed that the oligomers are potent to inhibit proteasome activity *in vitro*, causing subsequent cell death [70, 72].

1.3 The inhibition strategies of the self-assembly and the toxicity

Although, the mechanism of the self-assembly of amyloid proteins is not clear, several inhibition strategies have been applied. One possible way to prevent the self-assembly is to prevent the production of amyloid protein monomers. For example, in AD case the monomeric Aβ is produced via sequentially cleaved β and γ secretases on the amyloid precursor protein (APP) which is then released from the cell membrane [73-75]. With this in mind, intervention of β and γ secretases activities may be beneficial to prevent further assembly. Another strategy is to design an inhibitor to break the β-sheet, which is the predominant conformation in fibrils. Usually, the self-recognition motif, for instance the KLVFF region of Aβ protein [76] and 113-120 region of large amyloid protein−prion protein [77], are exploited as β-sheet breakers; these breakers can either bind to the monomers or attach to the end of fibrils to prevent the elongation. A significant downside to this method is that the enzymes always have the other functions, thus limiting their specificity. Meanwhile, the role that the monomers play *in vivo* are also still not well understood. One suggested functional role of the α-Syn protein is attributed to the regulation of dopamine neurotransmission [78]. Because of this, inhibition of enzymes and deletion of amyloid monomers may give rise to undesirable side-effects.

The oligomers, as described in section 1.2, display elevated neurotoxicity, compared to the amyloid fibril. Therefore, they can also be used as a potent target for drug design. In fact, conformation dependent antibodies and chaperones have been used

to alleviate the toxicity of oligomeric species [79]. The amyloid monomers are unstructured or partially folded [80-82] which then poses the question of how the self-assembly and conformational transition occur at the intermediate oligomer state (Figure 1.3). The self-assembly is a kinetic process during which oligomers of various sizes are formed, so understanding the self-assembly process requires experimental methods capable of characterizing these transient species in the aggregation reaction. Developing two methods that address this is the major goal of this dissertation as described in detail below.

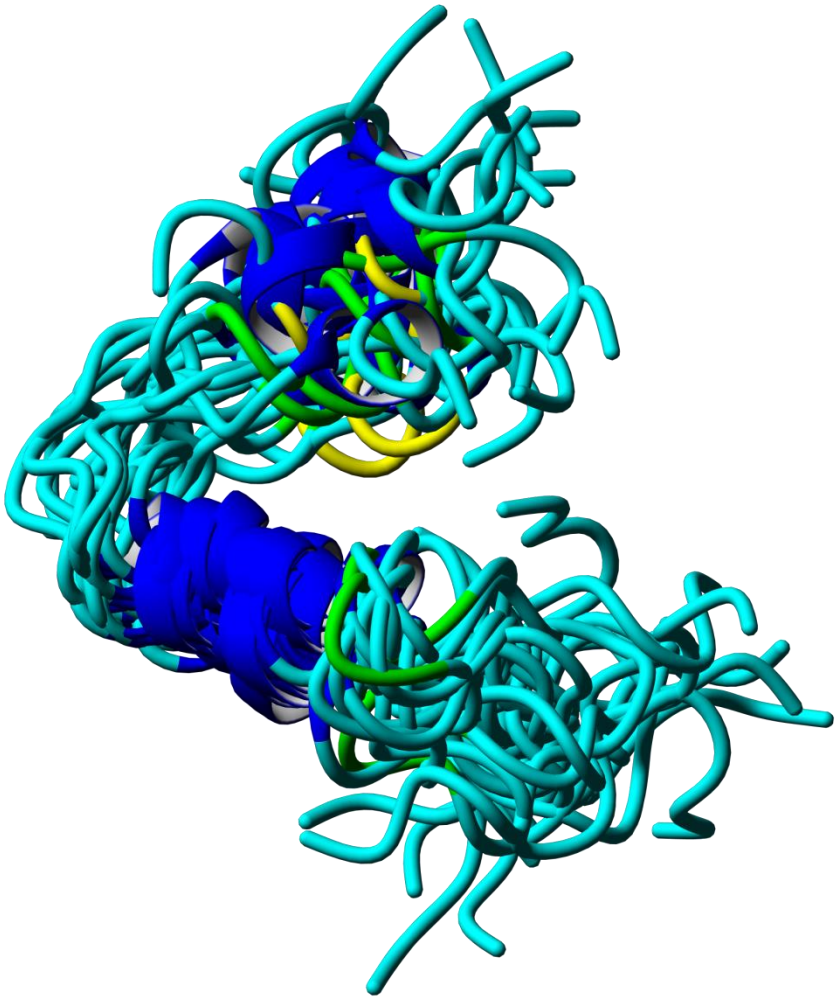

Figure 1.3. Model of 20 copies of partial folded Aβ40 in aqueous solution (PDB ID: 2LFM, adapted from ref. [82]). The blue regions indicate folded regions with blue presenting α-helices, cyan is random coil and yellow, β-turns.

1.4 The approaches exploited for Amyloid protein monomer interaction

1.4.1 AFM based approaches

AFM, conceived by Binnig and Rohrer [83], is a powerful tool for the morphological study of protein misfolding and aggregation [14-18]. A major limiting factor in the use of conventional AFM is the scan which is much too slow to capture the structural transition of biological samples. In order to overcome this issue, a recently developed approach called high-speed AFM (HS-AFM) is capable of acquiring images at tremendous rate, thereby allowing for videos of the structural transitions; additionally HS-AFM has been proven suitable for exploring various biological systems (detailed description in the review [84]) and it has been successfully used in the visualization of the dynamics of myosin V [85], F1–ATPase [86], nucleosomes [87] and intrinsically disordered proteins (IDP) [88, 89]. There are number of key advantages associated with the use of HS-AFM [84]: (1) The high scan rate; rates of 16 frames per second (fps) have been reported, which is about 1000 times faster than possible with a conventional AFM. (2) The interaction between the tip and sample is minimized (the force <100 pN is applied), and their interaction is also shortened as a result of the high oscillation frequency (~1.6 MHz). (3) The tips are sharpened giving them a radius of curvature as small as ~ 1 nm which allows for nanometer range resolution while imaging in aqueous solution. Together, these characteristics allow for the analysis of the self-assembly process of amyloid proteins in a manor never before possible.

In addition to imaging, the AFM can be used in the analysis of the mechanical properties (Young's modulus) of amyloid aggregates [17, 90-92]. The mature fibril exhibits remarkable mechanical properties as is evident by Young's modulus value of 2.2

GPa. The rigidities are mainly from the intermolecular hydrogen bond networks [17]. For comparison, the Young's modulus of Aβ42 oligomers is 1.5 GPa, which is smaller than the result from fibrils [91].

We have recently developed a technique for probing amyloid dimers based on measuring the interaction of amyloid monomers using AFM force spectroscopy [93-101]. In this approach, monomers were end-immobilized on both the AFM tip and the surface, and the interaction between them was then measured by approaching the tip to the surface, to allow the dimers to form, and the subsequent retraction step, which allowed us to measure the rupture force required to dissociate the dimer. The application of this methodology to amyloid proteins has allowed us not only to measure the strength of interaction between the monomers in the dimeric species, but also to evaluate the lifetime of each of the formed dimers [94-97, 102]. The lifetime values were found to be in the range of seconds, suggesting that dimerization undergoes a structural transition from unstructured monomers to stable complexes [94-97, 102]. Additionally, the contour length derived from AFM force spectroscopy experiments, provides valuble information on the location of interacting segments within the dimers [97-99, 103-105].

1.4.2 Computer Simulations

The AFM based force spectroscopy method is critical to these studies but it lacks the capacity to structurally characterize Computational approaches including MD and MC simulations have been used to predict the structure and dynamics information of amyloid protein, thus complimenting the AFM studies well. An example of the power of these computational approaches is that the MD or MC simulations have been used to gain

the structural information of Aβ42 dimers [106-111]. Taking advantage of discrete MD (DMD) simulation, Urbanc, B. *et al.* found Aβ42 dimers are populated by the planar conformations according to characteristics of β-stands orientations [106]. Later, utilizing MC simulations, Mitternacht, and co-workers proved that dimers with an intermolecular β-sheet are relatively rare [107]. Instead, the intramolecular antiparallel β-sheet, rather than the architecture of intermolecular parallel β-sheet in fibrils, is the main secondary structural component. Zhu *et al.* identified dimers consisting of high content of α-helix and the structures containing parallel as well as antiparallel β-sheet [111]. The replica exchange MD (REMD) method, an efficient method to enhance the exploration of all the possible conformational space of protein, has also been used to predict the Aβ42 dimerization [109]. Together these results of Aβ42 structure demonstrated that the dimers are mixtures of intermolecular antiparallel β-sheet and α-helix structures. A difficulty of the MD simulations is that they require validation along with other factors such as the dependence of the results on the initial structure, force field, solvent model and the need of long simulation time. Even in case of Aβ42 protein, the tremendous number of atoms complicates direct simulation of the dimer, so the current data is limited to short time scale conventional all-atom MD simulations in explicit solvent. Barz and Urbanc also pointed out that it is impossible to glean the full description of entire conformational ensembles of Aβ dimers due to their intrinsically disordered nature [108].

In regards to the validation of simulated models, comparing of AFM force spectroscopy results with MD simulation is considered as a useful approach [112-116]. In Steered Molecular Dynamics (SMD) simulations, an external force is applied to classic

molecular dynamics (MD) simulations which allows for the modeling of AFM pulling experiments. A major problem with this approach is that SMD is typically performed at pulling rates of 5 nm/ns, which are 10^7 times higher than those used in typical AFM experiments [102, 117], thereby complicating a direct comparison between *in silico* data and the experimental results [118]. In a recent publication, high-speed AFM instrumentation used in experimental conditions approached the SMD temporal range [119], but the approach is still at the development stage and the pulling speed range is well above the experimentally relevant conditions.

Recently, the all-atom Monte Carlo Pulling (MCP) approach was described which allowed for modeling at rates comparable to regular AFM pulling experiments (pulling rate ~300 nm/s) [120]. The authors were able to directly compare their results with AFM experiments for the characterization the intramolecular interaction strength within Aβ and α-Syn monomers, respectively. Based on these recent advances, we developed a validation approach enabling us to select the most appropriate model form a set of simulations (ref. [121], see also chapter 3).

In this dissertation, we combined the AFM approaches with the computer simulations to elucidate the mechanism of dimerization for the different length of amyloid peptides and proteins. The works are outlined as follows:

Chapter 2 is from the published manuscript in *The Journal of Physical Chemistry B* titled "Molecular Mechanism of Misfolding and Aggregation of Aβ(13–23)". The paper described the self-assembly of short fragment of Aβ via the combination of AFM force spectroscopy and MD simulations.

Chapter 3 is from the published manuscript in *Biophysical Journal* titled "The Structure of Misfolded Amyloidogenic Dimers: Computational Analysis of Force Spectroscopy Data". In this paper, a novel MC pulling (MC) simulation approach has been developed to validate the simulated structure of Amyloid peptides by comparing to the experimental data.

Chapter 4 is a submitted manuscript of my work. In this chapter, long time-scale MD simulations via specialized supercomputer Anton as well as accelerated MD were applied to predict the dimerization of full-length Aβ42. The application of MCP approach allowed us to identify models of Aβ42 dimers and describe their dynamics.

Chapter 5 describes recent data on analysis of structural dynamics of α-Syn using HS-AFM and computational modeling. The paper is in preparation.

Chapter 6 is the conclusion of all works.

REFERENCES

[1] Dobson, C. M. 2003. Protein folding and misfolding. Nature. 426:884-890.

[2] Chiti, F., and C. M. Dobson. 2006. Protein misfolding, functional amyloid, and human disease. Annu. Rev. Biochem. 75:333-366.

[3] http://www.alz.org/alzheimers_disease_trajectory.asp.

[4] Xiao, Y., B. Ma, D. McElheny, S. Parthasarathy, F. Long, M. Hoshi, R. Nussinov, and Y. Ishii. 2015. Aβ(1-42) fibril structure illuminates self-recognition and replication of amyloid in Alzheimer's disease. Nat. Struct. Mol. Biol. 22:499–505.

[5] Colvin, M. T., R. Silvers, B. Frohm, Y. Su, S. Linse, and R. G. Griffin. 2015. High Resolution Structural Characterization of Aβ42 Amyloid Fibrils by Magic Angle Spinning NMR. J. Am. Chem. Soc. 137:7509–7518.

[6] Qiang, W., W. M. Yau, Y. Luo, M. P. Mattson, and R. Tycko. 2012. Antiparallel beta-sheet architecture in Iowa-mutant beta-amyloid fibrils. Proc. Natl. Acad. Sci. USA. 109:4443-4448.

[7] Cobb, N. J., and W. K. Surewicz. 2007. Prion strains under the magnifying glass. Nat. Struct. Mol. Biol. 14:882-884.

[8] Olofsson, A., A. E. Sauer-Eriksson, and A. Öhman. 2006. The Solvent Protection of Alzheimer Amyloid-β-(1–42) Fibrils as Determined by Solution NMR Spectroscopy. J. Biol. Chem. 281:477-483.

[9] Lührs, T., C. Ritter, M. Adrian, D. Riek-Loher, B. Bohrmann, H. Döbeli, D. Schubert, and R. Riek. 2005. 3D structure of Alzheimer's amyloid-β(1–42) fibrils. Proc. Natl. Acad. Sci. USA. 102:17342-17347.

[10] Heise, H., W. Hoyer, S. Becker, O. C. Andronesi, D. Riedel, and M. Baldus. 2005. Molecular-level secondary structure, polymorphism, and dynamics of full-length α-synuclein fibrils studied by solid-state NMR. Proc. Natl. Acad. Sci. USA. 102:15871-15876.

[11] Antzutkin, O. N., R. D. Leapman, J. J. Balbach, and R. Tycko. 2002. Supramolecular structural constraints on Alzheimer's beta-amyloid fibrils from electron microscopy and solid-state nuclear magnetic resonance. Biochemistry. 41:15436-15450.

[12] Perutz, M. F., J. T. Finch, J. Berriman, and A. Lesk. 2002. Amyloid fibers are water-filled nanotubes. Proc. Natl. Acad. Sci. USA. 99:5591-5595.

[13] Nelson, R., M. R. Sawaya, M. Balbirnie, A. O. Madsen, C. Riekel, R. Grothe, and D. Eisenberg. 2005. Structure of the cross-beta spine of amyloid-like fibrils. Nature. 435:773-778.

[14] Conway, K. A., J. D. Harper, and P. T. Lansbury. 2000. Fibrils Formed in Vitro from α-Synuclein and Two Mutant Forms Linked to Parkinson's Disease are Typical Amyloid†. Biochemistry. 39:2552-2563.

[15] Lyubchenko, Y. L., S. Sherman, L. S. Shlyakhtenko, and V. N. Uversky. 2006. Nanoimaging for protein misfolding and related diseases. J. Cell Biochem. 99:52-70.

[16] Hoyer, W., D. Cherny, V. Subramaniam, and T. M. Jovin. 2004. Rapid Self-assembly of α-Synuclein Observed by In Situ Atomic Force Microscopy. J. Mol. Biol. 340:127-139.

[17] Knowles, T. P., A. W. Fitzpatrick, S. Meehan, H. R. Mott, M. Vendruscolo, C. M. Dobson, and M. E. Welland. 2007. Role of intermolecular forces in defining material properties of protein nanofibrils. Science. 318:1900-1903.

[18] Adamcik, J., J.-M. Jung, J. Flakowski, P. De Los Rios, G. Dietler, and R. Mezzenga. 2010. Understanding amyloid aggregation by statistical analysis of atomic force microscopy images. Nat. Nanotechnol. 5:423-428.

[19] Uversky, V. N., J. Li, and A. L. Fink. 2001. Evidence for a partially folded intermediate in alpha-synuclein fibril formation. J. Biol. Chem. 276:10737-10744.

[20] Balbach, J. J., A. T. Petkova, N. A. Oyler, O. N. Antzutkin, D. J. Gordon, S. C. Meredith, and R. Tycko. 2002. Supramolecular Structure in Full-Length Alzheimer's β-

Amyloid Fibrils: Evidence for a Parallel β-Sheet Organization from Solid-State Nuclear Magnetic Resonance. Biophys. J. 83:1205-1216.

[21] Gordon, D. J., J. J. Balbach, R. Tycko, and S. C. Meredith. 2004. Increasing the Amphiphilicity of an Amyloidogenic Peptide Changes the β-Sheet Structure in the Fibrils from Antiparallel to Parallel. Biophys. J. 86:428-434.

[22] Paravastu, A. K., R. D. Leapman, W. M. Yau, and R. Tycko. 2008. Molecular structural basis for polymorphism in Alzheimer's beta-amyloid fibrils. Proc. Natl. Acad. Sci. USA. 105:18349-18354.

[23] Tycko, R., and R. B. Wickner. 2013. Molecular structures of amyloid and prion fibrils: consensus versus controversy. Acc. Chem. Res. 46:1487-1496.

[24] Meier, B. H., and A. Böckmann. 2015. The structure of fibrils from ‘misfolded’ proteins. Curr. Opin. Struc. Biol. 30:43-49.

[25] Lu, J. X., W. Qiang, W. M. Yau, C. D. Schwieters, S. C. Meredith, and R. Tycko. 2013. Molecular Structure of beta-Amyloid Fibrils in Alzheimer's Disease Brain Tissue. Cell. 154:1257-1268.

[26] Straub, J. E., and D. Thirumalai. 2011. Toward a molecular theory of early and late events in monomer to amyloid fibril formation. Annu. Rev. Phys. Chem. 62:437-463.

[27] Reddy, G., J. E. Straub, and D. Thirumalai. 2009. Dynamics of locking of peptides onto growing amyloid fibrils. Proc. Natl. Acad. Sci. USA. 106:11948-11953.

[28] O'Brien, E. P., Y. Okamoto, J. E. Straub, B. R. Brooks, and D. Thirumalai. 2009. Thermodynamic perspective on the dock-lock growth mechanism of amyloid fibrils. J. Phys. Chem. B. 113:14421-14430.

[29] Baumketner, A., M. G. Krone, and J.-E. Shea. 2008. Role of the familial Dutch mutation E22Q in the folding and aggregation of the 15–28 fragment of the Alzheimer amyloid-β protein. Proc. Natl. Acad. Sci. USA. 105:6027-6032.

[30] Nguyen, P. H., M. S. Li, G. Stock, J. E. Straub, and D. Thirumalai. 2007. Monomer adds to preformed structured oligomers of Aβ-peptides by a two-stage dock–lock mechanism. Proc. Natl. Acad. Sci. USA. 104:111-116.

[31] Gurry, T., and C. M. Stultz. 2014. Mechanism of amyloid-beta fibril elongation. Biochemistry. 53:6981-6991.

[32] Han, W., and K. Schulten. 2014. Fibril Elongation by Aβ17–42: Kinetic Network Analysis of Hybrid-Resolution Molecular Dynamics Simulations. J. Am. Chem. Soc. 136:12450-12460.

[33] Bernstein, S. L., N. F. Dupuis, N. D. Lazo, T. Wyttenbach, M. M. Condron, G. Bitan, D. B. Teplow, J.-E. Shea, B. T. Ruotolo, C. V. Robinson, and M. T. Bowers. 2009.

Amyloid-β protein oligomerization and the importance of tetramers and dodecamers in the aetiology of Alzheimer's disease. Nat. Chem. 1:326-331.

[34] Hong, D. P., S. Han, A. L. Fink, and V. N. Uversky. 2011. Characterization of the non-fibrillar alpha-synuclein oligomers. Protein Pept. Lett. 18:230-240.

[35] Lorenzen, N., S. B. Nielsen, A. K. Buell, J. D. Kaspersen, P. Arosio, B. S. Vad, W. Paslawski, G. Christiansen, Z. Valnickova-Hansen, M. Andreasen, J. J. Enghild, J. S. Pedersen, C. M. Dobson, T. P. Knowles, and D. E. Otzen. 2014. The role of stable alpha-synuclein oligomers in the molecular events underlying amyloid formation. J. Am. Chem. Soc. 136:3859–3868.

[36] Paslawski, W., M. Andreasen, S. B. Nielsen, N. Lorenzen, K. Thomsen, J. D. Kaspersen, J. S. Pedersen, and D. E. Otzen. 2014. High Stability and Cooperative Unfolding of α-Synuclein Oligomers. Biochemistry. 53:6252-6263.

[37] Miller, Y., B. Ma, C.-J. Tsai, and R. Nussinov. 2010. Hollow core of Alzheimer's Aβ42 amyloid observed by cryoEM is relevant at physiological pH. Proc. Natl. Acad. Sci. USA. 107:14128-14133.

[38] Kayed, R., Y. Sokolov, B. Edmonds, T. M. McIntire, S. C. Milton, J. E. Hall, and C. G. Glabe. 2004. Permeabilization of Lipid Bilayers Is a Common Conformation-dependent Activity of Soluble Amyloid Oligomers in Protein Misfolding Diseases. J. Biol. Chem. 279:46363-46366.

[39] Harper, J. D., and P. T. Lansbury, Jr. 1997. Models of amyloid seeding in Alzheimer's disease and scrapie: mechanistic truths and physiological consequences of the time-dependent solubility of amyloid proteins. Annu. Rev. Biochem. 66:385-407.

[40] Serio, T. R., A. G. Cashikar, A. S. Kowal, G. J. Sawicki, J. J. Moslehi, L. Serpell, M. F. Arnsdorf, and S. L. Lindquist. 2000. Nucleated conformational conversion and the replication of conformational information by a prion determinant. Science. 289:1317-1321.

[41] Xue, W.-F., S. W. Homans, and S. E. Radford. 2008. Systematic analysis of nucleation-dependent polymerization reveals new insights into the mechanism of amyloid self-assembly. Proc. Natl. Acad. Sci. USA. 105:8926-8931.

[42] Cohen, S. I., S. Linse, L. M. Luheshi, E. Hellstrand, D. A. White, L. Rajah, D. E. Otzen, M. Vendruscolo, C. M. Dobson, and T. P. Knowles. 2013. Proliferation of amyloid-beta42 aggregates occurs through a secondary nucleation mechanism. Proc. Natl. Acad. Sci. USA. 110:9758-9763.

[43] Nguyen, P., and P. Derreumaux. 2014. Understanding Amyloid Fibril Nucleation and Aβ Oligomer/Drug Interactions from Computer Simulations. Acc. Chem. Res. 47:603-611.

[44] Lee, J., E. K. Culyba, E. T. Powers, and J. W. Kelly. 2011. Amyloid-β forms fibrils by nucleated conformational conversion of oligomers. Nat. Chem. Biol. 7:602-609.

[45] Meisl, G., X. Yang, E. Hellstrand, B. Frohm, J. B. Kirkegaard, S. I. Cohen, C. M. Dobson, S. Linse, and T. P. Knowles. 2014. Differences in nucleation behavior underlie the contrasting aggregation kinetics of the Abeta40 and Abeta42 peptides. Proc. Natl. Acad. Sci. USA. 111:9384-9389.

[46] Buell, A. K., C. Galvagnion, R. Gaspar, E. Sparr, M. Vendruscolo, T. P. J. Knowles, S. Linse, and C. M. Dobson. 2014. Solution conditions determine the relative importance of nucleation and growth processes in α-synuclein aggregation. Proc. Natl. Acad. Sci. USA. 111:7671-7676.

[47] Tomaselli, S., V. Esposito, P. Vangone, N. A. J. van Nuland, A. M. J. J. Bonvin, R. Guerrini, T. Tancredi, P. A. Temussi, and D. Picone. 2006. The α-to-β Conformational Transition of Alzheimer's Aβ-(1–42) Peptide in Aqueous Media is Reversible: A Step by Step Conformational Analysis Suggests the Location of β Conformation Seeding. Chembiochem. 7:257-267.

[48] Jin, M., N. Shepardson, T. Yang, G. Chen, D. Walsh, and D. J. Selkoe. 2011. Soluble amyloid beta-protein dimers isolated from Alzheimer cortex directly induce Tau hyperphosphorylation and neuritic degeneration. Proc. Natl. Acad. Sci. USA. 108:5819-5824.

[49] Shankar, G. M., S. Li, T. H. Mehta, A. Garcia-Munoz, N. E. Shepardson, I. Smith, F. M. Brett, M. A. Farrell, M. J. Rowan, C. A. Lemere, C. M. Regan, D. M. Walsh, B. L.

Sabatini, and D. J. Selkoe. 2008. Amyloid-beta protein dimers isolated directly from Alzheimer's brains impair synaptic plasticity and memory. Nat. Med. 14:837-842.

[50] Glabe, C. G. 2006. Common mechanisms of amyloid oligomer pathogenesis in degenerative disease. Neurobiol. Aging. 27:570-575.

[51] Glabe, C. G. 2008. Structural Classification of Toxic Amyloid Oligomers. J. Biol. Chem. 283:29639-29643.

[52] Ono, K., M. M. Condron, and D. B. Teplow. 2009. Structure–neurotoxicity relationships of amyloid β-protein oligomers. Proc. Natl. Acad. Sci. USA. 106:14745-14750.

[53] Tomic, J. L., A. Pensalfini, E. Head, and C. G. Glabe. 2009. Soluble fibrillar oligomer levels are elevated in Alzheimer's disease brain and correlate with cognitive dysfunction. Neurobiol. Dis. 35:352-358.

[54] Yu, L., R. Edalji, J. E. Harlan, T. F. Holzman, A. P. Lopez, B. Labkovsky, H. Hillen, S. Barghorn, U. Ebert, P. L. Richardson, L. Miesbauer, L. Solomon, D. Bartley, K. Walter, R. W. Johnson, P. J. Hajduk, and E. T. Olejniczak. 2009. Structural Characterization of a Soluble Amyloid β-Peptide Oligomer. Biochemistry. 48:1870-1877.

[55] Laganowsky, A., C. Liu, M. R. Sawaya, J. P. Whitelegge, J. Park, M. Zhao, A. Pensalfini, A. B. Soriaga, M. Landau, P. K. Teng, D. Cascio, C. Glabe, and D. Eisenberg. 2012. Atomic view of a toxic amyloid small oligomer. Science. 335:1228-1231.

[56] Roberts, R. F., R. Wade-Martins, and J. Alegre-Abarrategui. 2015. Direct visualization of alpha-synuclein oligomers reveals previously undetected pathology in Parkinson's disease brain. Brain. 138:1642-1657.

[57] Ahmed, M., J. Davis, D. Aucoin, T. Sato, S. Ahuja, S. Aimoto, J. I. Elliott, W. E. Van Nostrand, and S. O. Smith. 2010. Structural conversion of neurotoxic amyloid-beta(1-42) oligomers to fibrils. Nat. Struct. Mol. Biol. 17:561-567.

[58] Sandberg, A., L. M. Luheshi, S. Sollvander, T. Pereira de Barros, B. Macao, T. P. Knowles, H. Biverstal, C. Lendel, F. Ekholm-Petterson, A. Dubnovitsky, L. Lannfelt, C. M. Dobson, and T. Hard. 2010. Stabilization of neurotoxic Alzheimer amyloid-beta oligomers by protein engineering. Proceedings of the National Academy of Sciences of the United States of America. 107:15595-15600.

[59] Huang, D., M. I. Zimmerman, P. K. Martin, A. J. Nix, T. L. Rosenberry, and A. K. Paravastu. 2015. Antiparallel beta-sheet structure within the C-terminal region of 42-residue Alzheimer's beta-amyloid peptides when they form 150 kDa oligomers. J. Mol. Biol. 427:2319-2328.

[60] Stroud, J. C., C. Liu, P. K. Teng, and D. Eisenberg. 2012. Toxic fibrillar oligomers of amyloid-beta have cross-beta structure. Proc. Natl. Acad. Sci. USA. 109:7717-7722.

[61] Cerf, E., R. Sarroukh, S. Tamamizu-Kato, L. Breydo, S. Derclaye, Y. F. Dufrene, V. Narayanaswami, E. Goormaghtigh, J. M. Ruysschaert, and V. Raussens. 2009. Antiparallel beta-sheet: a signature structure of the oligomeric amyloid beta-peptide. The Biochemical journal. 421:415-423.

[62] Liu, C., M. Zhao, L. Jiang, P.-N. Cheng, J. Park, M. R. Sawaya, A. Pensalfini, D. Gou, A. J. Berk, C. G. Glabe, J. Nowick, and D. Eisenberg. 2012. Out-of-register β-sheets suggest a pathway to toxic amyloid aggregates. Proc. Natl. Acad. Sci. USA. 109:20913-20918.

[63] Bodner, C. R., A. S. Maltsev, C. M. Dobson, and A. Bax. 2009. Differential Phospholipid Binding of α-Synuclein Variants Implicated in Parkinson's Disease Revealed by Solution NMR Spectroscopy. Biochemistry. 49:862-871.

[64] Lorenzen, N., L. Lemminger, J. N. Pedersen, S. B. Nielsen, and D. E. Otzen. 2014. The N-terminus of alpha-synuclein is essential for both monomeric and oligomeric interactions with membranes. FEBS Lett. 588:497-502.

[65] Tsigelny, I. F., P. Bar-On, Y. Sharikov, L. Crews, M. Hashimoto, M. A. Miller, S. H. Keller, O. Platoshyn, J. X. J. Yuan, and E. Masliah. 2007. Dynamics of α-synuclein

aggregation and inhibition of pore-like oligomer development by β-synuclein. FEBS J. 274:1862-1877.

[66] Palecek, E., V. Ostatna, M. Masarik, C. W. Bertoncini, and T. M. Jovin. 2008. Changes in interfacial properties of alpha-synuclein preceding its aggregation. Analyst. 133:76-84.

[67] Yatin, S., M. Aksenova, M. Aksenov, W. Markesbery, T. Aulick, and D. A. Butterfield. 1998. Temporal relations among amyloid β-peptide-induced free-radical oxidative stress, neuronal toxicity, and neuronal defensive responses. J. Mol. Neurosci. 11:183-197.

[68] Mucke, L., and D. J. Selkoe. 2012. Neurotoxicity of Amyloid β-Protein: Synaptic and Network Dysfunction. CSH Perspect. Med. 2:a006338.

[69] Snyder, E. M., Y. Nong, C. G. Almeida, S. Paul, T. Moran, E. Y. Choi, A. C. Nairn, M. W. Salter, P. J. Lombroso, G. K. Gouras, and P. Greengard. 2005. Regulation of NMDA receptor trafficking by amyloid β. Nat. Neurosci. 8:1051-1058.

[70] Sakono, M., and T. Zako. 2010. Amyloid oligomers: formation and toxicity of Abeta oligomers. FEBS J. 277:1348-1358.

[71] LaFerla, F. M., K. N. Green, and S. Oddo. 2007. Intracellular amyloid-[beta] in Alzheimer's disease. Nat. Rev. Neurosci. 8:499-509.

[72] Tseng, B. P., K. N. Green, J. L. Chan, M. Blurton-Jones, and F. M. LaFerla. 2008. Aβ inhibits the proteasome and enhances amyloid and tau accumulation. Neurobiol. Aging. 29:1607-1618.

[73] Kang, J., H. G. Lemaire, A. Unterbeck, J. M. Salbaum, C. L. Masters, K. H. Grzeschik, G. Multhaup, K. Beyreuther, and B. Muller-Hill. 1987. The precursor of Alzheimer's disease amyloid A4 protein resembles a cell-surface receptor. Nature. 325:733-736.

[74] Masters, C. L., G. Simms, N. A. Weinman, G. Multhaup, B. L. McDonald, and K. Beyreuther. 1985. Amyloid plaque core protein in Alzheimer disease and Down syndrome. Proc. Natl. Acad. Sci. USA. 82:4245-4249.

[75] Hardy, J., and D. J. Selkoe. 2002. The amyloid hypothesis of Alzheimer's disease: progress and problems on the road to therapeutics. Science. 297:353-356.

[76] Tjernberg, L. O., J. Näslund, F. Lindqvist, J. Johansson, A. R. Karlström, J. Thyberg, L. Terenius, and C. Nordstedt. 1996. Arrest of -Amyloid Fibril Formation by a Pentapeptide Ligand. J. Biol. Chem. 271:8545-8548.

[77] Chabry, J., B. Caughey, and B. Chesebro. 1998. Specific Inhibition of in Vitro Formation of Protease-resistant Prion Protein by Synthetic Peptides. J. Biol. Chem. 273:13203-13207.

[78] Dev, K. K., K. Hofele, S. Barbieri, V. L. Buchman, and H. van der Putten. 2003. Part II: α-synuclein and its molecular pathophysiological role in neurodegenerative disease. Neuropharmacology. 45:14-44.

[79] Cohen, S. I. A., P. Arosio, J. Presto, F. R. Kurudenkandy, H. Biverstål, L. Dolfe, C. Dunning, X. Yang, B. Frohm, M. Vendruscolo, J. Johansson, C. M. Dobson, A. Fisahn, T. P. J. Knowles, and S. Linse. 2015. A molecular chaperone breaks the catalytic cycle that generates toxic Aβ oligomers. Nat. Struct. Mol. Biol. 22:207-213.

[80] Crescenzi, O., S. Tomaselli, R. Guerrini, S. Salvadori, A. M. D'Ursi, P. A. Temussi, and D. Picone. 2002. Solution structure of the Alzheimer amyloid β-peptide (1–42) in an apolar microenvironment. Eur. J. Biochem. 269:5642-5648.

[81] Sgourakis, N. G., M. Merced-Serrano, C. Boutsidis, P. Drineas, Z. Du, C. Wang, and A. E. Garcia. 2011. Atomic-level characterization of the ensemble of the Abeta(1-42) monomer in water using unbiased molecular dynamics simulations and spectral algorithms. J. Mol. Biol. 405:570-583.

[82] Vivekanandan, S., J. R. Brender, S. Y. Lee, and A. Ramamoorthy. 2011. A partially folded structure of amyloid-beta(1–40) in an aqueous environment. Biochem. Biophys. Res. Commun. 411:312-316.

[83] Binnig, G., H. Rohrer, C. Gerber, and E. Weibel. 1982. Surface Studies by Scanning Tunneling Microscopy. Phys. Rev. Lett. 49:57-61.

[84] Ando, T., T. Uchihashi, and N. Kodera. 2013. High-Speed AFM and Applications to Biomolecular Systems. Annu. Rev. Biophys. 42:393-414.

[85] Kodera, N., D. Yamamoto, R. Ishikawa, and T. Ando. 2010. Video imaging of walking myosin V by high-speed atomic force microscopy. Nature. 468:72-76.

[86] Uchihashi, T., R. Iino, T. Ando, and H. Noji. 2011. High-speed atomic force microscopy reveals rotary catalysis of rotorless F(1)-ATPase. Science. 333:755-758.

[87] Miyagi, A., T. Ando, and Y. L. Lyubchenko. 2011. Dynamics of nucleosomes assessed with time-lapse high-speed atomic force microscopy. Biochemistry. 50:7901-7908.

[88] Miyagi, A., Y. Tsunaka, T. Uchihashi, K. Mayanagi, S. Hirose, K. Morikawa, and T. Ando. 2008. Visualization of intrinsically disordered regions of proteins by high-speed atomic force microscopy. Chemphyschem : a European journal of chemical physics and physical chemistry. 9:1859-1866.

[89] Ishino, S., T. Yamagami, M. Kitamura, N. Kodera, T. Mori, S. Sugiyama, T. Ando, N. Goda, T. Tenno, H. Hiroaki, and Y. Ishino. 2014. Multiple Interactions of the Intrinsically Disordered Region between the Helicase and Nuclease Domains of the Archaeal Hef Protein. J. Biol. Chem. 289:21627-21639.

[90] Lamour, G., C. K. Yip, H. Li, and J. Gsponer. 2014. High Intrinsic Mechanical Flexibility of Mouse Prion Nanofibrils Revealed by Measurements of Axial and Radial Young's Moduli. ACS Nano. 8:3851–3861.

[91] Ruggeri, F. S., J. Adamcik, J. S. Jeong, H. A. Lashuel, R. Mezzenga, and G. Dietler. 2015. Influence of the beta-sheet content on the mechanical properties of aggregates during amyloid fibrillization. Angew. Chem. 54:2462-2466.

[92] Smith, J. F., T. P. J. Knowles, C. M. Dobson, C. E. MacPhee, and M. E. Welland. 2006. Characterization of the nanoscale properties of individual amyloid fibrils. Proc. Natl. Acad. Sci. USA. 103:15806-15811.

[93] Lyubchenko, Y. L., B. H. Kim, A. V. Krasnoslobodtsev, and J. Yu. 2010. Nanoimaging for protein misfolding diseases. Wiley Interdiscip. Rev. Nanomed. Nanobiotechnol. 2:526-543.

[94] Krasnoslobodtsev, A. V., J. Peng, J. M. Asiago, J. Hindupur, J. C. Rochet, and Y. L. Lyubchenko. 2012. Effect of spermidine on misfolding and interactions of alpha-synuclein. PloS one. 7:e38099.

[95] Portillo, A. M., A. V. Krasnoslobodtsev, and Y. L. Lyubchenko. 2012. Effect of electrostatics on aggregation of prion protein Sup35 peptide. J. Phys. Condens. Matter. 24:164205.

[96] Kim, B. H., and Y. L. Lyubchenko. 2014. Nanoprobing of misfolding and interactions of amyloid beta 42 protein. Nanomedicine : nanotechnology, biology, and medicine. 10:871-878.

[97] Lv, Z., R. Roychaudhuri, M. M. Condron, D. B. Teplow, and Y. L. Lyubchenko. 2013. Mechanism of amyloid beta protein dimerization determined using single-molecule AFM force spectroscopy. Sci. Rep. 3.

[98] Yu, J., S. Malkova, and Y. L. Lyubchenko. 2008. α-Synuclein Misfolding: Single Molecule AFM Force Spectroscopy Study. J. Mol. Biol. 384:992-1001.

[99] Yu, J., and Y. L. Lyubchenko. 2009. Early Stages for Parkinson's Development: α-Synuclein Misfolding and Aggregation. J. Neuroimmune Pharm. 4:10-16.

[100] Kim, B. H., N. Y. Palermo, S. Lovas, T. Zaikova, J. F. Keana, and Y. L. Lyubchenko. 2011. Single-molecule atomic force microscopy force spectroscopy study of Abeta-40 interactions. Biochemistry. 50:5154-5162.

[101] Kim, B.-H., and Y. L. Lyubchenko. 2014. Nanoprobing of misfolding and interactions of amyloid β 42 protein. Nanomedicine : nanotechnology, biology, and medicine. 10:871-878.

[102] Lovas, S., Y. Zhang, J. Yu, and Y. L. Lyubchenko. 2013. Molecular Mechanism of Misfolding and Aggregation of Aβ(13–23). J. Phys. Chem. B. 117:6175-6186.

[103] Tong, Z., A. Mikheikin, A. Krasnoslobodtsev, Z. Lv, and Y. L. Lyubchenko. 2013. Novel polymer linkers for single molecule AFM force spectroscopy. Methods. 60:161-168.

[104] Krasnoslobodtsev, A. V., I. L. Volkov, J. M. Asiago, J. Hindupur, J.-C. Rochet, and Y. L. Lyubchenko. 2013. α-Synuclein Misfolding Assessed with Single Molecule AFM Force Spectroscopy: Effect of Pathogenic Mutations. Biochemistry. 52:7377-7386.

[105] Krasnoslobodtsev, A. V., J. Peng, J. M. Asiago, J. Hindupur, J.-C. Rochet, and Y. L. Lyubchenko. 2012. Effect of Spermidine on Misfolding and Interactions of α-Synuclein. PLoS One. 7:e38099.

[106] Urbanc, B., L. Cruz, F. Ding, D. Sammond, S. Khare, S. V. Buldyrev, H. E. Stanley, and N. V. Dokholyan. 2004. Molecular dynamics simulation of amyloid beta dimer formation. Biophys. J. 87:2310-2321.

[107] Mitternacht, S., I. Staneva, T. Hard, and A. Irback. 2011. Monte Carlo study of the formation and conformational properties of dimers of Abeta42 variants. J. Mol. Biol. 410:357-367.

[108] Barz, B., and B. Urbanc. 2012. Dimer Formation Enhances Structural Differences between Amyloid β-Protein (1–40) and (1–42): An Explicit-Solvent Molecular Dynamics Study. PLoS One. 7:e34345.

[109] Zhang, T., J. Zhang, P. Derreumaux, and Y. Mu. 2013. Molecular Mechanism of the Inhibition of EGCG on the Alzheimer Aβ1–42 Dimer. J. Phys. Chem. B. 117:3993-4002.

[110] Viet, M. H., P. H. Nguyen, P. Derreumaux, and M. S. Li. 2014. Effect of the English Familial Disease Mutation (H6R) on the Monomers and Dimers of Aβ40 and Aβ42. ACS Chem. Neurosci. 5:646-657.

[111] Zhu, X., R. P. Bora, A. Barman, R. Singh, and R. Prabhakar. 2012. Dimerization of the Full-Length Alzheimer Amyloid β-Peptide (Aβ42) in Explicit Aqueous Solution: A Molecular Dynamics Study. J. Phys. Chem. B. 116:4405-4416.

[112] Brockwell, D. J., E. Paci, R. C. Zinober, G. S. Beddard, P. D. Olmsted, D. A. Smith, R. N. Perham, and S. E. Radford. 2003. Pulling geometry defines the mechanical resistance of a β-sheet protein. Nat. Struct. Mol. Biol. 10:731-737.

[113] Guzmán, D. L., A. Randall, P. Baldi, and Z. Guan. 2010. Computational and single-molecule force studies of a macro domain protein reveal a key molecular determinant for mechanical stability. Proc. Natl. Acad. Sci. USA. 107:1989– 1994.

[114] Lovas, S., Y. Zhang, J. Yu, and Y. L. Lyubchenko. 2013. Molecular mechanism of misfolding and aggregation of abeta(13-23). The journal of physical chemistry. B. 117:6175-6186.

[115] Lu, H., B. Isralewitz, A. Krammer, V. Vogel, and K. Schulten. 1998. Unfolding of titin immunoglobulin domains by steered molecular dynamics simulation. Biophys. J. 75:662-671.

[116] Grubmüller, H., B. Heymann, and P. Tavan. 1996. Ligand Binding: Molecular Mechanics Calculation of the Streptavidin-Biotin Rupture Force. Science. 271:997-999.

[117] Lemkul, J. A., and D. R. Bevan. 2010. Assessing the Stability of Alzheimer's Amyloid Protofibrils Using Molecular Dynamics. J. Phys. Chem. B. 114:1652-1660.

[118] Lee, E. H., J. Hsin, M. Sotomayor, G. Comellas, and K. Schulten. 2009. Discovery Through the Computational Microscope. Structure. 17:1295-1306.

[119] Rico, F., L. Gonzalez, I. Casuso, M. Puig-Vidal, and S. Scheuring. 2013. High-Speed Force Spectroscopy Unfolds Titin at the Velocity of Molecular Dynamics Simulations. Science. 342:741-743.

[120] Jonsson, S. A. E., S. Mitternacht, and A. Irback. 2013. Mechanical resistance in unstructured proteins. Biophys. J. 104:2725-2732.

[121] Zhang, Y., and Yuri L. Lyubchenko. 2014. The Structure of Misfolded Amyloidogenic Dimers: Computational Analysis of Force Spectroscopy Data. Biophys. J. 107:2903-2910.

Chapter 2

MOLECULAR MECHANISM OF SELF-ASSEMBLY OF Aβ(13-23)

2.1. INTRODUCTION

As described in chapter 1, the self-assembly of an Amyloid protein from disordered monomer to amyloid fibril is associated with several neurodegenerative diseases. We have developed the AFM-based force spectroscopy method to measure amyloid protein monomer interactions, which is the initial step of such self-assembly. Based on our force spectroscopy data, we propose that the formation of dimers is the key step in the initiation of aggregation with the dimers acting as building blocks for the protein aggregation process. To date, the mechanism underlying the formation of dimers and their structure in misfolded transient states remains unclear.

To address these questions, we combined AFM force spectroscopy and MD simulations to characterize the misfolding and aggregation process for the Aβ peptide. We selected the 13-23 segment (HHQKLVFFAED) of Aβ since it contains the region Aβ (16−20), which is known to be crucial for Aβ fibril formation and because it mediates the strongest Aβ-Aβ binding [1, 2]. The N-terminal His13 was replaced with Cys for use as an anchor in the site specific immobilization of the peptide; this derivative will be hereby referred to as Aβ(13-23). From AFM experiments it is evident that the peptide spontaneously forms amyloid fibrils. DFS analysis shows that the peptide dimers are stable with a lifetime of ∼1 s. The MD simulations revealed that the peptide contains a β-

turn/bend segment that refolds to a β-sheet conformation when two monomers approach and form a stable dimer structure in an antiparallel orientation. SMD simulation was applied to analyze the rupture process for the dimer. The results demonstrate that the individual peptide chains under the applied force undergo structural transition, which is accompanied by the sharp rupture of the dimer. A molecular mechanism is proposed for the protein misfolding and aggregation.

2.2. METHODS

2.2.1. Sample Preparation for AFM Force Spectroscopy

Peptide immobilization on tips and mica sheets was done as described in refs [3, 4]. Briefly, silicon nitride (Si_3N_4) AFM tips (Bruker, MODEL: MSNL) were cleaned in 98% ethanol (EtOH) and then irradiated by UV for 30 min. The AFM tips were next immersed into 167 μM Maleimide Silatrane (MAS) aqueous solution for 30 min followed by thorough rinsing with deionized water. For covalent attachment of the peptide to MAS functionalized tips, 19 nM peptide in pH 7.0 4-(2-hydroxyethyl)-1-piperazineethanesulfonic acid (HEPES, Sigma-Aldrich Inc.) buffer was reacted with 0.25 mM Tris(2-carboxyethyl)phosphine (TCEP; Hampton Research Inc.) hydrochloride for 10 min, and the MAS functionalized tips were immersed into this solution for 1 h. Following the immersion, tips were rinsed with a pH 7.0 buffer (100 mM HEPES-sodium hydroxide) and unreacted maleimide was blocked by treatment with 10 mM β-mercaptoethanol for 10 min at room temperature. The functionalized probes were washed with pH 7.0 HEPES buffer and stored in the same buffer until use; typically, the storage

time was less than 24 h. Mica sheets (Asheville-Schoonmaker Mica Co., Newport News, VA) were cut into ~1.5 cm × 1.5 cm plates and the freshly cleaved mica surfaces were treated with 167 μM Aminopropyl Silatrane (APS) for 30 min followed by a reaction with 167 μM maleimidepolyethylene glycol-succinimidyl valerate (MAL-PEG-SVA; 3.4 kDa Laysan Bio Inc, Arab, AL) in dimethyl sulfoxide (DMSO; Sigma-Aldrich Inc.) for 3 h. The mica plates were then rinsed repetitively with DMSO and then Deionized water (18.2 MΩ, 0.22 μm pore size filter, APS Water Services Corp., Van Nuys, CA) to remove un-bound MAL-PEG-SVA, samples were dried with a gentile stream of argon gas. The peptide preparation and subsequent steps were the same as just described for the AFM tips. Prepared mica plates were stored in pH 7.0 HEPES buffer until use; the storage time was typically less than 24 h.

2.2.2. AFM Imaging

The Aβ(13-23) stock solution (3.74 mM) in DMSO was diluted to a concentration 100 μM in pH 5 buffer (a mixture of 1 mM Na_2HPO_4 and 0.94 mM citric acid) and incubated at 37 °C for one day. The 10 μL aliquots were placed on freshly cleaved mica and the sample was allowed to adhere to the surface for 5 min. The unbound sample was rinsed with 100 μL of double-distilled water three times, dried with a gentile stream of argon gas, and stored in a vacuum oven at 25 °C overnight (~12 h) for complete dehydration. The images were acquired with a Multimode AFM equipped with a Nanoscope IIId controller (Veeco Inc., Santa Barbara, CA, USA) operating in tapping mode at ambient conditions. A silicon tip with a spring constant at 40 N/m was used (Veeco Inc., Santa Barbara, CA, USA).

2.2.3. Molecular Dynamics (MD) Simulations.

2.2.3.1. Simulations of Monomer Structures.

The MD simulations were performed using the GROMACS 4.5.4 package [5] by modifications of previous methods [6, 7] and using the OPLS-AA/L force field [8]. Three initial structures of Ac-[Cys13]Aβ(13-23)-NH_2 for the simulations were derived using experimental Aβ structures from the protein data bank (PDB) [9]. The structure with PDB ID 1HZ3 [10] was used for simulation I (simI); that with PDB ID 1Z0Q [11] was used for simulation II (simII); and the solid state NMR structure of Aβ(1-40) by Petkova and associates [12] was used for simulation III (simIII). The *N-acetyl* and amide capping groups were added to the N and C-terminus, respectively, in order to preserve the electronic structure of the backbone as in the full length Aβ. Peptides were solvated with 1200, 1520, and 5070 TIP4P water molecules [13] for simI, simII, and simIII, respectively, in a truncated octahedron so that the minimal distance of the peptide from edge of the octahedron was a minimum of 1 nm. Charged side chains of peptides were neutralized by replacing water molecules with Na^+ for Asp and Glu and Cl^- for Lys residues at the positions of the first atoms with the most favorable electrostatic potential. Systems were subjected to 1000 steps steepest descent energy minimization and then to 100 ps NVT, constant number of molecules, volume, and temperature (300 K) simulation so that the position of the peptide was constrained at the center of the octahedron with a force constant of 1000 kJ mol^{-1}. The three different initial starting structures were subsequently subjected to 200.2 ns NPT constant pressure (1 bar) and constant temperature (300 K) simulation. The following parameters were used for the

simulations: integration step was 2 fs, and snapshots of trajectories were saved at every 20 ps; the non-bonded interactions list was updated following every 10 steps; the LINCS algorithm [14] was used to constrain all bonds to their correct length, with a warning angle of 30°; the peptide and solvent with ions were coupled to separate temperature baths with a relaxation constant of 0.1 ps; and the peptide and solvent with ions were coupled separately to constant pressure using Berendsen scaling [15] with a relaxation constant of 1.0 ps and 4.5×10^{-5} bar^{-1} isothermal compressibility. Coulomb interactions were calculated using a twin-range cutoff with reaction-field correction methods. The dielectric constant of the system was set to 78.0 beyond 1.4 nm. The short-range cutoff was 0.9 nm. For the calculations of van der Waals interactions, the short-range and long-range cutoffs were 0.9 and 1.4 nm, respectively, and dispersion correction was applied.

2.2.3.2. Analysis of Trajectories

The first 0.2 ns of the trajectory was considered as an equilibration period and was omitted from the analysis. The secondary structures explored during the simulations by Ac-[Cys13]Aβ(13-23)-NH_2 were analyzed using the defined secondary structure of proteins (DSSP) method [16]. The ϕ and ψ torsional angles for each residue were determined using the g_rama utility of GROMACS. The R 2.14.0 program [17] and in-house written R-script (Appendix 2.1) were used for data processing and drawing the Ramachandran plot following the methodology of Lovell and associates [18]. The number of intramolecular hydrogen bonds was determined by using the g_hbond utility of GROMACS. The root-mean-square deviation (RMSD) of backbone atoms and the radius of gyration (Rg) of the peptide chain was determined by the g_rms and g_gyrate

utilities of GROMACS, respectively. Trajectories were submitted to cluster analysis by the GROMOS method of clustering [19] using a backbone RMSD cutoff of 0.1 nm. To determine if the peptide explores similar conformational space during simI, simII, and simIII, trajectories were compared by using essential dynamics analysis and calculating pairwise root-mean-square inner product (RMSIP) of eigenvector of trajectories [20]. Covariance matrix was calculated using the g_covar command of GROMACS, the eigenvectors corresponding to the 10 highest eigenvalues were used to calculate the RMSIP. The RMSIP was calculated using equation for entire systems and individual monomers:

$$RMSIP = \left(\frac{1}{10} \sum_{10}^{i=1} \sum_{10}^{j=1} (\eta \cdot \nu)^2 \right)^{1/2}$$

where η_i and ν_j are the eigenvectors of two independent simulations. The R script example of the RMSIP calculation is placed in appendix 2.2.

2.2.3.3. Simulation of the Dimer Structure.

The dimer structure of the peptide in parallel arrangement was made from the central structure of the largest cluster of simIII so that the x, y, and z distances between the two chains were 1.5, 0.5, and 0.1 nm, respectively. The individual chains were assigned as chains A and B. The dimer was solvated in a truncated octahedron with 3239 TIP4P water molecules so that the minimal distance of the peptide from the edge of the octahedron was a minimum of 1 nm. Four Na^+ and two Cl^- ions were added to the systems to neutralize charges by replacing water molecules with Na^+ for Asp and Glu and Cl^- for Lys residues at the positions of the first atoms with the most favorable

electrostatic potential. The system was subjected to 1000 steps steepest descent energy minimization and then to 100 ps NVT simulation at 300 K so that the position of the dimer was constrained at the center of the octahedron with a force constant of 1000 kJ mol^{-1}. The system was then submitted to a 400.2 ns NPT simulation at 1 bar pressure and a temperature of 300 K. The rest of the parameters were the same as those used in monomer simulations.

To test whether applying different force fields would affect the stability of the dimer, the starting structure for the SMD simulation was submitted to 400 ns and 1.1 μs MD simulations using the OPLS-AA/L [8] and the Amber ff99sb*-ILDN [21] force fields, respectively. For the simulation using the Amber ff99sb*-ILDN force field, the dimer structure was solvated in a truncated octahedron with 3092 TIP3P water molecules so that the minimal distance of the peptide from the edge of the octahedron was 1 nm. The long-range electrostatic interaction was calculated using the PME method with a cutoff distance of 0.9 nm and Fourier spacing 0.15 nm. The rest of the simulation parameters were the same as for the dimer simulation. For the simulation using the OPLS-AA/L force field, the parameters were the same as those used for the dimer simulation.

2.2.3.4. Analysis of the Trajectory of Dimer Simulation.

The DSSP analysis, inter-chain hydrogen bond determinations, and the radius of gyration calculation were performed as described for the monomer simulations above. Inter-chain salt bridges were determined using a trajectory analysis tool of the VMD package [22]. To determine the parallel or antiparallel orientation of the chains, the

distance between the center of mass of Cys13 of chain A (COM13A) and center of mass of Cys13 of chain B (COM13B) was calculated using the g_dist command of GROMACS. The first 200 ns trajectory and the last 50 ns of trajectory were submitted to cluster analysis using the GROMOS method of clustering [19] and a backbone RMSD cutoff of 0.1 nm. The angle and distance between the plains of the aromatic side chains of Phe were calculated to determine whether aromatic-aromatic (Ar-Ar) interactions exist between two residues. The plane of the Phe side chain ring was defined by CD1, CD2, and CZ atoms. The distance between two rings was the distance between the centers of mass of the aromatic side chain rings of Phe residues. Ar-Ar interactions were assumed when the distance was less than 0.7 nm and the angle between them was greater than or equal to 33° and less than or equal to 150° [23]. The aromatic−backbone (Ar-bb) interactions were determined by calculating the angle and distance between the plane of the aromatic ring of Phe and either the Cα-Hα vector or N-Hα vector of any other residue [24]. The aromatic-CH (Ar-CH) interactions were determined by calculating the angle and distance between the plane of the aromatic ring of Phe and the Cβ-Hβ vector.

When the Amber ff99sb*-ILDN force field was used, the trajectories were analyzed using the DSSP method [16] and the GROMOS method of clustering [19]. For clustering without N- and C-terminal residues, a backbone RMSD cutoff of 0.3 nm was used. The distance between the center of mass of Cys13 of chain A (COM13A) and a center of mass of Cys13 of chain B (COM13B) was calculated.

2.2.3.5. Steered Molecular Dynamics (SMD) Simulations.

The central structure of the largest cluster from the first 200 ns and the last 50 ns of the dimer simulation were used for steered molecular dynamics (SMD) simulations. Dimer structure was solvated in a cubic box of 6.555 nm × 4.376 nm × 18 nm with 16766 TIP4-P water molecules. Four Na^+ ions and two Cl^- ions were added to the systems to neutralize charges by replacing water molecules with Na^+ for Asp and Glu, and Cl^- for Lys residues at the positions of the first atoms with the most favorable electrostatic potential. NPT MD (100 ps) simulation was performed at 300 K with the Berendsen method for temperature and pressure coupling, and the position of the dimer was constrained at the center of the box with a force constant of 1000 kJ mol^{-1}. During SMD simulations, the position of COM13B of the dimer was fixed, and the COM13A was attached to a harmonic spring with a spring constant of 1000 kJ mol^{-1} nm^{-2} and pulled along the z-axis at a rate of 5 nm/ns with a simulation time of 1.4 ns. The final distance between COM13A and COM13B was 7.865 nm. The peptide and solvent with ions were separately coupled to a 1 bar Parrinello-Rahman barostat [25, 26] and a 300 K Nose-Hoover thermostat [27, 28]. The long-range electrostatic interaction was calculated using the PME method with a cutoff distance of 0.9 nm and Fourier spacing of 0.12 nm. The rest of the parameters were the same as those described above.

2.2.3.6. Umbrella Sampling Simulations.

Umbrella sampling simulations [29-31] were used to determine the free energy of binding ($\Delta G_{bindA,B}$) of chain A to B. From the trajectory of the 5 nm/ns SMD simulation, along the z-axis, 31 snapshots were taken as starting configurations for umbrella sampling simulations. In these snapshots, the distance between COM13A and COM13B (ξ reaction coordinate) was increased by 0.25 nm stepwise. Each of the umbrella

windows was simulated for 20 ns. A 1000 kJ mol^{-1} nm^{-2} umbrella potential was imposed in each window. The peptide and solvent with ions were separately coupled to a 1 bar Parrinello-Rahman barostat and a 300 K Nose-Hoover thermostat. The long-range electrostatic interaction was calculated using the PME method with a 0.9 nm cutoff distance and 0.12 nm Fourier spacing. The rest of the parameters were the same as those previously described. The weighted histogram analysis method (WHAM) [32-34] was used to determine the one-dimensional potential of mean force (PMF) curve. The value of ΔG_{bind} was taken as the difference between the highest and lowest values of the PMF curve.

2.2.3.7. Software

Structure manipulations, data analyses, and visualization were done using the analysis suite of the GROMACS [5], the VMD [22] and YASARA (www. yasara.org) packages.

2.3. RESULTS

2.3.1. Misfolding and aggregation of Aβ(13-23): Single molecule AFM studies

To test the ability of Aβ(13-23) to form amyloid fibrils, a solution of the peptide (100 μM) was prepared for self-aggregation at 37 °C. Aliquots of the solution were analyzed with AFM. Figure 2.1 shows a typical image for a sample incubated for 24 h. The sample prepared under these conditions contains primarily fibrils of different lengths

but rather uniform heights. Thus, Aβ(13-23) is capable of spontaneous self-assembly into amyloid fibrils.

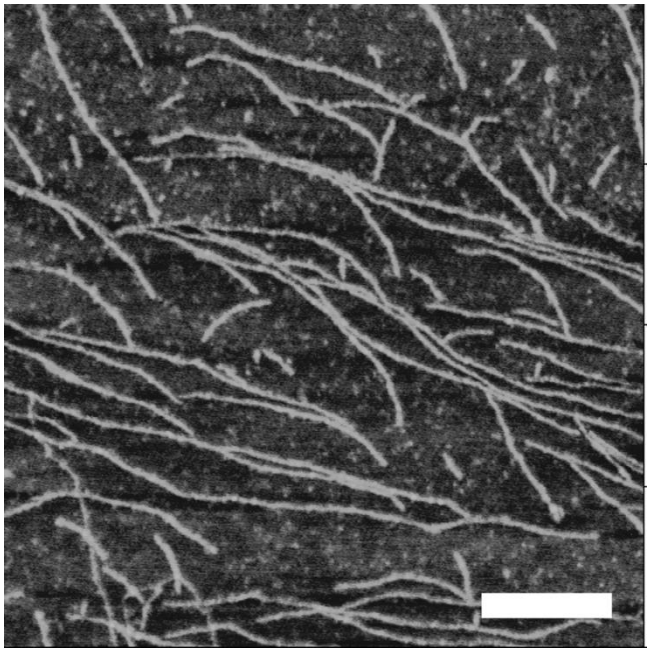

Figure 2.1. Characterization of Aβ(13-23) fibrils by AFM. Aβ(13-23) (100 μM) was incubated for 24 h at 37 °C, and the fibrils were imaged by AFM. The mean height of the fibril was 0.65 ± 0.05 nm. The white scale bar is 200 nm.

To characterize the interactions present during the initial stage of the self-assembly process, we applied an AFM force spectroscopy approach in which the peptide molecules are immobilized on both the AFM tip and on the mica surface (Figure 2.2A). The immobilization was at the N-terminal Cys residues via long flexible polymeric tethers which helped to facilitate proper orientation of the peptides at the approach stage. The flexible tether with a Gauss-distributed random coil conformation allows the tethered peptides to find the optimal orientation. The ends of the tether move independently from each other, thus eliminating potential restriction of the mobility of the peptide attached at one end of the tether relative to the other, attached to the surface. The ability of the peptide to form a dimer was characterized by measuring the strength of the interpeptide interaction in multiple approach−retraction cycles (see review in ref [35] and references therein). A typical force curve illustrating the rupture event, indicated with an arrow, is shown in Figure 2.2B. The extension of the tether is approximated by the worm-like chain model [35] shown in the figure as a black line. The ΔF value in this figure corresponds to the force required for rupture of the peptide dimer to occur. The probing was performed over various positions on the AFM substrate, and the results of such multiple measurements are assembled as a histogram as shown in Figure 2.2B. The distribution has a single peak suggesting a single molecule detection of interpeptide interactions, and thus, the strength of the interactions in dimers formed by the peptides at the approach step is measured.

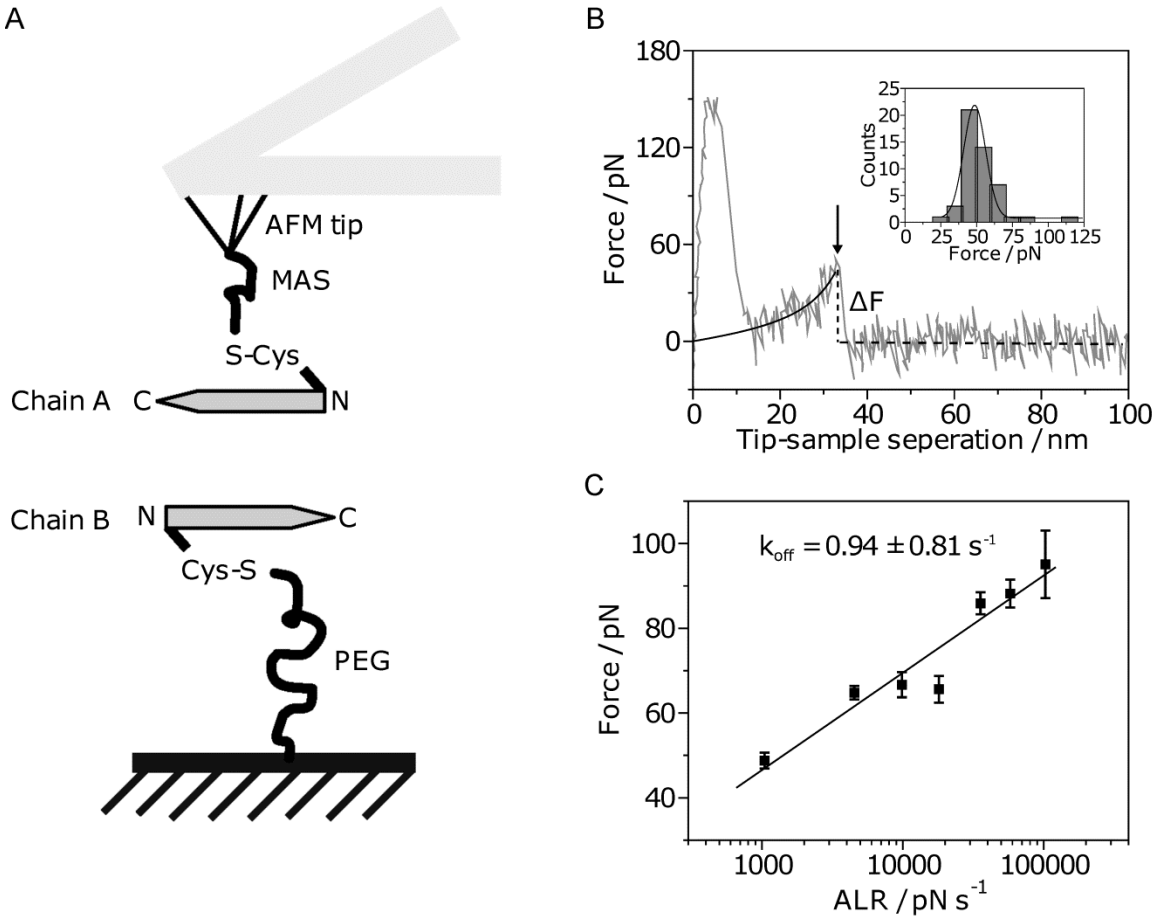

Figure 2.2. Single molecular force spectroscopy. (A) Schematics of the experimental setup. The peptide was immobilized on AFM tips and mica surfaces through N-terminal cysteine. Bifunctional PEG (about 77 PEG repeats long linker) was used to attach the peptides to the mica surface. MAS (5 repeats of PEG, short linker) was utilized to connect peptides to AFM tips. (B) Typical force curve illustrating the rupture event force curves (gray line) recorded at pH 6 with 500 nm/s pulling rate; the black line is from the worm-like chain model fitting [35]. The insert shows the distribution of rupture force (bar) and fitting results with probability function (line). The mean value of force was 48.62 ± 8.38 pN. (C) DFS analysis for Aβ(13-23) acquired at pH 2. Forces obtained from different pulling rates are plotted against logarithmic apparent loading rates (ALR). Seven ALR values were used to generate the plot. Each data point is an average of three independent experiments. The data set was approximated by the Bell-Evans model as described in ref [36]. The intercept on the x-axis was used for the calculation of the off-rate constant producing the lifetime value of 1.06 ± 0.95 s. The large variance of this value is due to a logarithmic dependence of the off-rate constant value on the experimentally determined intercept value.

To characterize the stability of Aβ(13-23) dimers, the dynamic force spectroscopy (DFS) method was applied. In this approach, the probing is performed at different apparent loading rates (10^3 pN s^{-1} − 10^5 pN s^{-1}), and after the extrapolation of the data to the zero pulling rate, the off-rate constant is determined (see ref [35] and references therein). The results of the DFS analysis for Aβ(13-23) are shown in Figure 2.2C. The experimental data fitted to a straight line and the intercept value for this plot provides the value for the off-rate constant 0.94 ± 0.84 s^{-1}. A similar approach applied to Aβ40 peptide and α-Syn produced lifetime values for in the same range, suggesting that this incredibly long lifetime for transient dimers is a general phenomenon for amyloid proteins [35, 36].

2.3.2. MD Simulations: The Structure of Monomer.

Conformational properties of Aβ(13-23) both in monomeric and dimeric forms were studied by MD simulations. First, the structural dynamics of the peptide in monomeric form was studied using three different initial structures (Figure 2.3A). Initial structures for I, II, and III are essentially random meander, α- helix, and fully extended β-sheet conformation, respectively. Regardless of the different conformations from initial structures, central structures (Figure 2.3B) of the largest cluster of structures from the 200 ns trajectories are rather similar (Figure 2.4). Intramolecular interactions, such as hydrogen bonds (yellow dotted lines) between His14-Leu17 and Gln15-Val18 in structure III, are formed to stabilize a β-turn structure (Figure 2.3B).

The similarities between the conformational spaces that the peptide explores in the three independent simulations are further supported by the high RMSIP values for the

first 10 eigenvectors of simulations I−III (Table 2.1). The DSSP analysis [16] (Figure 2.5) reveals that the peptide structure is flexible and assumes various conformations, but in each trajectory, a similar conformational space is explored as shown by the Ramachandran plots (Figure 2.6). The Radius of gyration (Rg) and root-mean-square deviation (RMSD) (Figure 2.7 and 2.8, respectively) indicate that the peptide has flexible conformations and follows a different folding−unfolding path. Rg (Figure 2.7) demonstrates that geometrically compact structures with average Rg ≈ 0.62 nm are formed during each simulation. The mean RMSD value for simI and simII is ∼0.4 nm, while it is ∼0.8 nm for simIII (Figure 2.8). The high RMSD values show that the peptide assumes substantially different conformations from those of the initial structures.

Overall, the MD simulations show that the structure of Aβ(13-23) is flexible in aqueous solution in its monomeric form, and residues 4-9 are in the turn/bend conformation. Regardless of the different initial configurations, all the structures eventually converge to a conformation in which residues 4-9 form a turn. Furthermore, during simulations, the peptide did not adopt a fully extended β-sheet type conformation.

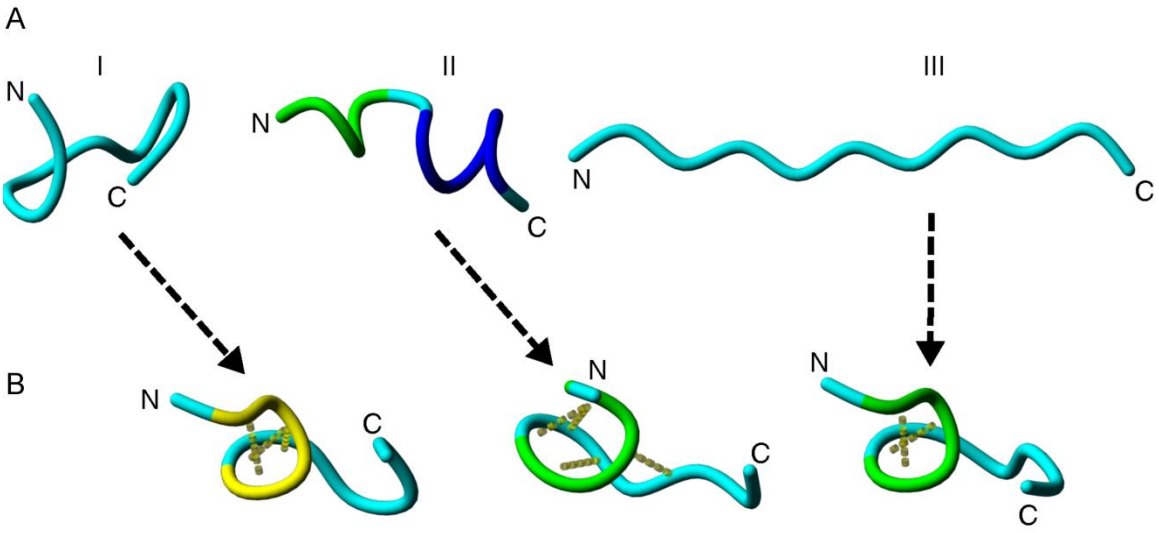

Figure 2.3. Initial and central structures of MD simulations of monomer structures I−III. (A) Tube representations of the backbone of the initial structures I−III for the three independent MD simulations. (B) The central structure of the largest cluster of the simulations. Random meander is cyan; α-helix is dark blue; 3_{10}-helix is yellow; turn is green; and H-bonds are indicated by yellow dotted lines. N and C indicate N- and C-termini, respectively.

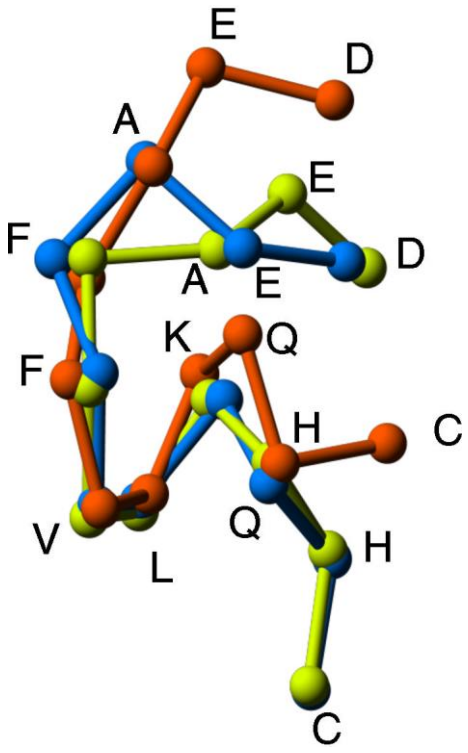

Figure 2.4. Overlaid representative Cα trace structure of the largest cluster of simulation I, II and III. Blue, simulation I; Red, simulation II; Green, simulation III.

Table 2.1. RMIP value of the 10 largest eigenvectors between three simulations

	0-50 ns	50-100 ns	100-150 ns	150-200 ns
I-II pair	0.7589	0.7363	0.7248	0.6656
II-III pair	0.7698	0.7702	0.7973	0.7212
I-III pair	0.7859	0.7757	0.7835	0.7509

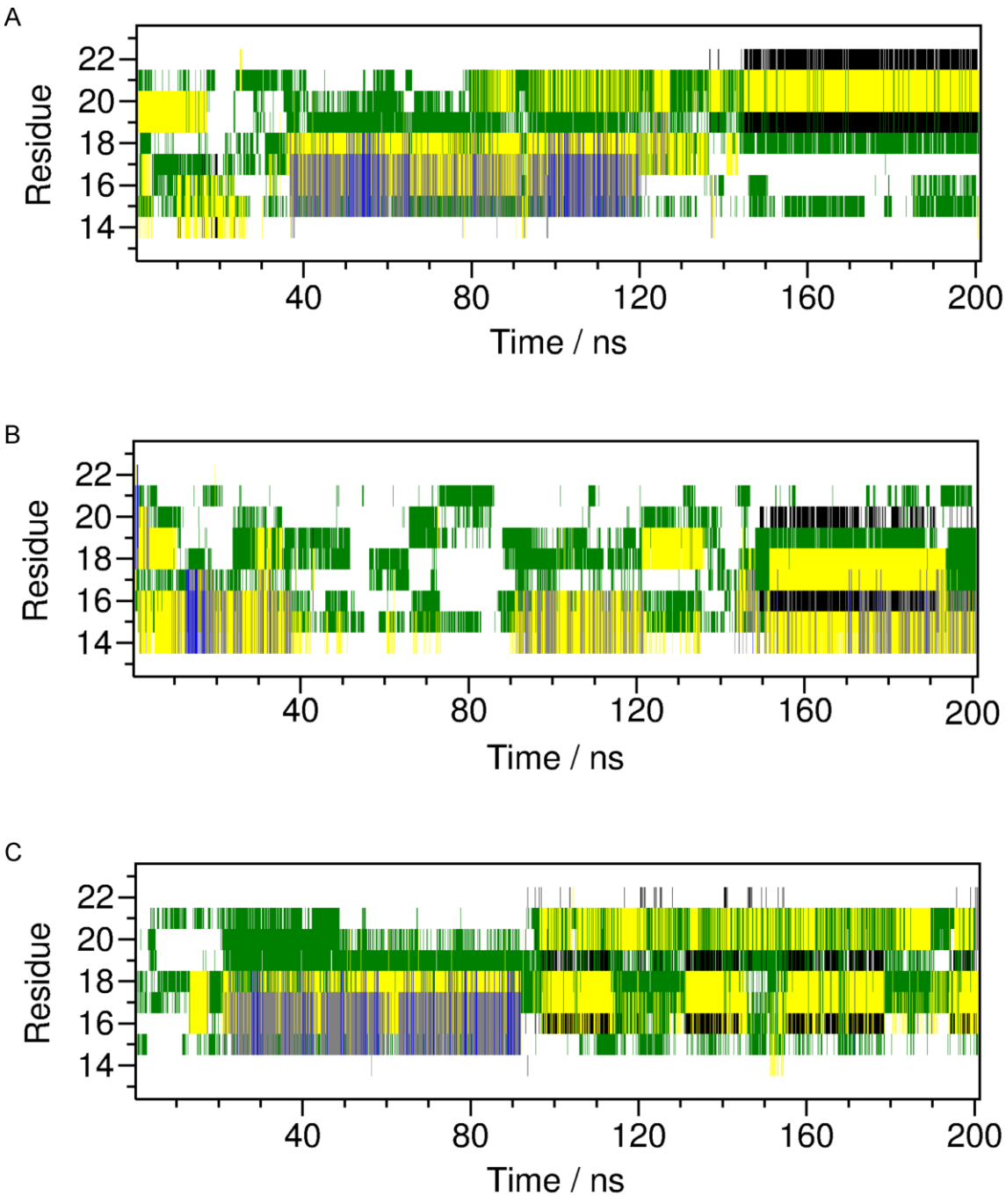

Figure 2.5. DSSP analysis of the trajectories of simulations I-III of Ac-[Cys13]Aβ(13-23)-NH2. (A) simI. (B) simII. (C) simIII. Random meander is white, β-bridge is black, β-bend is green, β-turn is yellow, α-helix blue and 3_{10}-helix is gray.

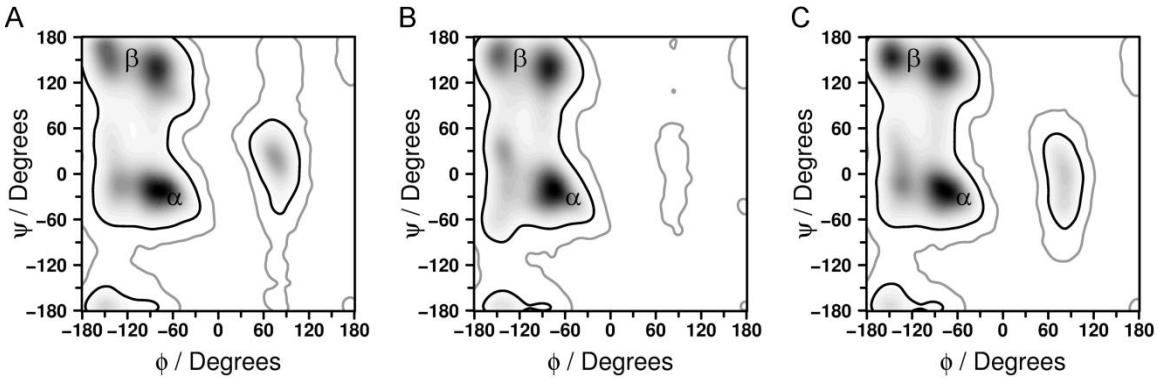

Figure 2.6. Ramachandran plot for simulations I-III. (A-C) are from simI, simII and simIII, respectively. The dark regions indicate the conformation explored during simulations. α-helix and β-sheet conformations are labeled. Gray line indicates allowed (99.95% contour level) and black line indicates favored (98% contour level) regions of conformational space [18].

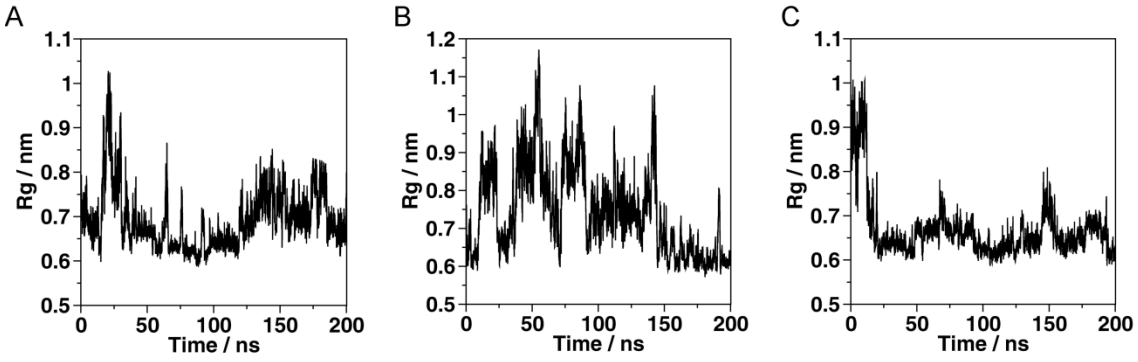

Figure 2.7. The radius of gyration (Rg) of the peptide in simulations I-III. (A-C) are from simI, simII and simIII, respectively.

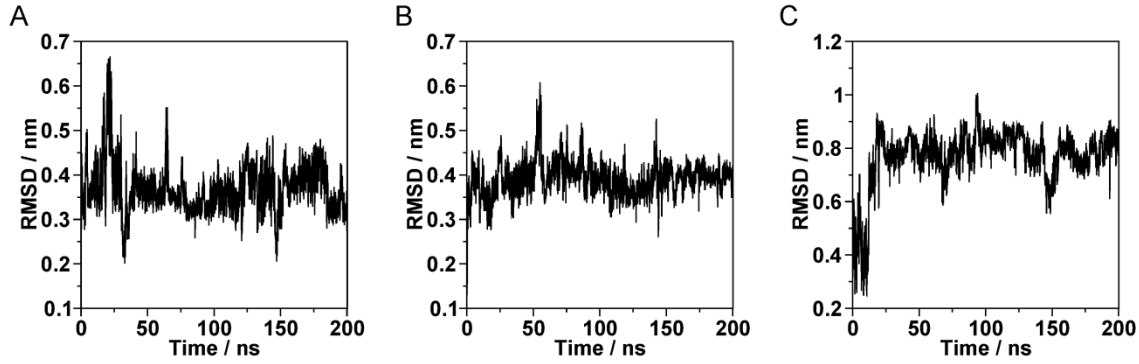

Figure 2.8. The RMSD of the backbone of atoms in simulations I-III. (A-C) are from simI, simII and simIII, respectively.

2.3.3. MD Simulation of the Structure of Dimer

Next, we considered how the conformation of the peptide changes when it interacts with another peptide chain. We selected the central structure of the largest cluster of simIII (Figure 2.3B) and placed monomers A and B in a parallel arrangement so that the minimal distance between the two chains was ≥ 1.5 nm. To follow the relative orientation of the two monomers, the distance between COM13A and COM13B was plotted for the 400 ns MD simulation (Figure 2.9). During the initial 50 ns period, the distance fluctuates at 1.5 nm, and the peptide chains retain their initial conformations (structures 1 and 2 in Figure 2.9A). Between 50 and 200 ns, the two Cys residues approach, and the distance between COM13A and COM13B fluctuates at 0.5 nm. The secondary structure of the two chains resembles that of the initial (structure 1 in Figure 2.9A) and is more stable than it was during the simulations of the monomer (Figures 2.5 and 2.10). Between 200 and 300 ns, the two monomers move apart, and their orientation changes to antiparallel (structures 4 and 5 in Figure 2.9A). After 350 ns, this rearrangement results in the formation of a stable antiparallel β- sheet conformation (structures 6 in Figure 2.9A). The structural transition of the dimer is further demonstrated during the synchronous change of the distance between COM13A and COM13B by a sudden increase and decrease of the radius of gyration (Figure 2.11). Changes in intermolecular interactions closely follow the structural transitions, and the formation of an antiparallel β-sheet conformation results in the lowest interaction energy state (Figure 2.9B). The central backbone structure of the largest cluster of the last 50 ns of the MD simulation is shown in Figure 2.9C. The intermolecular interactions of

monomers were therefor seen to trigger conformational changes within the individual peptide chain, which led to the formation of the antiparallel β-sheet structure.

The MD results provide insight into the interactions that stabilize the structure of the dimer. During the first 200 ns of the simulation, the monomers within the dimer are held together by hydrophobic interactions, by hydrogen bonds between Phe19 of monomer A and Gln15 of monomer B, between the two Cys residues (Figure 2.12), and by the aromatic−aromatic (Ar-Ar) interaction between Phe19 of monomer A and Phe20 of monomer B (Figure 2.13A). After 320 ns, the antiparallel β-sheet conformation is found to be formed and stabilized by four hydrogen bonds between residues His14 of monomer A and Phe19 of monomer B, and between Lys16 of monomer A and Leu17 of monomer B (Figure 2.9C). Additional stabilization is provided by salt bridges between Lys16 of monomer A and Asp23 of monomer B, between His14 of monomer A and Glu22 of monomer B, an aromatic−backbone (Ar-bb) interaction between Phe19 of monomer B and the backbone of His14 and Gln15 of monomer A (data not shown), and an aromatic-CH (Ar-CH) interaction between Phe19 of monomer B and CβH groups of His14 of monomer A (Figure 2.13B). The change from Ar-Ar interaction to Ar-CH interaction coincides with the switching of the orientations of monomers from parallel to antiparallel (Figure 2.9 and Figure 2.13).

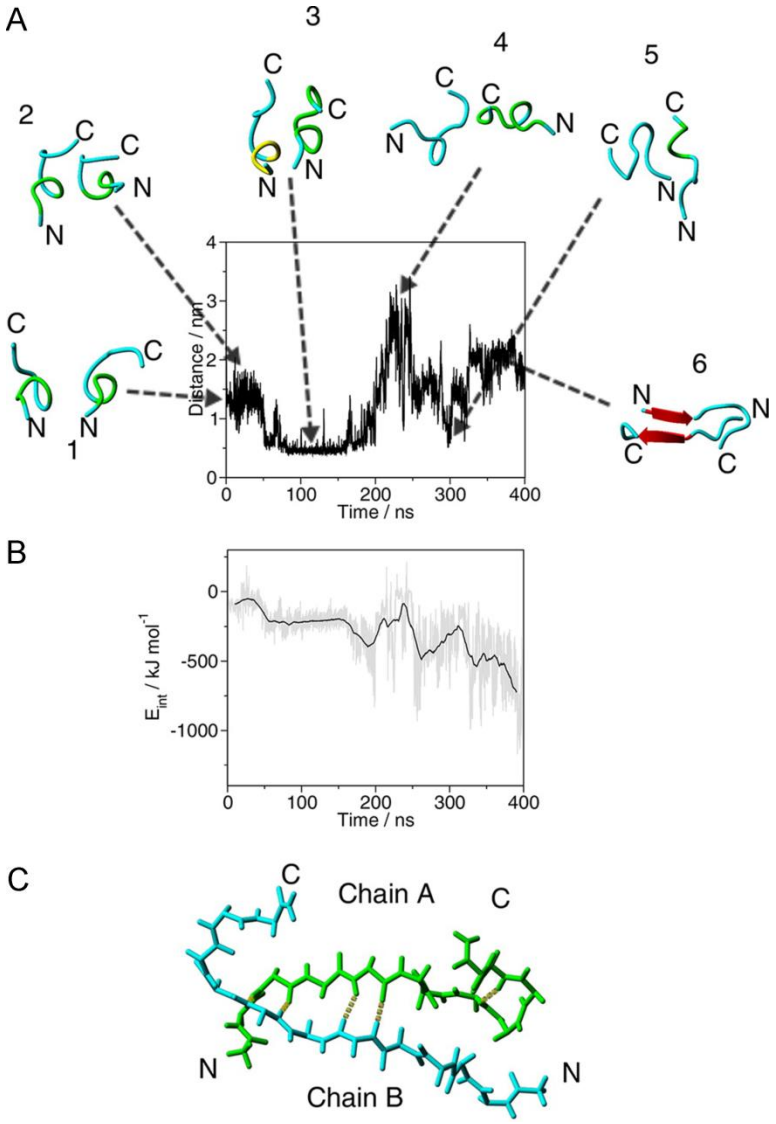

Figure 2.9. Evolution of the distance between the center of mass of Cys13 of chain A and the center of mass of Cys13 of chain B during the 400 ns MD simulation of the dimer structure. Snapshots of the dimer backbone structures from the trajectory are placed inside the plot. (A) 1, 0 ns; 2, 20 ns; 3, 97.9 ns; 4, 221 ns; 5, 300 ns; 6, 359 ns. Backbone conformation of the peptide chain is as follows: cyan is random meander; yellow is 3_{10}-helix; green is β-turn/bend; red arrow is β-sheet; and H-bonds are yellow dotted lines. N and C indicate the N-and C-termini, respectively. (B) Intermolecular interactions (E_{int}) during the 400 ns MD simulation of the dimer structure. The gray line shows E_{int} at every 10 ps, and the black line is the running average at 5 ns intervals. (C) Antiparallel backbone structure of the central structure of the largest cluster of the last 50 ns of the MD simulation. In chain A, the backbone carbon atoms are in green. H-bonds are yellow dotted lines. N and C indicate the N-and C-termini, respectively.

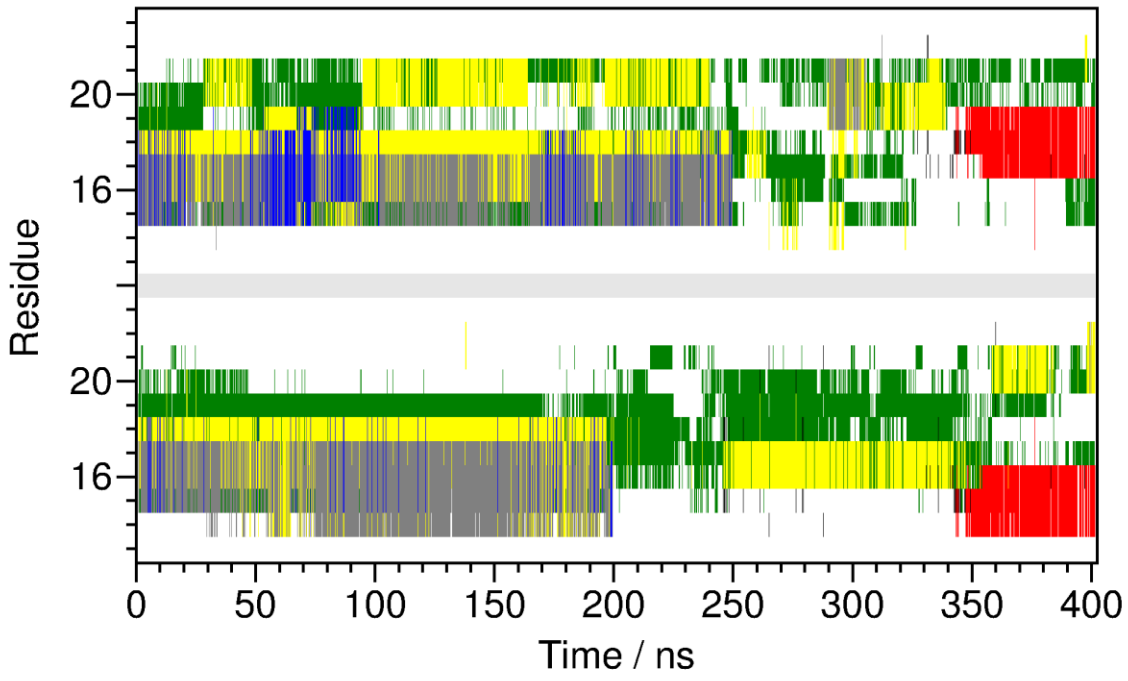

Figure 2.10. DSSP analysis of 400 ns trajectory of the dimer simulation. Bottom panel, chain A; top panel, chain B. White is coil, black is bridge, green is bend, yellow is β-turn, blue is α-helix, gray is 3_{10} helix and red is β-sheet. The two chains are separated by a light gray ribbon.

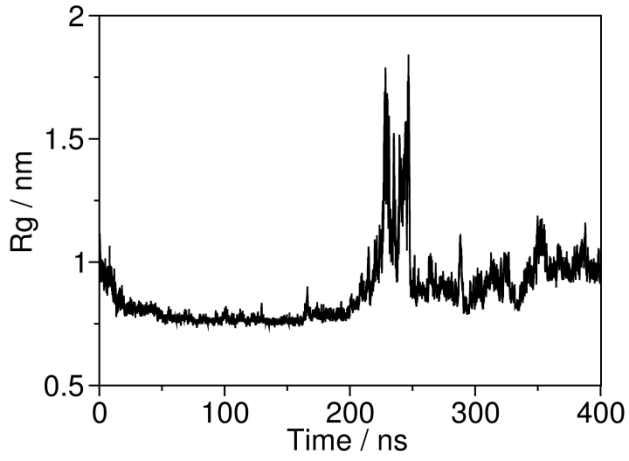

Figure 2.11. The radius of gyration (Rg) of the dimer during the 400 ns simulation.

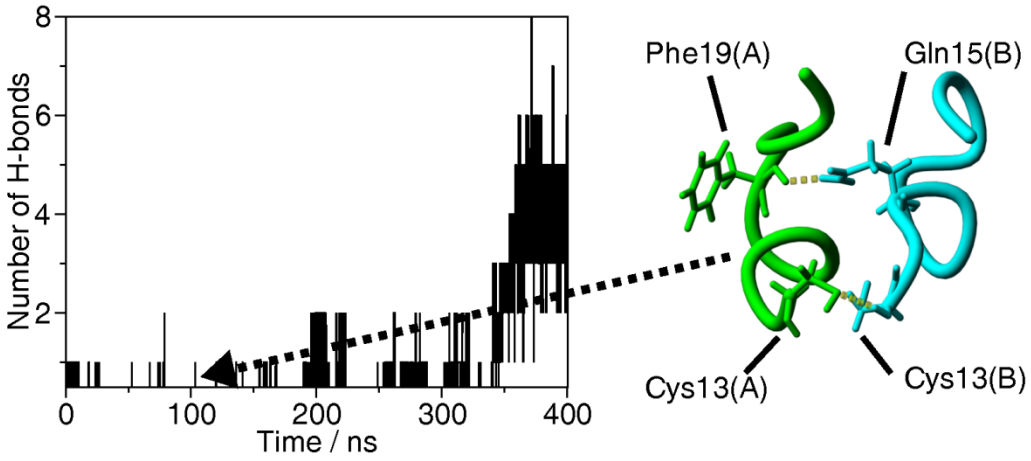

Figure 2.12. Number of hydrogen bonds during MD simulation of the dimer structure. The inserted structure shows H-bonds between the two Cys residues and between the amide H of Phe19 of chain A and the side chain of Gln15 of chain B.

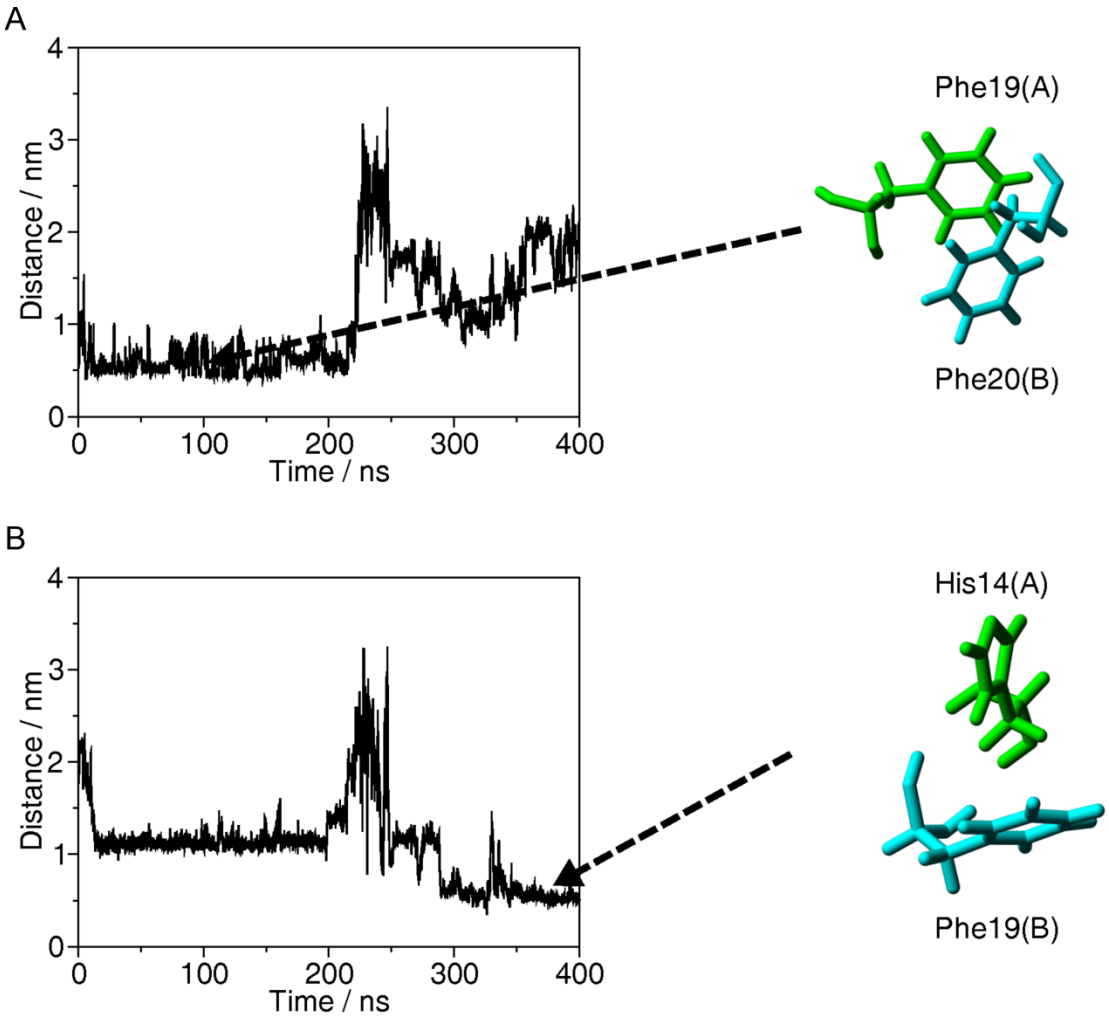

Figure 2.13. The weakly polar interactions during MD simulation of the dimer structure. (A) the distance of Phe19 of chain A and Phe20 of chain B. (B) the distance between CβH of His14 of chain A and Phe19 of chain B. On the left side of the figure are snapshots from the trajectory which illustrate these interactions.

2.3.4. Steered MD Simulation of the Force-Induced Rupture of the Dimer.

To analyze the stability of the structure of the dimer, we used SMD simulation to examine the force-induced dissociation of the dimer. The dimer was pulled apart by applying external forces to the center of mass of Cys13 of monomer A at a constant rate 5 nm/ns (Figure 2.14A). This led to the clear rupture event characterized by the force curves (Figure 2.14B and C). The force−distance curve (Figure 2.14C) shows that the rupture event occurred at the 2.6 nm distance between the center of mass of the two Cys residues, corresponding to a force of ∼1000 pN.

Figure 2.15 shows the force-induced dissociation pathways of the dimer. The initial segment of the force curve prior to the rupture event (0 ns−0.48 ns, 0−2.6 nm in Figure 2.14B and C) corresponds to the change in orientation of the dimer (models 1 to 3 in Figure 2.15A) and the loss of interpeptide H-bonds (Figure 2.15B). The major peak of the force curve in Figure 2.14 corresponds to the cooperative rupture of H-bonds in the time scale between 0.48 and 0.49 ns (models 2 to 4 in Figure 2.15A). From that point, chains of both monomers A and B slide past each other along the direction of the applied force. At 0.54 ns (model 6 in Figure 2.15C; 3.1 nm distance between the center of mass of the Cys residues in Figure 2.14C), the salt bridge between His14 of monomer A and Glu22 of monomer B ruptures (data not shown). However, the salt bridge between Lys16 of monomer A and Asp23 of monomer B exists for much longer and is essentially the last interpeptide interaction to break. Models in Figure 2.6C illustrate this process and the time dependent changes in the distance between the centers of mass of $\varepsilon NH\,3^{+}$ of Lys16 of monomer A and βCOO^{-} of Asp23 of monomer B (Figure 2.15D). Figure 2.15E and F show the time-dependent variation of the dimer structure with a focus on the aromatic

interactions. Snapshots of various structures along the force curve are shown in Figure 2.15E, and the graph illustrating the increase in the distance between the CβH group of His14 of monomer A and the center of the phenyl ring of Phe19 of monomer B is shown in Figure 2.15F. The rupture of this interaction corresponds to the minor peak seen between 0.6 and 0.7 ns on the force curve (Figure 2.14B).

In an additional SMD simulation, the dimer was the central structure of the largest cluster from the first 200 ns of the trajectory (structure 3 in Figure 2.9A). In this dimer, the chains have β-turn/bend conformations in a parallel orientation (Figure 2.16A). The force curve (Figure 2.16B) did not show a single characteristic rupture event. This further indicates that in AFM experiments the dimer is in antiparallel β-sheet conformation.

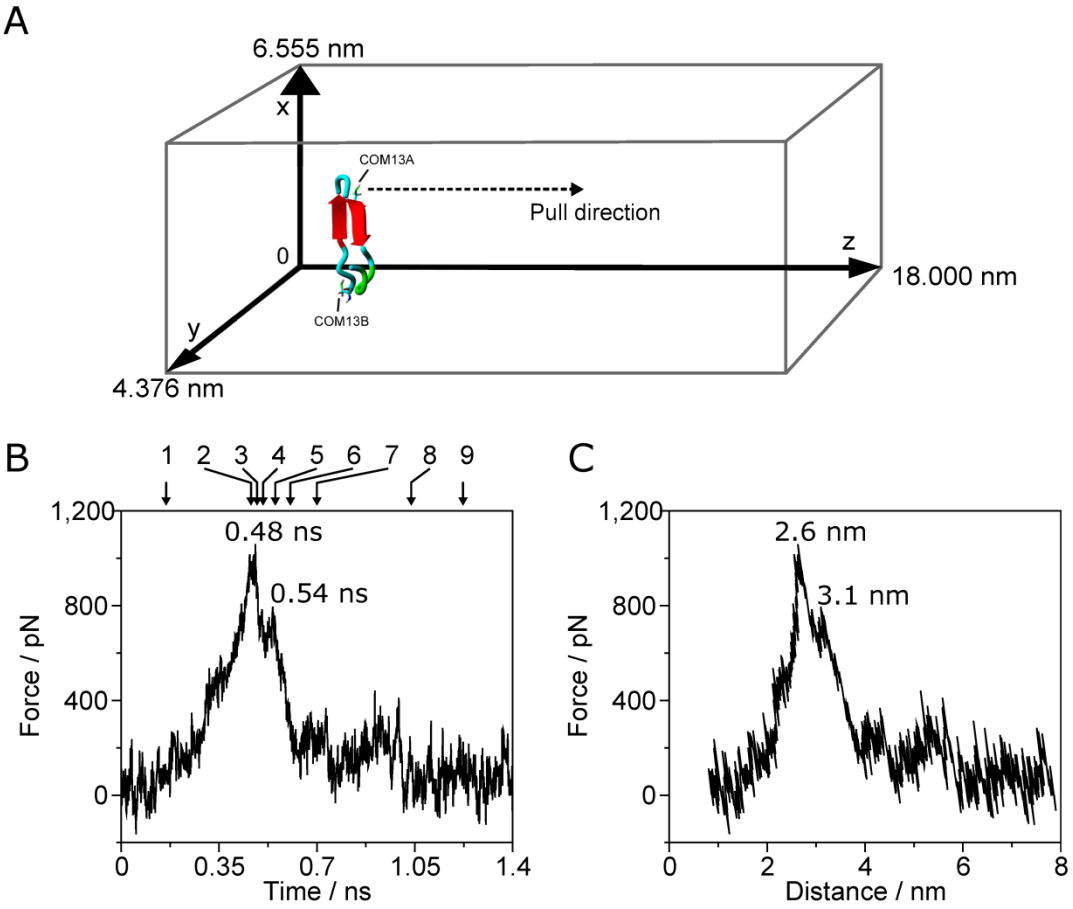

Figure 2.14. Force curves acquired at 5 nm/ns pulling rate from SMD simulation. (A) Pulling the center of mass of Cys13 of monomer A (COM13A) along the z-axis. The central structure of the largest cluster of the last 50 ns of the MD simulation of the dimer is in a rectangular box. For clarity, the water molecules are not shown. The dimension of the box is 6.555 nm × 4.376 nm × 18 nm. The pulling direction is indicated by a dashed arrow. Backbone conformation of the peptide chain is as follows: cyan is random meander; green is β-turn/bend; and red arrow is β-sheet. Numbers inside the force curve panels indicate the time (B) and distance (C) locations of the characteristic peaks. Arrows and numbers on panel B indicate the snapshots in Figure 2.15.

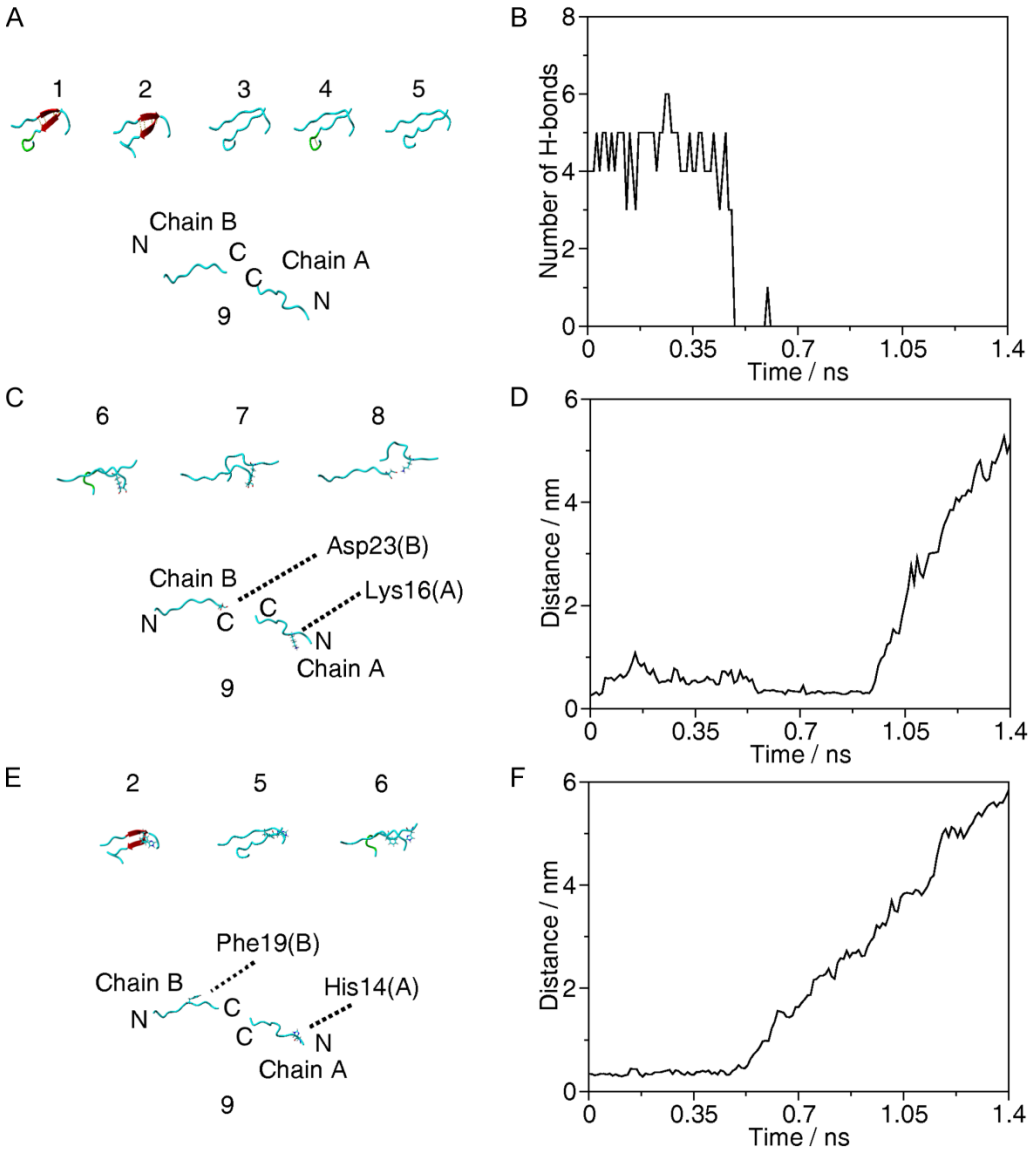

Figure 2.15. Force-induced dissociation pathway of the dimer structure during SMD simulation (5 nm/ns pulling rate). The snapshots of dimer structure are from 1, 0.2 ns; 2, 0.48 ns; 3, 0.49 ns; 4, 0.5 ns; 5, 0.54 ns; 6, 0.6 ns; 7, 0.7 ns; 8, 0.9 ns; and 9, 1.2 ns of the SMD trajectory. The numbers correspond to the position numbers shown in Figure 2.5B. (A) H-bond breaking. The red arrow indicates β-sheet structure, and H-bonds are yellow dotted lines. N and C indicate the N- and C-terminal ends, respectively. (B) Changes in the number of interchain H-bonds. (C) Force induced dissociation of the interchain salt bridge between Lys16 of chain A and Asp23 of chain B. (D) Distance between the center-of-masses of $\varepsilon NH3^{+}$ of Lys16 of chain A and βCOO^{-} of Asp23 of chain B groups. (E) Weakly polar interaction between the side chain of Phe19 of chain B and side chain of His14 of chain A. (F) Distance between the CβH group of His14 of chain A and the center of the phenyl ring of Phe19 of chain B.

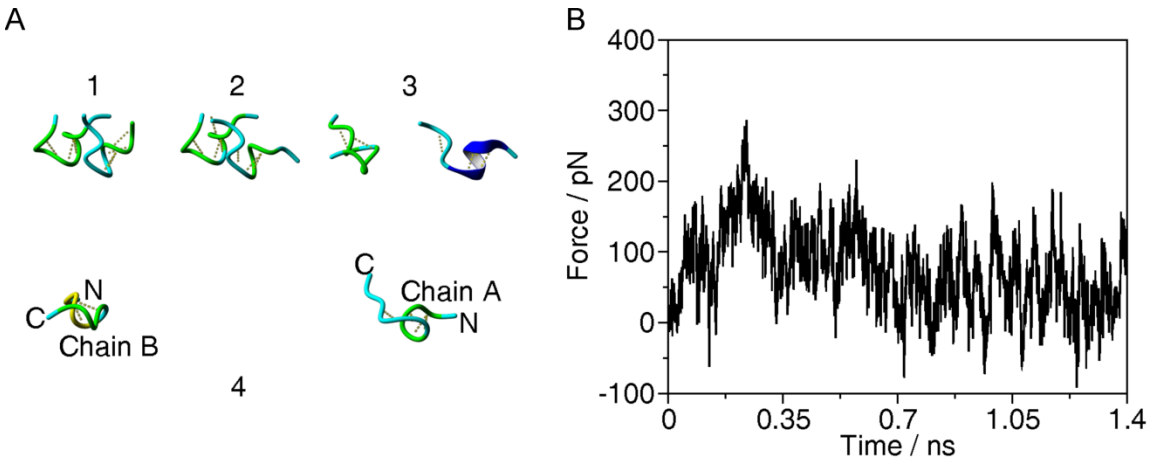

Figure 2.16. Force-induced dissociation pathway of the dimer structure of the central structure of the most populated cluster during the first 200 ns of the simulation of structure of the dimer during SMD simulation (5 nm/ns pulling rate). (A) The snapshots of dimer structure are from 1, 0 ns; 2, 0.2 ns; 3, 0.6 ns; 4, 1.4 ns of the SMD trajectory. Cyan indicates random meander; green represents β-turn and H-bonds are yellow dotted lines. N and C indicate the N- and C-terminal ends, respectively. (B) Force curves acquired from SMD simulation.

2.3.5. Energetics of the Dimer Rupture: Umbrella Sampling Simulations

We used umbrella sampling simulations [29-31] to determine the one-dimensional Potential of Mean Force (PMF) curve along the ξ reaction coordinate and to calculate the free energy of binding ($\Delta G_{bindA,B}$) between monomers (Figure 2.17). The umbrella histograms and PMF curve (Figure 2.17) were obtained using the method of Weighted Histogram Analysis (WHAM) [32-34]. At a large distance between COM13A and COM13B ($\xi > 5$ nm), the PMF curve is flat, and it was selected as the zero reference point. At the 2.6 nm $\leq \xi \leq$ 2.9 nm region, the PMF curve is flat, and it corresponds to the main rupture event (see Figure 2.14B and C). Therefore, the main rupture is accompanied by $\Delta G^1_{bindA,B} = -49.52$ kJ/mol, and the subsequent dimer dissociation has $\Delta G^2_{bindA,B} = -35.93$ kJ/mol changes. $\Delta G^1_{bindA,B}$ corresponds to the breaking of H-bonds and the salt bridge between His14 of monomer A and Glu22 of monomer B, whereas $\Delta G^2_{bindA,B}$ is the free energy change associated with the breaking of weakly polar interactions and a salt bridge between Lys16 of monomer A and Asp23 of monomer B. Overall, a $\Delta G_{bindA,B}$ of −85.45 kJ/mol suggests that the interaction between the monomers in the dimer is strong. The uneven distribution of the umbrella histograms at 2.0 nm $\leq \xi \leq$ 3.0 nm indicates that during the SMD simulation, before and after the major rupture peak, the number of interchain interactions in neighboring umbrella windows vary substantially and change quickly; therefore, the probability of configuration exchange between the windows is low.

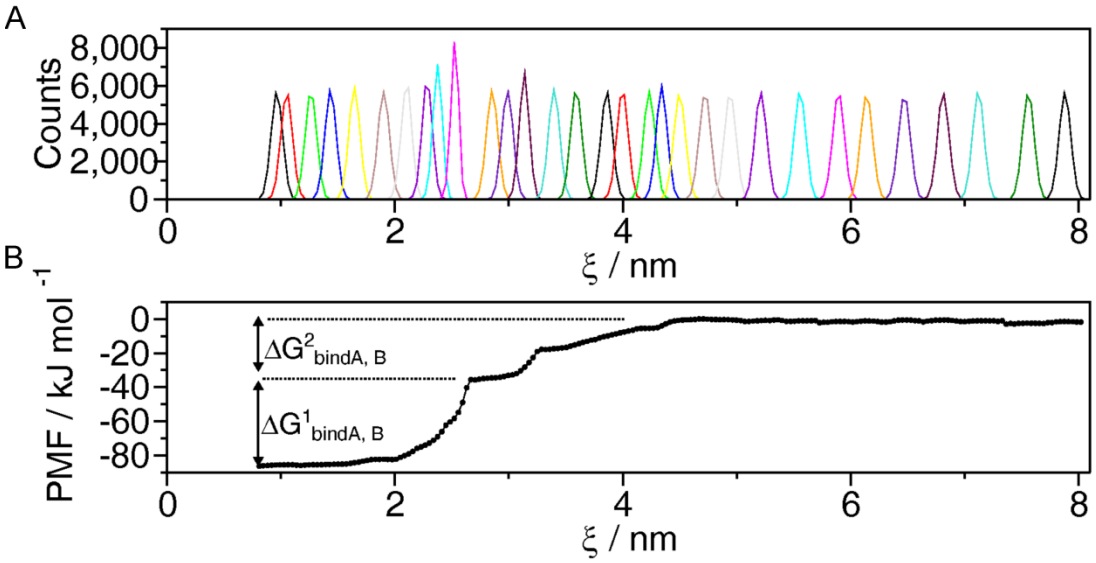

Figure 2.17. WHAM analysis of the umbrella sampling simulation. (a) Converged umbrella histograms of 31 configurations, each derived from 20 ns simulation. (b) Potential of mean force (PMF). ΔG^{1}bindA,B corresponds to H-bonds and salt bridge breaking, and ΔG^{2}bindA,B is associated with the breaking of weakly polar interactions and a salt bridge.

2.4. DISCUSSION

In our recent model of amyloid aggregation, the misfolded state of amyloid proteins, including Aβ-peptides, is stabilized by the formation of dimers [35, 36]. The model supported by AFM force spectroscopy studies demonstrates that the dimers are characterized by lifetimes as large as seconds. However, the structure and mechanism of formation of misfolded dimers remained unclear. In this work, we showed that isolated monomers have characteristic conformational features that differ from those in aggregated or fibril states. However, substantial changes in the peptide structure were observed when the two monomers interacted to form a dimer. The formation of an antiparallel β-sheet was detected after a series of conformational transitions within each monomer (Figure 2.9). The dimer is only stable when the two monomers are in antiparallel orientation. SMD simulation showed that individual peptide chains under the applied force undergo a structural transition that is accompanied by sharp rupture of the dimer; this is in agreement with AFM experiments.

2.4.1. Structure and Dynamics of the Peptide.

On the basis of earlier MD simulations, the conformations of short Aβ fragments were considered to be in random coil [37, 38] or polyproline II structures [39, 40]. For Aβ(1-28), it was shown that residues 13-21 have a high propensity for α-helical conformations in the monomeric state [41]. During our monomer simulations, Aβ(13-23) was initially assumed to have a 3_{10}-helix conformation at residues 14-17 which then converted to β-turn/ bend and random meander conformations. Since the

sequence of the peptide here is shorter than that in the work of Rojas and associates [41], a stable helical conformation is not expected but rather a flexible structure that interconverts between different conformational types. The three different initial conformations for the peptide were selected from known experimental amyloid β structures, and over time, all three converged to similar conformations. In the antiparallel β-sheet structure, the N-terminal Cys residue neither formed any intramolecular interactions nor participated in the formation of any secondary structures and, therefore, was an appropriate anchoring group for the AFM experiments.

During REMD simulations of the structure of Aβ(16-22) dimer by Gnanakaran and associates, six different low energy structures occurred between 275 and 510 K [40]. The individual chains did not prefer any particular secondary structure, and both parallel and antiparallel orientations occurred. In our dimer simulation, the conformations of the monomers and the structures of the dimer were initially similar to those observed by Gnanakaran and associates [40]. As the simulation proceeded the dimer assumed a stable antiparallel β-sheet structure after several structural transitions. Furthermore, during two additional long-time simulations of the dimer structure, using two different force fields, a stable antiparallel β-sheet structure was also observed (Figures 2.18-20). The stability could be due to the longer chain length and to the presence of His14, which was shown to be important for aggregation [42]. Here, we showed that His14 forms an interchain weakly polar Ar-CH interaction that stabilizes the dimer (Figures 2.15E, F and 2.13B). The aggregation of Aβ(16-22) was studied in trimer form using relatively short (10 ns) MD simulations [37]. The stable association of the chains was accompanied by a conformational transition of the individual chains from a β-turn to

β-strand structure. The oligomer did not have the antiparallel β-sheet structure, most likely due to the short simulation time. Nguyen and associates, using 50 ns REMD simulations [43], showed that the free energy landscape of the dimer of Aβ(16-22) is complex and that only 25% of the total population have the antiparallel β-sheet structure, which is again most likely due to the short length of the peptide. REMD simulations of dimerization of Aβ(11-25) at three different pH values revealed a dynamic interplay between hydrophobic, electrostatic, and solvation intertactions [44]. At pH 8.4, the free energy landscape for the peptide is complex, although most of the low energy structures are in antiparallel β-sheet conformation. Here, we also observed that the dimer has dynamic structure but can form stable antiparallel β-sheet conformation.

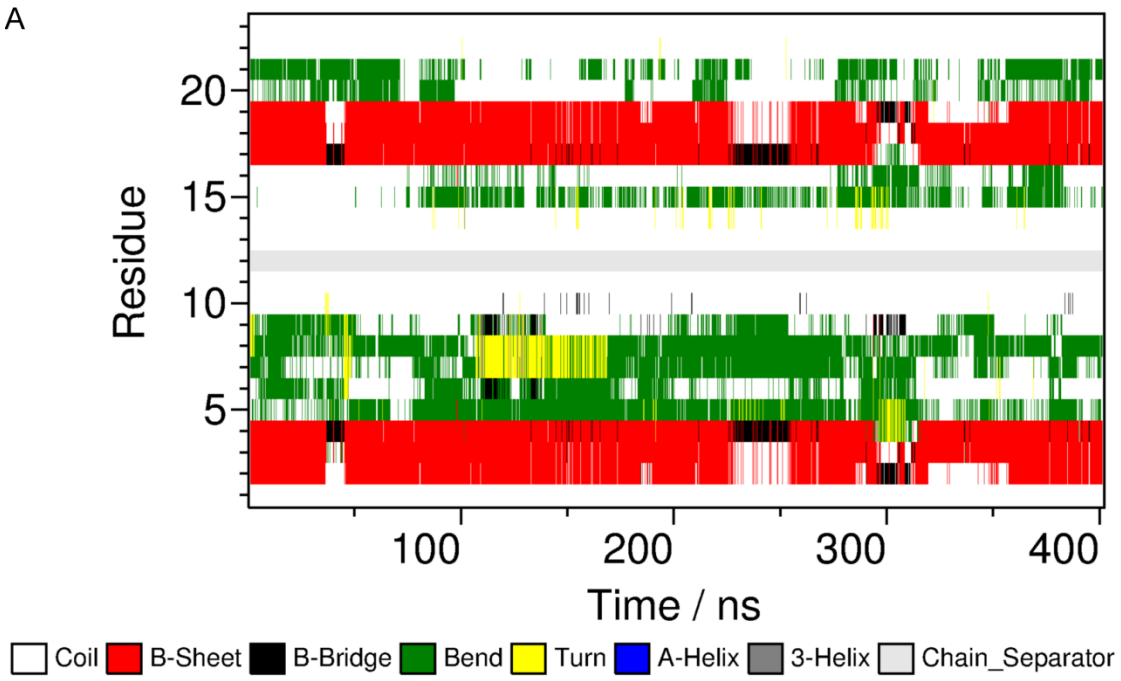

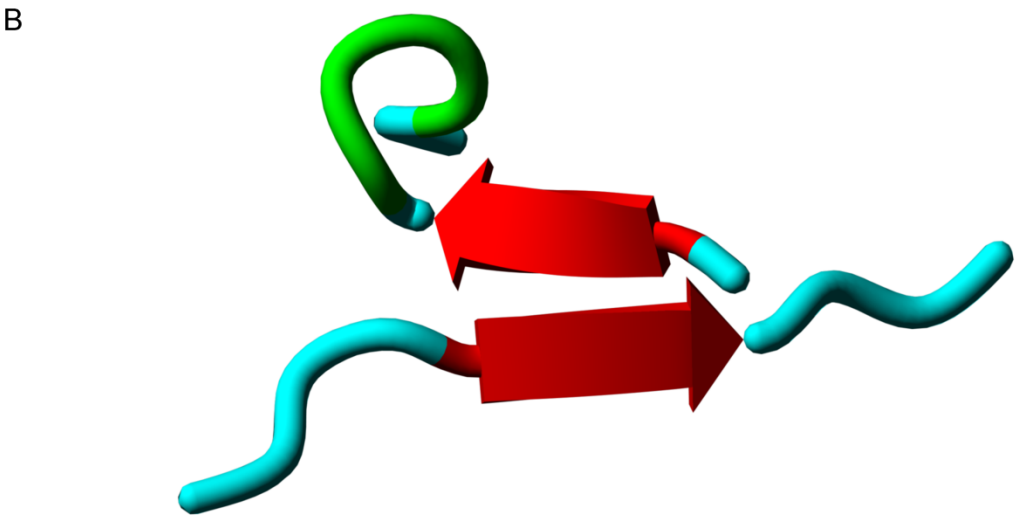

Figure 2.18. MD simulation using the OPLS-AA/L force field. (A) DSSP analysis of the trajectory. Bottom panel, chain A; top panel, chain B. White is coil, black is bridge, green is bend, yellow is β-turn, blue is α-helix, gray is 3_{10} helix and red is β-sheet. The two chains are separated by a light gray ribbon. (B) Representative structure of the largest cluster. The snapshot is taken from the trajectory at 114.2 ns. Backbone conformation of the peptide chains is as follows: cyan is random meander; green is β-turn/bend, red arrow is β-sheet and H-bonds are yellow dotted lines.

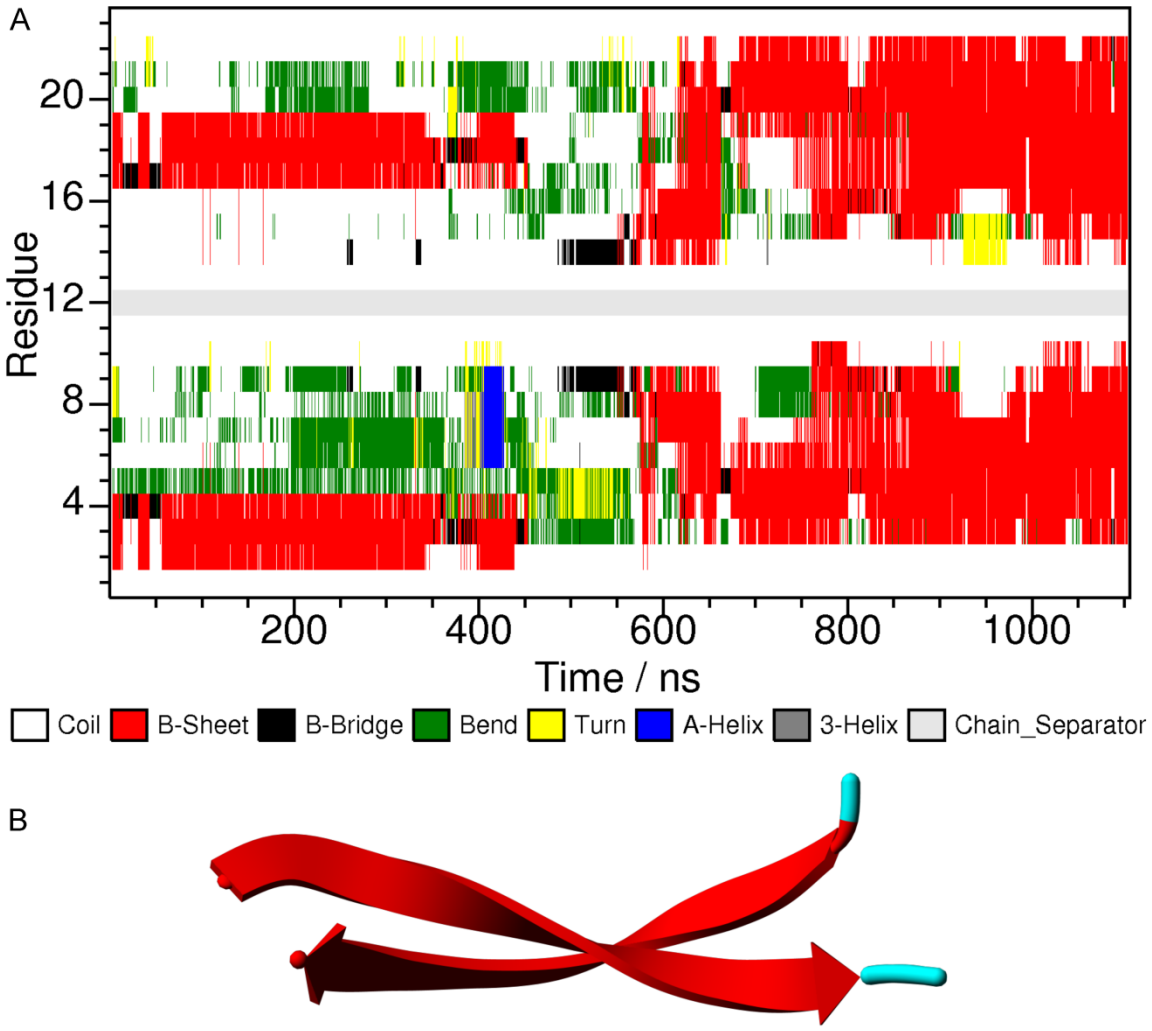

Figure 2.19. MD simulation using Amber-ff99sb*-ILDN force field (A) DSSP analysis of the trajectory. Bottom panel, chain A; top panel, chain B. White is coil, black is bridge, green is bend, yellow is β-turn, blue is α-helix, gray is 3_{10} helix and red is β-sheet. The two chains are separated by a light gray ribbon. (B) Representative structure of the largest cluster. The snapshot is taken from the trajectory at 1003.7 ns. Backbone conformation of the peptide chains is as follows: cyan is random meander, red arrow is β-sheet and H-bonds are yellow dotted lines.

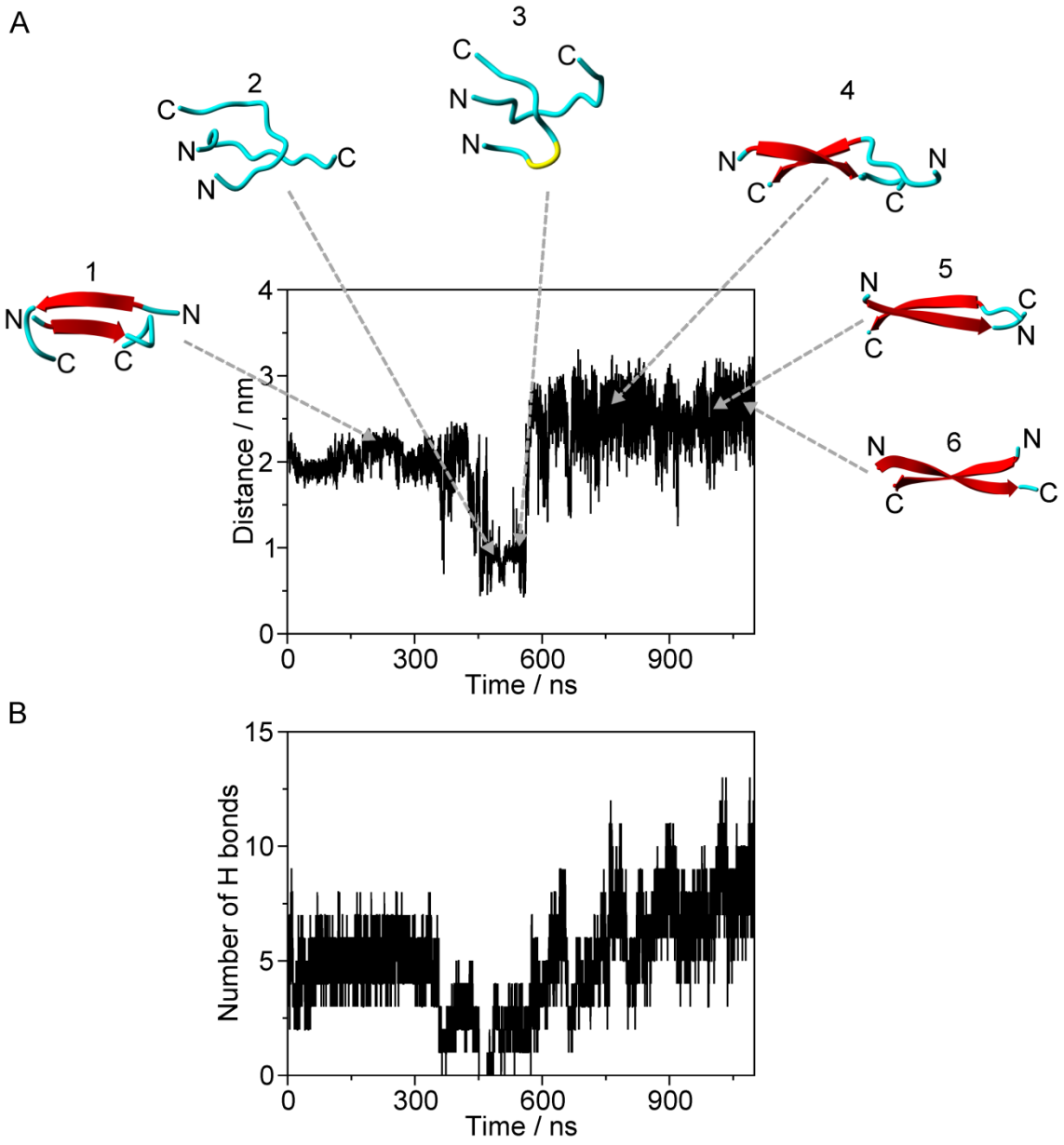

Figure 2.20. (A) The distance between the center of mass of Cys13 of chain A and the center of mass of Cys13 of chain B in during the 1.1 μs MD simulation of the dimer structure using Amberff99sb*-ILDN force field. Snapshots from the trajectory are placed inside the plot. 1, 200 ns; 2, 480 ns; 3, 510 ns; b, 750 ns; 5, 1000 ns; 6, 1003.7 ns. Cyan is random meander; yellow is turn; red arrow is β-sheet. N and C indicate the N-and C-termini, respectively. (B) Number of hydrogen bonds during MD simulation of the dimer structure using Amber-ff99sb*-ILDN force field.

The dimer has dynamic structure and typically 4 to 5 H-bonds are present during simulations. Nevertheless, after the antiparallel β-sheet structure was formed, it was not disrupted until the end of the simulation. Furthermore, the ionization state of the side chains was set as at pH 7, and only the Lys residues were protonated. Subsequently, the dimer was further stabilized by ionic interaction between Lys16 of chain A and Asp23 of chain B. Weakly polar interactions could substantially stabilize the polypeptide structure because their strength can be as strong as that of H-bonds [45-49]. Here, we observed the Ar-bb interaction between Phe19 of chain B and the backbone of the His14-Gln15 of chain A and an Ar-CH interaction between Phe19 of chain B and CβH groups of His14 of chain A. These interactions clearly contributed to the stabilization of the antiparallel β-sheet structure of the dimer.

2.4.2. Stability of the Dimer

The stability of preformed Aβ dimers and fibrils was studied by pulling the center of mass of one chain and keeping the rest of the complex constrained [50, 51]. Here, we used a different approach to closely mimic the experimental AFM procedure. Residue 13 of the peptide was replaced with Cys, and only the position of Cys13 of chain B was constrained, while Cys13 of chain A was pulled and the rest of the peptide chains were flexible. Subsequently, the main force-peak of SMD simulation, where the antiparallel β-sheet breaks up, corresponds to the rupture peak in force spectroscopy (compare Figures 2.2 and 2.5). If the structure was not an antiparallel β-sheet, the force curve from the SMD simulation would be different from that from force spectroscopy. When a pulling simulation was performed on a dimer with β-turn and random meander structures (Figure

2.16), the force curve was at the noise level of the SMD simulation of the antiparallel β-sheet structure clearly indicating that during AFM experiments, the antiparallel β-sheet dimer dissociates.

Our umbrella sampling simulations further indicate that the peptide forms a stable dimer that dissociates in two steps by showing a plateau on the free energy curve at a $\Delta G^{1}_{bindA,B}$ of −49.52 kJ/mol (Figure 2.17). A similar transient plateau was observed by Mothana and associates [50], although they overestimated the value of ΔG_{bind} by its calculation from only a single MD simulation. The large value of the overall free energy of binding ($\Delta G_{bindA,B}$ = −85.45 kJ/mol) indicates that a stable dimer is formed. This is further supported by the AFM experimental off-rate constant of 0.94 ± 0.84 s^{-1} for the lifetime of the dimer. The data clearly indicate that oligomerization of Aβ is initiated by the formation of stable dimers.

2.4.3. Molecular Model for Aβ Aggregation.

MD simulations of the process of Aβ peptides showed that monomers can adjust their conformation following docking to the prestructured oligomer [38, 41], and this process leads to elongation of the oligomer that eventually may lead to the formation of protofibrils. The mechanism of the formation of oligomers, however, remains unclear. Our studies fill this gap and lead to a model for the oligomerization. The AFM force spectroscopy data demonstrate that as the monomers approach the dimers are formed. The contact time is in the range of seconds. Since MD simulations show that the time for the formation of stable dimers is much shorter, ∼300 ns, the experimental conditions provide sufficient time for the formation of dimers during the AFM force

spectroscopy. The peptides in the dimer form antiparallel β-sheet conformation, and this conformation is similar to the conformation in fibrils of Aβ (14-23) [52], suggesting that the process of formation of dimers modeled here is the first step in the aggregation of the peptide.

Previously we proposed that the fibrils are assembled from dimers [35]. The evidence for this model was the long lifetime of dimers. Recent experimental data for the kinetics of oligomerization of Aβ peptides agree with this model [53, 54]. The assembly of monomers into dimers observed in this study and the docking of monomers to the preassembled oligomers [55-57] occur in nanoseconds, suggesting that the finding of partners is the time-limiting step of the oligomerization process. The β-sheet structure of the dimer found in our MD simulations on average has four hydrogen bonds. This is in agreement with the solid state NMR structure of Aβ(14-23) fibers [52]. In additional simulations (Figure 2.20A,B), a longer β-sheet structure was formed and stabilized by on average seven hydrogen bonds. However, for Aβ peptides it is possible that the β-sheet structure in the same region of residues with four to seven hydrogen bonds is transient and gradually can be transformed into longer β-sheet structures. If this does not happen within the Aβ dimer, the formation of higher order oligomers can stimulate this conformational transition. Furthermore, the monomers in Aβ(1-40) and Aβ(1-42) fibers are in parallel orientation [12, 58], but the orientation in dimers or higher order of oligomers remains to be determined. On the basis of our present data and recent publications [59-63] it is possible that Aβ dimers are in antiparallel orientation and

subsequent docking of monomers to dimers triggers an overall chain reorientation leading to fiber formation.

Overall, in this study, AFM and MD simulations are synergistically used to characterize the mechanism of misfolding and dimer formation of Aβ(13-23). Dynamic force spectroscopy analysis showed that the dimeric complex formed by the peptide is stable and dissociates typically in seconds. During MD simulations, isolated monomers gradually adopted characteristic conformational states forming a native ensemble that differed significantly from those in dimers or fiber state. When two monomers formed a dimer, their structure changed substantially and adopted an antiparallel β-sheet conformation. Conformational spaces of the monomers become restricted due to interchain interactions including hydrogen bonds, salt bridges, and weakly polar interactions of side chains. Under the applied force, the dimer as during the AFM experiments dissociated in a cooperative manner. Thus, misfolding of the Aβ peptide proceeds via a loss of conformational flexibility and formation of stable dimers suggesting their key role in Aβ aggregation process.

REFERENCES

[1] Santini, S., G. Wei, N. Mousseau, and P. Derreumaux. 2004. Pathway complexity of Alzheimer's beta-amyloid Abeta16-22 peptide assembly. Structure. 12:1245-1255.

[2] Balbach, J. J., Y. Ishii, O. N. Antzutkin, R. D. Leapman, N. W. Rizzo, F. Dyda, J. Reed, and R. Tycko. 2000. Amyloid Fibril Formation by Aβ16-22, a Seven-Residue Fragment of the Alzheimer's β-Amyloid Peptide, and Structural Characterization by Solid State NMR. Biochemistry. 39:13748-13759.

[3] Yu, J., S. Malkova, and Y. L. Lyubchenko. 2008. α-Synuclein Misfolding: Single Molecule AFM Force Spectroscopy Study. J. Mol. Biol. 384:992-1001.

[4] Yu, J., and Y. L. Lyubchenko. 2009. Early Stages for Parkinson's Development: α-Synuclein Misfolding and Aggregation. J. Neuroimmune Pharm. 4:10-16.

[5] Hess, B., C. Kutzner, D. van der Spoel, and E. Lindahl. 2008. GROMACS 4: Algorithms for Highly Efficient, Load-Balanced, and Scalable Molecular Simulation. J. Chem. Theory Comput. 4:435-447.

[6] Hatfield, M. P. D., R. F. Murphy, and S. Lovas. 2010. Molecular dynamics analysis of the conformations of a beta-hairpin miniprotein. J. Phys. Chem. B. 114:3028-3037.

[7] Hatfield, M. P. D., R. F. Murphy, and S. Lovas. 2010. VCD spectroscopic properties of the β - hairpin forming miniprotein CLN025 in various solvents. Biopolymers. 93:442-450.

[8] Kaminski, G. A., R. A. Friesner, J. Tirado-Rives, and W. L. Jorgensen. 2001. Evaluation and Reparametrization of the OPLS-AA Force Field for Proteins via Comparison with Accurate Quantum Chemical Calculations on Peptides†. J. Phys. Chem. B. 105:6474-6487.

[9] Berman, H. M., J. Westbrook, Z. Feng, G. Gilliland, T. N. Bhat, H. Weissig, I. N. Shindyalov, and P. E. Bourne. 2000. The Protein Data Bank. Nucleic. Acids. Res. 28:235-242.

[10] Zhang, S., K. Iwata, M. J. Lachenmann, J. W. Peng, S. Li, E. R. Stimson, Y. a. Lu, A. M. Felix, J. E. Maggio, and J. P. Lee. 2000. The Alzheimer's Peptide Aβ Adopts a Collapsed Coil Structure in Water. J. Struct. Biol. 130:130-141.

[11] Tomaselli, S., V. Esposito, P. Vangone, N. A. J. van Nuland, A. M. J. J. Bonvin, R. Guerrini, T. Tancredi, P. A. Temussi, and D. Picone. 2006. The α-to-β Conformational Transition of Alzheimer's Aβ-(1–42) Peptide in Aqueous Media is Reversible: A Step by Step Conformational Analysis Suggests the Location of β Conformation Seeding. Chembiochem. 7:257-267.

[12] Petkova, A. T., W. M. Yau, and R. Tycko. 2006. Experimental constraints on quaternary structure in Alzheimer's beta-amyloid fibrils. Biochemistry. 45:498-512.

[13] Jorgensen, W. L., and J. D. Madura. 1985. Temperature and size dependence for Monte Carlo simulations of TIP4P water. Molecular Physics. 56:1381-1392.

[14] Hess, B., H. Bekker, H. J. C. Berendsen, and J. G. E. M. Fraaije. 1997. LINCS: A linear constraint solver for molecular simulations. J. Comput. Chem. 18:1463-1472.

[15] Berendsen, H. J. C., J. P. M. Postma, W. F. van Gunsteren, A. DiNola, and J. R. Haak. 1984. Molecular dynamics with coupling to an external bath. J. Chem. Phys. 81:3684-3690.

[16] Kabsch, W., and C. Sander. 1983. Dictionary of protein secondary structure: Pattern recognition of hydrogen ‐ bonded and geometrical features. Biopolymers. 22:2577-2637.

[17] Team, R. C. 2011. R: A Language and Environment for Statistical Computing. R Foundation for Statistical Computing, Vienna, Austria.

[18] Lovell, S. C., I. W. Davis, W. B. Arendall Iii, P. I. W. de Bakker, J. M. Word, M. G. Prisant, J. S. Richardson, and D. C. Richardson. 2003. Structure validation by Cα geometry: ϕ,ψ and Cβ deviation. Proteins: Structure, Function, and Bioinformatics. 50:437-450.

[19] Daura, X., K. Gademann, B. Jaun, D. Seebach, W. F. van Gunsteren, and A. E. Mark. 1999. Peptide Folding: When Simulation Meets Experiment. Angew. Chem. Int. Edit. 38:236-240.

[20] Amadei, A., M. A. Ceruso, and A. Di Nola. 1999. On the convergence of the conformational coordinates basis set obtained by the essential dynamics analysis of proteins' molecular dynamics simulations. Proteins: Structure, Function, and Bioinformatics. 36:419-424.

[21] Lindorff-Larsen, K., P. Maragakis, S. Piana, M. P. Eastwood, R. O. Dror, and D. E. Shaw. 2012. Systematic Validation of Protein Force Fields against Experimental Data. PLoS One. 7:e32131.

[22] Humphrey, W., A. Dalke, and K. Schulten. 1996. VMD: visual molecular dynamics. J. Mol. Graph. Model. 14:33-38.

[23] Kortvelyesi, T., R. F. Murphy, and S. Lovas. 1999. Secondary structures and intramolecular interactions in fragments of the B-loops of naturally occurring analogs of epidermal growth factor. J. Biomol. Struct. Dyn. 17:393-407.

[24] Toth, G., C. R. Watts, R. F. Murphy, and S. Lovas. 2001. Significance of aromatic-backbone amide interactions in protein structure. Proteins. 43:373-381.

[25] Parrinello, M., and A. Rahman. 1981. Polymorphic transitions in single crystals: A new molecular dynamics method. J. Appl. Phys. 52:7182-7190.

[26] Nosé, S., and M. L. Klein. 1983. Constant pressure molecular dynamics for molecular systems. Molecular Physics. 50:1055-1076.

[27] Nose, S. 1984. A unified formulation of the constant temperature molecular dynamics methods. J. Chem. Phys. 81:511-519.

[28] Hoover, W. G. 1985. Canonical dynamics: Equilibrium phase-space distributions. Phys. Rev. A. 31:1695-1697.

[29] Patey, G. N., and J. P. Valleau. 1973. The free energy of spheres with dipoles: Monte Carlo with multistage sampling. Chem. Phys. Lett. 21:297-300.

[30] Torrie, G. M., and J. P. Valleau. 1974. Monte Carlo free energy estimates using non-Boltzmann sampling: Application to the sub-critical Lennard-Jones fluid. Chem. Phys. Lett. 28:578-581.

[31] Torrie, G. M., and J. P. Valleau. 1977. Nonphysical sampling distributions in Monte Carlo free-energy estimation: Umbrella sampling. J. Comput. Phys. 23:187-199.

[32] Kumar, S., J. M. Rosenberg, D. Bouzida, R. H. Swendsen, and P. A. Kollman. 1992. THE weighted histogram analysis method for free-energy calculations on biomolecules. I. The method. J. Comput. Chem. 13:1011-1021.

[33] Jarzynski, C. 1997. Nonequilibrium Equality for Free Energy Differences. Phys. Rev. Lett. 78:2690-2693.

[34] Hub, J. S., B. L. de Groot, and D. van der Spoel. 2010. g_wham—A Free Weighted Histogram Analysis Implementation Including Robust Error and Autocorrelation Estimates. J. Chem. Theory Comput. 6:3713-3720.

[35] Lyubchenko, Y. L., B. H. Kim, A. V. Krasnoslobodtsev, and J. Yu. 2010. Nanoimaging for protein misfolding diseases. Wiley Interdiscip. Rev. Nanomed. Nanobiotechnol. 2:526-543.

[36] Kim, B. H., N. Y. Palermo, S. Lovas, T. Zaikova, J. F. Keana, and Y. L. Lyubchenko. 2011. Single-molecule atomic force microscopy force spectroscopy study of Abeta-40 interactions. Biochemistry. 50:5154-5162.

[37] Klimov, D. K., and D. Thirumalai. 2003. Dissecting the Assembly of Aβ16–22 Amyloid Peptides into Antiparallel β Sheets. Structure. 11:295-307.

[38] Nguyen, P. H., M. S. Li, G. Stock, J. E. Straub, and D. Thirumalai. 2007. Monomer adds to preformed structured oligomers of Aβ-peptides by a two-stage dock–lock mechanism. Proc. Natl. Acad. Sci. USA. 104:111-116.

[39] Eker, F., K. Griebenow, and R. Schweitzer-Stenner. 2004. Aβ1-28 Fragment of the Amyloid Peptide Predominantly Adopts a Polyproline II Conformation in an Acidic Solution†. Biochemistry. 43:6893-6898.

[40] Gnanakaran, S., R. Nussinov, and A. E. García. 2006. Atomic-Level Description of Amyloid β-Dimer Formation. J. Am. Chem. Soc. 128:2158-2159.

[41] Rojas, A. V., A. Liwo, and H. A. Scheraga. 2011. A Study of the α-Helical Intermediate Preceding the Aggregation of the Amino-Terminal Fragment of the β Amyloid Peptide (Aβ1–28). J. Phys. Chem. B.12978-12983.

[42] Tjernberg, L. O., D. J. Callaway, A. Tjernberg, S. Hahne, C. Lilliehöök, L. Terenius, J. Thyberg, and C. Nordstedt. 1999. A molecular model of Alzheimer amyloid beta-peptide fibril formation. J. Biol. Chem. 274:12619-12625.

[43] Nguyen, P. H., M. S. Li, and P. Derreumaux. 2011. Effects of all-atom force fields on amyloid oligomerization: replica exchange molecular dynamics simulations of the Aβ16–22 dimer and trimer. Phys. Chem. Chem. Phys. 13:9778-9788.

[44] Xu, W., C. Zhang, P. Derreumaux, A. Gräslund, L. Morozova-Roche, and Y. Mu. 2011. Intrinsic Determinants of Aβ 12–24 pH-Dependent Self-Assembly Revealed by Combined Computational and Experimental Studies. PLoS One. 6:e24329.

[45] Palermo, N. Y., J. Csontos, M. C. Owen, R. F. Murphy, and S. Lovas. 2007. Aromatic-backbone interactions in model α-helical peptides. J. Comput. Chem. 28:1208-1214.

[46] Csontos, J., N. Y. Palermo, R. F. Murphy, and S. Lovas. 2008. Calculation of weakly polar interaction energies in polypeptides using density functional and local Møller-Plesset perturbation theory. J. Comput. Chem. 29:1344-1352.

[47] Hatfield, M. P. D., N. Y. Palermo, J. Csontos, R. F. Murphy, and S. Lovas. 2008. Quantum Chemical Quantification of Weakly Polar Interaction Energies in the TC5b Miniprotein. J. Phys. Chem. B. 112:3503-3508.

[48] Palermo, N. Y., J. Csontos, R. F. Murphy, and S. Lovas. 2008. Role of aromatic residues in stabilizing the secondary and tertiary structure of avian pancreatic polypeptide. Int. J. Quantum Chem. 108:814-819.

[49] Hatfield, M. P. D., R. F. Murphy, and S. n. Lovas. 2011. The CLN025 Decapeptide Retains a β-Hairpin Conformation in Urea and Guanidinium Chloride. J. Phys. Chem. B. 115:4971-4981.

[50] Mothana, B. R., S.; Rauk, . 2009. A.Molecular Dynamics Study of the Interaction of Aβ (13–23) with β-sheet Inhibitors. ARKIVOC. 2009:116– 134.

[51] Lemkul, J. A., and D. R. Bevan. 2010. Assessing the Stability of Alzheimer's Amyloid Protofibrils Using Molecular Dynamics. J. Phys. Chem. B. 114:1652-1660.

[52] Bu, Z., Y. Shi, D. J. E. Callaway, and R. Tycko. 2007. Molecular Alignment within β-Sheets in Aβ14-23 Fibrils: Solid-State NMR Experiments and Theoretical Predictions. Biophys. J. 92:594-602.

[53] Bernstein, S. L., N. F. Dupuis, N. D. Lazo, T. Wyttenbach, M. M. Condron, G. Bitan, D. B. Teplow, J.-E. Shea, B. T. Ruotolo, C. V. Robinson, and M. T. Bowers. 2009. Amyloid-β protein oligomerization and the importance of tetramers and dodecamers in the aetiology of Alzheimer's disease. Nat. Chem. 1:326-331.

[54] He, X., J. T. Giurleo, and D. S. Talaga. 2010. Role of Small Oligomers on the Amyloidogenic Aggregation Free-Energy Landscape. J. Mol. Biol. 395:134-154.

[55] Straub, J. E., and D. Thirumalai. 2010. Principles governing oligomer formation in amyloidogenic peptides. Curr. Opin. Struc. Biol. 20:187-195.

[56] Takeda, T., and D. K. Klimov. 2009. Interpeptide interactions induce helix to strand structural transition in Aβ peptides. Proteins: Structure, Function, and Bioinformatics. 77:1-13.

[57] Rojas, A., A. Liwo, D. Browne, and H. A. Scheraga. 2010. Mechanism of Fiber Assembly: Treatment of Aβ Peptide Aggregation with a Coarse-Grained United-Residue Force Field. J. Mol. Biol. 404:537-552.

[58] Lührs, T., C. Ritter, M. Adrian, D. Riek-Loher, B. Bohrmann, H. Döbeli, D. Schubert, and R. Riek. 2005. 3D structure of Alzheimer's amyloid-β(1–42) fibrils. Proc. Natl. Acad. Sci. USA. 102:17342-17347.

[59] Chebaro, Y., N. Mousseau, and P. Derreumaux. 2009. Structures and Thermodynamics of Alzheimer's Amyloid-β Aβ(16−35) Monomer and Dimer by Replica Exchange Molecular Dynamics Simulations: Implication for Full-Length Aβ Fibrillation. J. Phys. Chem. B. 113:7668-7675.

[60] Sarroukh, R., E. Cerf, S. Derclaye, Y. Dufrêne, E. Goormaghtigh, J.-M. Ruysschaert, and V. Raussens. 2011. Transformation of amyloid β(1–40) oligomers into fibrils is characterized by a major change in secondary structure. Cell Mol. Life Sci. 68:1429-1438.

[61] Mitternacht, S., I. Staneva, T. Hard, and A. Irback. 2011. Monte Carlo study of the formation and conformational properties of dimers of Abeta42 variants. J. Mol. Biol. 410:357-367.

[62] Baftizadeh, F., X. Biarnes, F. Pietrucci, F. Affinito, and A. Laio. 2012. Multidimensional View of Amyloid Fibril Nucleation in Atomistic Detail. J. Am. Chem. Soc. 134:3886-3894.

[63] Côté, S., R. Laghaei, P. Derreumaux, and N. Mousseau. 2012. Distinct Dimerization for Various Alloforms of the Amyloid-Beta Protein: Aβ1–40, Aβ1–42, and Aβ1–40(D23N). J. Phys. Chem. B. 116:4043-4055.

APPENDIX 2.1. The R script example Ramachandran plot

```
#The original code is from
http://www2.warwick.ac.uk/fac/sci/moac/students/peter_cock/r/density/#sm.density
#It can convert scatter points from Ramachandran calculation to contour plot
#Modified by Yuliang Zhang,
#Nov, 30, 2011, UNMC
#===============
#GEENRIC DATA
#===============
test.data = read.table("test.agr", header=FALSE, comment.char = "@",sep = "")#input
raw data to data
test.data[1:38,]#check whether rama data is correct
summary(test.data)

library(MASS)
generic.density <- kde2d(test.data[,1], test.data[,2], n=361, lims=c(-180,180,-180,180),
h=c(25,25))#function from MASS package
summary(generic.density)
sum(generic.density$z)
max <- max(generic.density$z)#check max value
min <- min(generic.density$z)#check min value
generic.total <- sum(generic.density$z)
#Lovel et al. divided their plots into three regions using 99.8% (allowed) and 98%
(favoured) levels (for the glycine, proline and pre-proline plots) or 99.95% (allowed) and
98% (favored) levels for the generic case.------Lovell, S.C. et al. Proteins: Structure,
Function, and Bioinformatics 50, 437-450 (2003).
100*sum(generic.density$z[generic.density$z > 0.0000001942]) / generic.total#to define
the edge where data is from 99.95% of total data.
100*sum(generic.density$z[generic.density$z > 0.000011326]) / generic.total#to define
the edge where data is from 98% of total data.
#100*sum(generic.density$z[generic.density$z > 0.00001788]) / generic.total
postscript("test.eps", horizontal=FALSE, onefile=FALSE, paper = "special", height=3,
width=3.3, pointsize=8)
#================
#For plot image with color bar
layout(matrix(data=c(1,2), nrow=1, ncol=2), widths=c(4,1),heights=c(1,1))
ColorRamp <- gray((30:0)/30)
ColorLevels <- seq(min, max, length=length(ColorRamp))
par(mar = c(6,5,2,2))
#================
#par(mar = c(5, 5, 1, 1)+.1)
x<-generic.density$x
y<-generic.density$y
image(x,y,z=generic.density$z,xlab="",ylab="",col=gray((30:0)/30),axes=FALSE)
```

```
contour(generic.density,asp=1,lwd=2,levels=c(0,0.0000001942,0.000011326),col=c('#FF
FFFF','#999999','#000000'),drawlabels=FALSE,axes=FALSE,add=TRUE)
#,col=c('#FFFFFF','#999999','#666666','#333333','#000000'))
#major tick
axis(1, at = seq(-180, 180, by = 60),font=2,lwd=2,cex.axis=1.5,labels=FALSE)
axis(2, at = seq(-180, 180, by = 60),font=2,lwd=2,cex.axis=1.5,las = 1)
lablist.x<-as.vector(c(-180,-120,-60,0,60,120,180))
text(x = seq(-180, 180, by=60), par("usr")[2] - 370, labels = lablist.x, srt = 0, pos = 1, xpd
= TRUE,font=2,cex=1.5)
#minor tick
axis(1, at = seq(-180, 180, by = 30),font=2,labels=FALSE,lwd=2,tck=-.02)
axis(2, at = seq(-180, 180, by = 30),font=2,labels=FALSE,lwd=2,tck=-.02)
box(lwd=2)
title(xlab=expression(paste(phi, " / Degrees")),ylab=expression(paste(psi, " /
Degrees")),font=2,cex.lab=2,mgp=c(3.35,1,0))
#abline(h=0,v=0,font=2,lwd=2,col="gray")

#=========
#Plot color bar
par(mar = c(6,0,2,4),font = 2)
image(1, ColorLevels, matrix(data=ColorLevels,
ncol=length(ColorLevels),nrow=1),col=ColorRamp,xlab="",ylab="",xaxt="n", las =
1,axes=FALSE,labels=FALSE)
axis(4, at = seq(min, max, by = max/5),font=2,lwd=2,cex.axis=1,las = 1)
box(lwd=2)
#==========
dev.off()
gc()
```

APPENDIX 2.2. The R script example for RMSIP calculation

```
#This script is used to calculate RMSIP from the first 10 eigenvectors.
#Jan, 14, 2012, Yuliang Zhang in UNMC, OMAHA.
#At first, we must comment the lines at the end of each *.g96 file using @ character.

#RMSIP of SimI and SimII(0-50NS)
#================================================
a <- paste("a_0-50_eigenvec", 2:11,".g96", sep="")#Generate the dataset including filename from simulation I
b <- paste("b_0-50_eigenvec", 2:11,".g96", sep="")#Generate the dataset including filename from simulation II
ab=c()# Creat matrix for cumulation of the sum of xyz data from 1 to 10 eigenvector.
for (i in 1:10){
  AA <- scan(a[i],skip=4,nlines=35)# Load raw data from simulation I, skip 4 character lines and read 35 lines data as a vector.
  dim(AA)=c(3,35)#Change dimention of vector to(3,35)
  A1 <- t(AA)#Build matrix like raw data with (35,3) dimention
  for (j in 1:10){
    BB <- scan(b[j],skip=4,nlines=35)#Load raw data from simulation II, skip 4 character lines and read 35 lines data as a vector.
    dim(BB)=c(3,35)#Change dimention of vector to(3,35)
    B1 <- t(BB)#Build matrix like raw data with (35,3) dimention
    sumxyz <- sum(A1[,1]*B1[,1])+sum(A1[,2]*B1[,2])+sum(A1[,3]*B1[,3])#The inner product of each dataset. We can use crossprod(A1,B1) to calculate them.
    ab <- c(ab,sumxyz)#Append data to variable ab
  }
}
"I-II(0-50NS)"
sqrt(crossprod(ab,ab)/10)#The RMSIP of first 10 eigenvectors
rm(a)
rm(b)
rm(A)
rm(B)
rm(sumxyz)
```

Chapter 3

VALIDATING THE STRUCTURE OF THE AMYLOIDOGENIC PROTEIN DIMERS WITH MONTE CARLO PULLING SIMULATION

3.1. INTRODUCTION

In the previous chapter, we provided detailed structural information as well as the interactions of short Aβ sequence (Aβ(14-23)) via the combination of AFM based single molecular force spectroscopy and steered Molecular Dynamics (SMD) simulations [1]. However, a major problem with this approach is that SMD is typically performed at pulling rates of 5 nm/ns, which are 10^7 times higher than those used under typical experimental conditions [1, 2]. This makes performing a direct comparison between *in silico* data and the experimental results difficult [3]. In a recent publication, high-speed AFM instrumentation was used in experimental conditions approaching the SMD temporal range [4], however this methodology is not well developed at this time. In a different approach, all-atom Monte Carlo Pulling (MCP) was described which enabled slowing down the pulling rates during simulations to rates comparable with regular AFM pulling experiments (pulling rate ~300 nm/s) [5]. The authors were able to directly compare their results with AFM experiments for amyloid β and α-synuclein monomers.

In this chapter, we further develop the MCP approach, thereby enabling us to model AFM pulling experiments that measured intrapeptide and interpeptide interactions. The titin 91 (formerly, I27) and ubiquitin proteins were chosen to verify the feasibility of

our novel approach. For the amyloid system, two peptides Sup35(6-13) ([Q6C]Sup35(6-13) containing sequence, CGNNQQNY) and Aβ(13-23) ([H13C]Aβ(13-23) containing sequence, CHQKLVFFAED) were selected and termed as Aβ peptide and Sup35 peptide, respectively. MCP analysis of AFM probing experiments for these peptides demonstrates that both peptides in the AFM experiments form transient misfolded dimers with an antiparallel orientation of the monomers' β-sheet. The monomers are arranged in an out-of-register pattern with an overall length of interacting segments of five residues. The MCP approach also enabled us to follow the rupture process and to characterize the contribution of different interactions to dimer stability.

3.2. METHODS

3.2.1. Initial Structure

The structure of I27 (PDB ID: 1TIT) and ubiquitin (PDB ID: 1UBQ) were taken from the Protein Data Bank (PDB) [6], and the PROFASI (Protein Folding and Aggregation Simulator) [7] software package was used to find the lowest energy structures through energy minimization. The structure for the in-register Aβ dimer was also generated using the same method.

Two short peptides, Aβ peptide and Sup35 peptide, as defined above, were studied. The structure of the Aβ dimer was taken from our previous publication [1], described in Chapter 2 and shown in Figure 3.1A. The Aβ dimer with an in-register β sheet in Figure 3.1B was generated by the PROFASI package [7]. Briefly, two monomer sequences were given to PROFASI to generate a random dimer conformation and then underwent 10^7 MC steps to obtain the low energy dimer structure with in-register

antiparallel β-sheet. The structures of the Sup35 dimers (both the out-of-register β sheet and the in-register β sheet) were obtained from Replica Exchange MD (REMD) simulations and are shown in Figure 3.1C, D. The REMD simulations were performed using the GROMACS 4.5.5 package [8], with modifications used in previous methods [1], and with the AMBER-ff99SB-ILDN force field [9]. The detailed simulation procedure is as follows:

The following parameters were used in the simulations: the integration time was 2 fs; the non-bonded interaction list was updated after every 10 steps; the LINCS [10] algorithm was used for all bonds to correct the length; the peptide and solvent, including ions, were coupled separately to a temperature bath with a 0.1 ps relaxation constant; constant pressure was achieved using Berendsen scaling [11] with a 1.0 ps relaxation constant and a 4.5×10^{-5} bar^{-1} isothermal compressibility; van der Waals interactions were switched off between 0.7 and 0.9 nm; Particle Mesh Ewald (PME), with a 1.0 nm cutoff, was used to deal with Coulomb interactions.

The two Sup35 monomers with random coil conformations were solvated in a dodecahedron box with 2398 TIP3P water molecules. The distance between the peptides and edges of the box was 1 nm. The distance between the center of mass (COM) of two monomers was 1.5 nm. Seven Na^+ and seven Cl^- were added to neutralize the charges, and the final salt concentration was adjusted to 150 mM NaCl. The systems were submitted to 1000 steps steepest descent energy minimization, and then to constant number of molecules, and volume and temperature (NVT) simulation, while the positions of the peptides were constrained to the center of the box with a force constant of 1000 kJ mol^{-1}. Then, 25 replicas (non-interacting copies) were submitted to Replica Exchange

Molecular Dynamics (REMD) simulation in parallel at temperatures ranging from 300K to 400 K. The following set of temperatures, generated through http://folding.bmc.uu.se/remd/, were used: 300.00, 303.58, 307.20, 310.85, 314.53, 318.26, 322.01, 325.80, 329.63, 333.50, 337.40, 341.34, 345.32, 349.34, 353.40, 357.49, 361.63, 365.81, 370.02, 374.28, 378.57, 382.92, 387.30, 391.72, 396.19. After a certain time, the neighboring replicas were selected randomly and exchanged with the probability of approximately 0.2, based on the Metropolis criterion:

$$P(i \rightarrow j) = \min\{1, \exp[(\beta_j - \beta_i)(E_j - E_i)]\} \quad (1)$$

where E_i and E_j are the potential energy of the i^{th} and j^{th} replicas, $\beta_i=1/k_BT_i$, $\beta_j=1/k_BT_j$, k_B is the Boltzmann constant, and T is the absolute temperature. After a 140 ns simulation, the last 100 ns trajectory at the 300 K was used for analysis. To avoid artifacts from combining internal and overall motion and to acquire a meaningful free energy landscape, Principal Component analysis of backbone dihedrals (dPCA) was used to generate the representative structures [12]. The following equation was used for the free energy calculations:

$$\Delta G(V1, V2) = -k_B T[\mathrm{Ln}\, P(V1, V2) - P_{max})] \quad (2)$$

where V1 and V2 are the first and second largest Principal Components; P(V1,V2) indicates the distribution obtained from the histogram of REMD data, P_{max} is the maximum of distribution, which is subtracted to make sure the $\Delta G=0$ for the lowest free energy minimum. k_B is the Boltzmann constant, and T is the absolute temperature. The Fortran program for the dPCA analysis was provided by Dr. Yuguang Mu. The representative structures associated with two energy minima on the free energy landscape were identified, one was an out-of-register antiparallel β-sheet dimer and the second was

an in-register antiparallel β-sheet dimer (Figure 3.2). These two structures were chosen as representative structures for the MCP simulations.

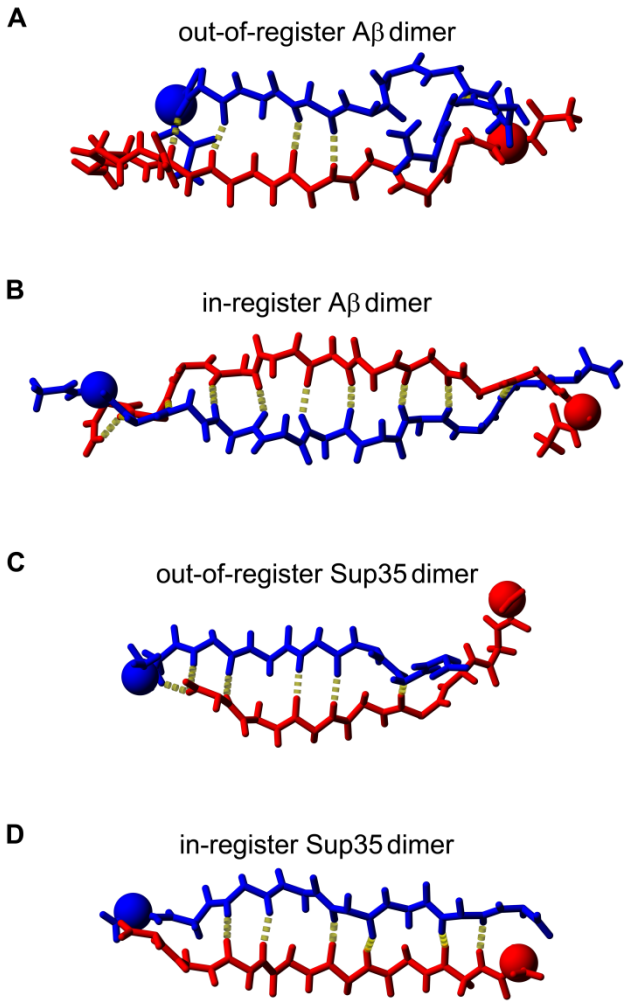

Figure 3.1. The initial structures for MC pulling (MCP) simulations. (A) The out-of-register Aβ dimer structure obtained in our previous study [1], with an antiparallel orientation of the monomers, was chosen for the MCP simulation. (B) The in-register Aβ dimer generated in this work by using PROFASI software. The antiparallel out-of-register (C) and in-register (D) Sup 35 dimers correspond to structures with the lowest energy minima in the REMD simulations. The stick structures correspond to the backbones of the two monomers, and the dot lines represent hydrogen bonds. The balls indicate the Cα atoms for the N terminal residues of the monomers, where the pulling force was applied.

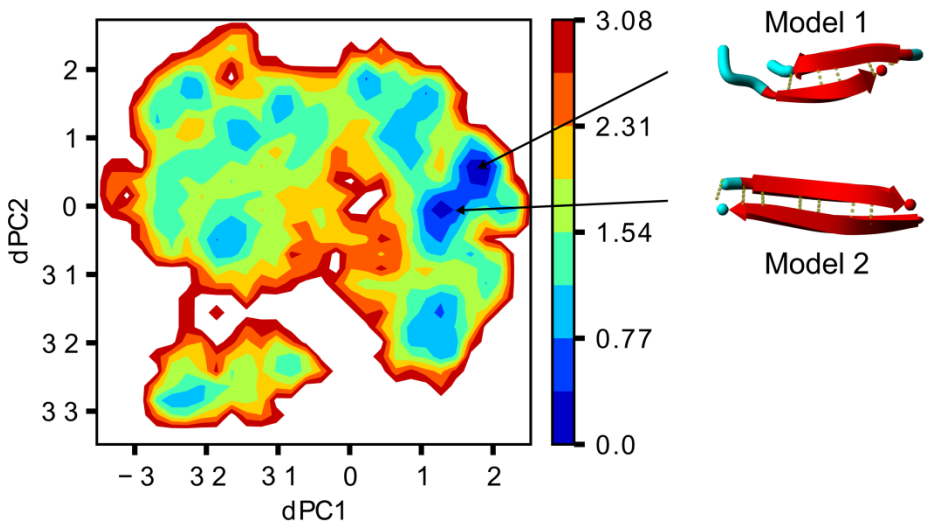

Figure 3.2. The energy landscape profiles for the Sup35 dimers obtained with the Replica Exchange Molecular Dynamics (REMD) simulations. The snapshots of the two major minima are indicated to the right of the energy landscape profile. The red arrows in the models indicate β-strands, cyan tubes are the random coils, and dot lines are hydrogen bonds.

3.2.2. Monte Carlo Pulling (MCP) simulation

The modified MCP simulations were implemented using the PROFASI package [7] with the implicit water model and the all-atom FF08 force field [5, 7]. In the PROFASI software package, bond lengths, bond angles, and peptide torsion angles are assumed to be fixed. The interaction potential consists of the following four terms:

$$E = E_{loc} + E_{ev} + E_{hb} + E_{hp} \quad (3)$$

The E_{loc} term is the backbone potential from the adjacent peptide units along the chain; E_{ev} represents a $1/r^{12}$ repulsion between a pair of atoms; E_{hb} and E_{hp} indicate the hydrogen binding energy and hydrophobic energy, respectively.

Recently, the atomic level MCP simulation with respect to a constant pulling rate was proposed [5]. A virtual spring is attached to the two Cα of the N and C terminal residues, and the spring pulls the two atoms along a vector between them during the pulling simulation. The energy change of the spring is provided by the E2Espring function (the virtual spring attached on the two Cα of the N and C terminal residues) in the PROFASI package and calculated using the following equation:

$$E_{tot} = E(x) + \frac{k}{2}[L_0 + vt - L(x)]^2 \quad (4)$$

where E(x) is the energy in the absence of an external force, t is MC step time, and k is the spring constant of the probe. L_0 represents the distance between the Cα atoms of Cys at the N termini from the initial conformation. L(x) is the distance between Cα atoms of Cys during MC pulling, and x denotes a protein conformation. When v = 0.1 fm per MC step, the value is equivalent to 600 nm/s.

However, the E2Espring function parameter only calculates the distance along a vector of the N and C terminal residues, which is not suitable for the simulation of intermolecular interactions of AFM probing experiments [1]. Therefore, we modified the E2Espring to the A2Aspring function (the virtual spring is attached onto the two Cα of any pairwise residues from different chains, appendix 3.1) by introducing two parameters into the program, Pulling Group 1 and Pulling Group 2, to recognize the specific atoms. In this Chapter, we used the Cα atoms of the cysteines at the N termini as Pulling Group 1 and Pulling Group 2, respectively. The distance between two Cα atoms of any pairwise residues from different chains was calculated by the Atomdistance function in PROFASI instead of the end-to-end distance between two Cα atoms of the N and C terminal residues. The temperatures used for the amyloidogenic protein simulation were 300 K, 288 K, and 266 K. The parameters for each case are listed in Table 3.1.

Table 3.1. The dimers rupture characteristics obtained from the MCP simulations performed at different temperatures.

Protein	Temp. (Kelvin)	Spring constant (pN/nm)	v (nm/s)	No. of rupture events	No. of simulations
1TIT	300	100	1000 600	162 140	200 200
1UBQ	300	40	300	199	200
Aβ[a]	300 288 266	30	500	586 256 315	1000 400 400
Aβ[b]	300 288 266	30	500	397 393 196	400 400 200
Sup35[a]	300[c] 288 266	40 & 60 40 40	300	318 196 372	1400 400 400
Sup35[b]	300[c] 288 266	40 & 60 40 40	300	991 344 397	1400 400 400

v - pulling rate converted from fm per MC step

1TIT - titin

1UBQ - ubiquitin

[a]Simulations from the out-of-register structure of Aβ and Sup35 peptides.

[b]Simulations from the in-register structure of Aβ and Sup35 peptides.

[c]Combined data obtained with two spring constant values (40 and 60 pN/nm) as used in experiments.

3.2.3. Data analysis

Several hundred simulations were performed and the rupture events were assembled in Table 3.1. The force curves were smoothed by Matlab 2013a via smooth function (MathWorks Inc., Natick, MA, USA). The rupture peak was defined by the force value > 20 pN, and the position of the peak was identified by the minimum derivative value of the smoothed force curve. Rupture force distributions for each structure were compared to experimental values and were fitted by probability density function (PDF) [13, 14]. The equation of PDF is as follows:

$$p(F) = \frac{k_{off}}{v_F} exp\left(\frac{F}{F^{\ddagger}} - \frac{k_{off}F^{\ddagger}}{v_F}\left(e^{F/F^{\ddagger}} - 1\right)\right) \qquad (5)$$

where, k_{off} is the dissociation rate of protein complex at zero force. v_F is the loading rate. F represents rupture force. $F^{\ddagger} = k_BT/x^{\ddagger}$. k_B is the Boltzmann constant. T is the absolute temperature. $x^{\ddagger}$ is the distance of equilibrate state to transition state.

The majority of simulations were fitted by bimodal PDF indicating the existence of transient states in the dimers, but the results from the in-register dimers at low temperatures were fitted by monomodal PDF. The Kolmogorov-Smirnov nonparametric test (SPSS 20.0; IBM Corp, Armonk, NY, USA) was used to determine statistical significance between the force distribution differences. The fractions of dissociated dimers for both peptides, for in-register and out-of-register conformations, were obtained by dividing the number of simulations with non-rupture events by the total number of simulations. All of the line plots were produced by Igor Pro. 6.3.4 (WaveMetrics, Lake Oswego, OR, USA); the snapshots were generated by YASARA (www.yasara.org).

3.3. RESULTS

3.3.1. Monte Carlo Pulling (MCP) approach

The all-atom MCP method was described in [5] to unravel the intramolecular structure of proteins by pulling apart the N and C terminal residues. We modified this approach for AFM probing experiments in which the dimer, formed by two monomers immobilized to the AFM tip and the substrate, is pulled apart. With these modifications we are able to apply pulling forces to any pair of Cα atoms. The approach was validated using experimental data for the commonly used systems – titin I91 (formerly, I27) and ubiquitin proteins. Under an applied force each repeated unit of the I91 protein unravels in a step-wise pattern. In the experiment, using a pulling rate of 600 nm/s [15, 16], each segment of I91 protein ruptures cooperatively, producing a rupture force value of 200 ± 26 pN. Similar experimental studies for ubiquitin performed in [17] resulted in a rupture force value of 203 ± 35 pN.

We used our MCP approach to model the pulling process of one unit of I91 using the available PDB structure (PDB ID: 1TIT [18]). A typical force curve for the rupture of this I91 unit is shown in Figure 3.3A. The mean rupture force values are 184 ± 37 pN (n = 140) at a pulling rate of 600 nm/s, and 203 ± 33 pN (n = 162) at a pulling rate of 1 μm/s. The experimental value 200 ± 26 pN obtained at a pulling rate of 600 nm/s [15, 16] is very close to both theoretical values. Recent *in silico* results obtained with the coarse-grained model at a pulling rate of 600 nm/s produced the rupture force value 204 ± 30 pN [19], which is matches closely with our retults. Similarly, we modeled ubiquitin rupture by using the PDB structure (PDB ID: 1UBQ [20]). The results obtained at the pulling rate of 400 nm/s are shown in Figure 3.3B. The maximum rupture force 208 ± 51 pN (n =

199) is very close to the experimental value, 203 ± 35 pN, in ref. [15] and the in silico value, 230 ± 34 pN, obtained in [17]. Therefore, our MCP approach produces rupture force results that are in agreement with experimental data.

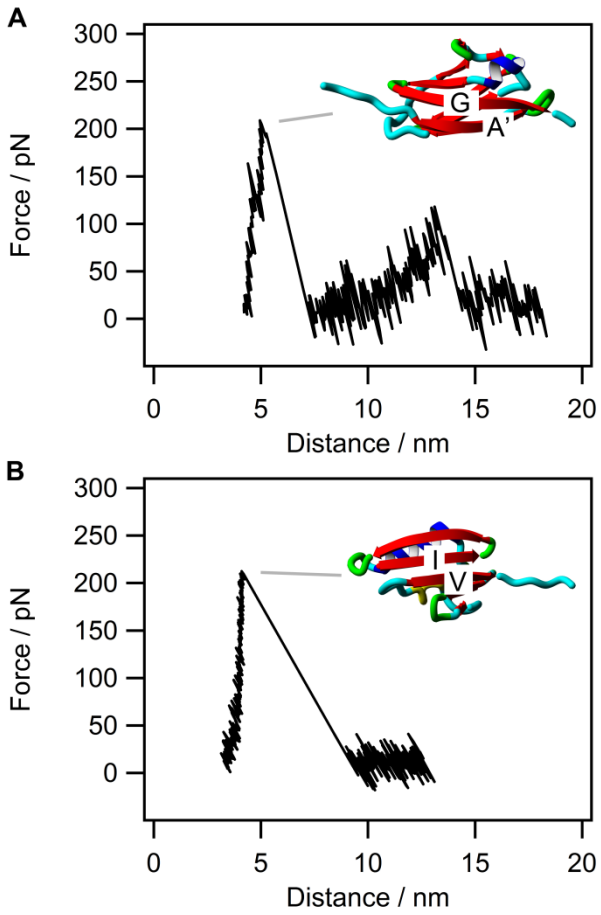

Figure 3.3. Typical force curves for unraveling I91 domains and ubiquitin. (A) The initial structure of I91 is taken from the PDB website (PDB ID: 1TIT). The snapshot just before rupture is on the right. The rupture force is 200 pN followed by the breakage of the β-strands of A'-G, as shown on the right. (B) The unfolding of ubiquitin (PDB ID: 1UBQ). The snapshot before the maximum rupture is seen on the right. The rupture event occurs at the breakage of the β-strands I and V, as shown on the right side of the force curve. In the schematics of the structures, the arrows indicate β-strands, the tubes are random coils of different types, and the ribbon represents α-helix.

3.3.2. Structural features of Aβ and Sup35 peptides

We used our MCP approach to analyze the dimers formed by two amyloidogenic peptides, Aβ and Sup35. Both peptides were probed in SMFS experiments during which each monomer was tethered to the AFM tip and substrate surface via terminal Cys residues. The dimers' dissociation was characterized by sharp rupture events with forces in the range of 100 pN [1, 21]. Therefore, in order to closely mimic the AFM experimental conditions during the MCP simulations, Cys residues were added to the N termini of the peptides and the pulling force was applied at Cα atoms of these Cys residues.

In the computer simulations, four different conformers, shown in Figure 3.1, were chosen as the initial structures for the MCP analyses. For the Aβ dimer, the structure generated from our previous publication [1] was selected. For this structure, shown in Figure 3.1A, the two monomers adopt an out-of-register antiparallel β-sheet conformation stabilized by four backbone hydrogen bonds. H-bonds are formed between residues His14 of monomer A and Phe19 of monomer B, and between Lys16 of monomer A and Leu17 of monomer B. Salt bridges and aromatic interactions are also involved in stabilizing the Aβ dimer structure [1]. Another structure for the Aβ dimer was the in-register antiparallel β-sheet conformation (Figure 3.1B) generated using the PROFASI software (see methods section).

The selected structures of Sup35 peptide are shown in Figure 3.1C and D. These two dimer structures were found by the REMD simulation (see methods section). The monomers in the dimer are oriented in an antiparallel fashion with out-of-register or in-register arrangements (Figure 3.1C, D, respectively). Five backbone hydrogen bonds

from the Asn and Gln residues participate in the formation of the out-of-register dimer in Figure 3.1C, while 7 backbone hydrogen bonds stabilize the in-register dimer structure (Figure 3.1D). Two Cα atoms from the Cys residues, indicated with the balls, were chosen as the pulling force application points.

3.3.3. MCP pulling of Aβ dimers

A representative MCP force curve obtained for the Aβ dimer in the out-of-register conformation is shown in Figure 3.4A. The structure of the dimer prior to the rupture is shown above the force curve. The simulations were carried out at the pulling rate of 500 nm/s, which is close to the experimental pulling rate. Figure 3.4A shows that the dimer undergoes a sharp transition with a rupture force value of 60 pN. Similar simulations were performed for 586 pulling events, and the distribution of the rupture forces is shown in Fig. 3 B. The force distribution is asymmetrical (skewed to the right) with the geometric mean value of 46 ± 1 pN ± the standard error of geometric mean, as described in [22]. Similar simulations for the in-register conformation of the Aβ dimer produced larger forces, as shown in Figure 3.4C. The histogram built for the set of 397 simulation runs is shown in Figure 3.4D. The distribution is broad with a geometric mean value of 178 ± 3 pN that is three fold of the value obtained for the out-of-register conformation. The experimental value of 53 ± 2 pN (Figure 3.4E) obtained at the same pulling rate [1] is considerably closer to the computational data for the out-of-register model (46 ± 1 pN). The difference between the experimental results and the simulated value for the out-of-register model is only ~10% which can be explained by a number of minor factors such as exact ionic conditions, and experimental errors in the force calibration. In our previous

analysis of the rupture of the out-of-register Aβ dimers with the use of the SMD approach, a rupter value more more than 10 times greater was obtained [1]; This was due to the use of a pulling rate of 5 nm/ns, which is 10^7 times greater than pulling rates used in MCP simulations and the experiment.

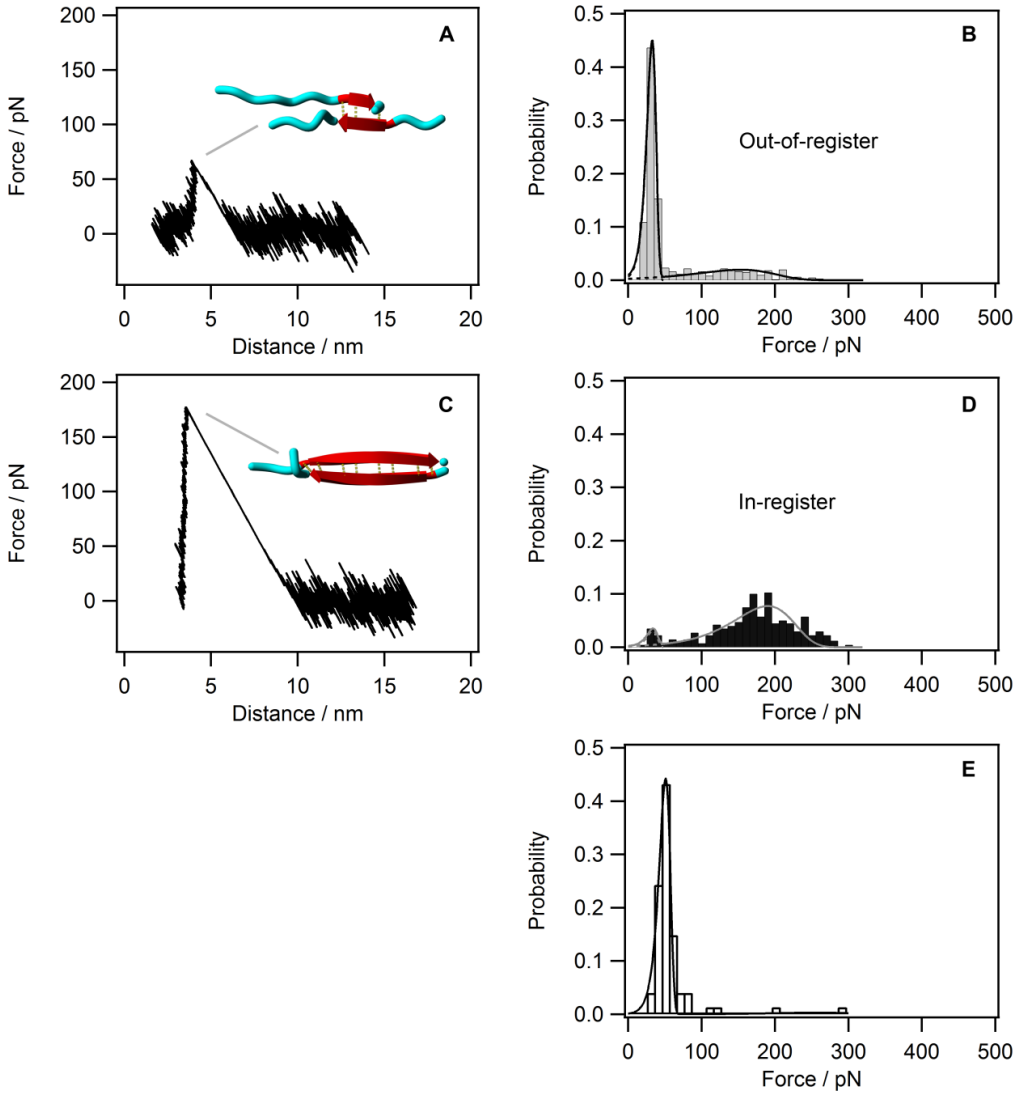

Figure 3.4. The rupture force curves and distributions of Aβ peptide at 300 K. (A) A typical force curve for the rupture of the out-of-register dimer. The snapshot of the dimer structure prior to the rupture is above the force curve. (B) The rupture force distribution for the force induced dissociation of the out-of-register dimer. (C) Typical force curve for the dissociation of the in-register dimer. The snapshot of the dimer structure before the rupture is above the force curve. In A and C, the distance on the x-axis of the force plots corresponds to the distances between the Cα atoms of the N-terminal Cys residues. The arrows indicate β-strands, the tubes are random coils, and the dotted lines are hydrogen bonds. (D) Rupture force distribution for the in-register dimer. The force distribution histograms are approximated with probability density functions (PDF). The bimodal approximation fits the histograms. Individual PDF distributions made with dotted lines essentially coincide with the overall distributions shown with solid lines. (E) The reconstructed rupture force distribution from experimental results for Aβ dimer. The solid (B and D) and dashed lines (B) indicate the individual fits with probability density function (PDF), which donate the overall fits in Fig 3.4. In E, the black solid line represents the unimodal fit with the PDF.

The MCP simulations revealed that three classes of out-of-register Aβ dimers exist, differing in their rupture processes (Figure 3.5). The parameters used for the characterization of different structures are rupture forces values, number of hydrogen bonds, and β-sheet content. Class I structures are defined as having a rupture force value > 20 pN, a number of hydrogen bonds ≥ 0, and a β-sheet content of 0. Class II structures have a rupture force value > 20 pN, hydrogen bond numbers ranging from 1 to 5, and a β-sheet content of > 0. Class III is similar to Class II, but contains a number of hydrogen bonds > 5. In class I dimers (Figure 3.5A), the β structure dissociates before approaching the maximum rupture force, leading to the formation of a non-β structure stabilized by aromatic-aromatic (Ar-Ar) interactions of four Phe residues as seen in Figure 3.5A. Its dissociation, averaged over 386 events, produces a mean rupture force of 32 ± 1 pN (Figure 3.4B, fist peak). Class I dimers are the most representative population of the rupture events in the MCP simulations. In Class II (Figure 3.5B), the out-of-register structure retains a few hydrogen bonds prior to reaching the maximum force, and Ar-Ar interactions contribute to the structural stability of the dimer. In class III dimers (Figure 3.5C), the out-of-register structure undergoes a conformational transition to structures containing relatively high β-sheet content from 70% residues, with some conformations forming in-register dimers. The conformational transitions occurred due to a relatively low pulling rate (500 nm/s) and the fast rate of β-sheet formation, which is in the microsecond time scale [23]. These conformational transitions of the structure with different β content can occur during the pulling of in-register dimers as well. This model explains the broad distribution for the in-register dimer pulling results (Figure 3.4D). Due to the fast rate of the conformational transitions, dimers with fewer numbers of hydrogen

bonds are formed and dissociations occur at low forces. The forces from Class II and III structures contribute to the asymmetry of the overall force distributions. Although there is a significant difference between the simulation of out-of-register dimers and experimental conditions ($p < 0.01$), class I and II rupture conformations correspond to the rupture force values that are close to experimental rupture force values (Figure 3.4E). This finding suggests that a combination of these two types of structures is probed with the experiment.

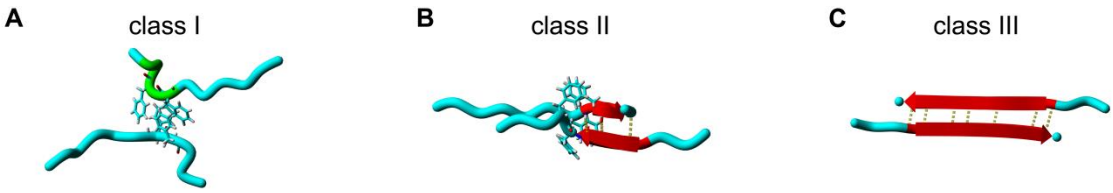

Figure 3.5. Modeling of the rupture process for three classes of structures for the out-of-register Aβ dimer. The simulation was performed at 300 K. (A) The Class I structure is characterized by the transient formation of dimers stabilized by aromatic-aromatic (Ar-Ar) interactions. (B) The Class II structure contains hydrogen bonding and Ar-Ar interactions. (C) The Class III structure is rearranged from the initial structure to form more hydrogen bonds. The arrows indicate β-strands, the tubes are random coils, the stick structures represent Phe residues and the dotted lines are hydrogen bonds.

3.3.4. MCP pulling of Sup35 dimers

Next, we used the MCP simulation method to characterize the rupture process of Sup35 dimers. Analysis of the REMD simulation data generated two structures (Figure 3.1C, D). The typical rupture profiles obtained using the MCP approach and experimental method are shown in Fig. 5. The distribution for the rupture forces for the out-of-register Sup35 dimer shown in the Figure 3.6A results in a rupture force of 33 ± 1 pN (n = 318). The rupture profile for the out-of-register Sup35 dimer data shows that there is tremendous fluctuation in the dimer structure (Figure 3.6A, inset). While five hydrogen bonds remain stable (Figure 3.7A), the two extra dangling hydrogen bonds between Tyr of one monomer and Gly of the other monomer are unstable prior to the rupture event. According to Figure 3.7B, which shows the residue position fluctuations, the terminal Cys residues are floppy and characterized by a relatively large Root Mean Square Fluctuation (RMSF) value (> 0.3 nm).

A similar analysis was performed for the in-register dimer (Figure 3.7C, D); a representative force curve is shown in Figure 3.6B inset. Based on 991 rupture events (the distribution is shown in Figure 3.6B), the rupture force was determined to be 58 ± 1 pN. The in-register dimer has 7 hydrogen bonds that remain intact until the end of the rupture process. Furthermore, unlike the out-of-register dimers, the number of hydrogen bonds in the in-register dimers remains constant before the rupture starts (Figure 3.7C), and there are no dangling hydrogen bonds. Additionally, the RMSF value of residues is relatively low (< 0.3 nm; Figure 3.7D), suggesting that the swing residues and the dangling hydrogen bonds in the out-of-register dimer are responsible for its reduced conformational stability. Similar to the results for the Aβ dimer structures, the out-of-

register dimer with low β-sheet content constitutes the most representative species, suggesting that these structures were probed in the majority of the force probing experiments.

The force distribution of experimental data assembled in Figure 3.6C has a peak value 42 ± 2 pN that is significantly less of the value 58 ± 1 pN for the simulation of the in-register dimer ($p < 0.01$), but closer to 33 ± 1 pN obtained for the simulation for the out-of-register dimer. The comparison between these values is summarized by the bar histogram in Figure 3.8. Next, we fitted the force distributions in Figure 3.6 with bimodal PDF functions. Such an approximation shows that the experimental data (main peak at 33 pN, shoulder peak at 55 pN) correlate well with the theoretical data for the out-of-register model (main peak at 32 pN and shoulder peak at 50 pN). At the same time, the in-register model has a minor first peak at 40 pN and the major second peak at 92 pN. These comparisons are summarized in Table 3.2, and Figure 3.8. This comparative analysis suggests that the out-of-register Sup35 dimer is the predominant structure probing by SMFS experiment.

The elevated dynamics observed for Sup35 dimers is in agreement with the computational analyses described in ref. [24], which analyzed the dynamics of the Sup35 crystallographic hexamer structure [25]. These simulations showed that the crystallographic hexamer is not stable and dissociates in the course of the simulation process, suggesting that additional interactions within a large ensemble of the peptide units are responsible for ensemble stabilization.

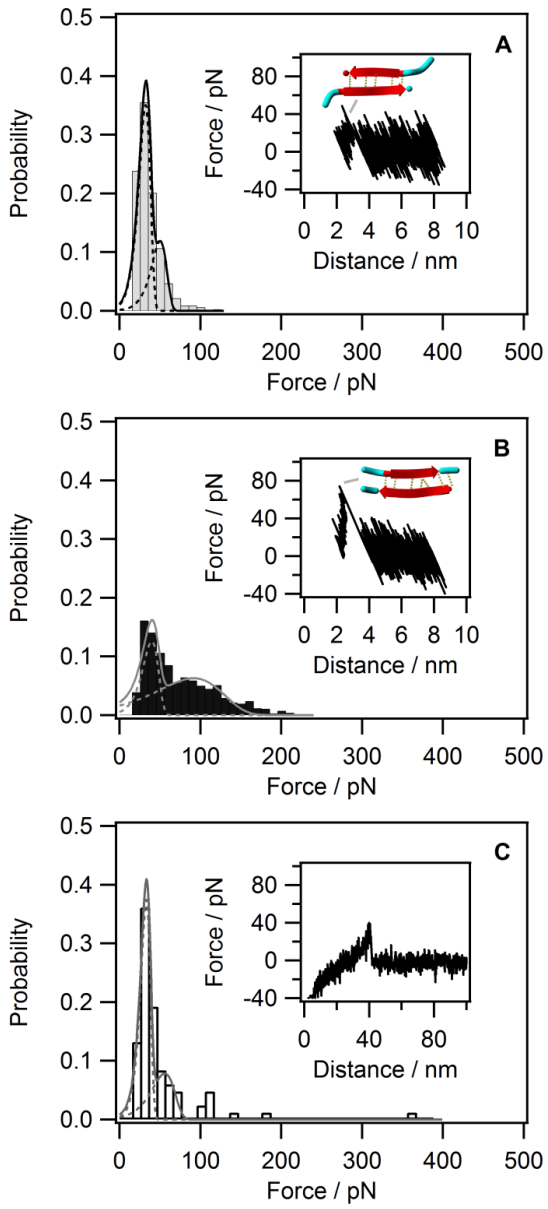

Figure 3.6. The rupture force distributions for Sup35 dimers at 300 K. (A) Theoretical data for the dissociation of the out-of-register dimer. (B) Theoretical data for the dissociation of the in-register dimer. (C) The experimental results for the rupture force distribution for Sup35 dimer at pulling rate of 300 nm/s. Note that the distance in the force curve show in C (inset) includes the length of stretching polymer tether used for the peptide immobilization [21]. The solid lines indicate the overall fits approximation with the bimodal PDF and the dotted lines represent individual PDF fits. The insets are the representative force curves. The models of structures are shown above the force curves in the insets. The red arrows indicate β-strands, the tubes are the random coils, and the dotted lines are hydrogen bonds. The distance in the graphs corresponds to the distances between the Cα atoms of the N-terminal Cys residues (black lines in the insets of A and C).

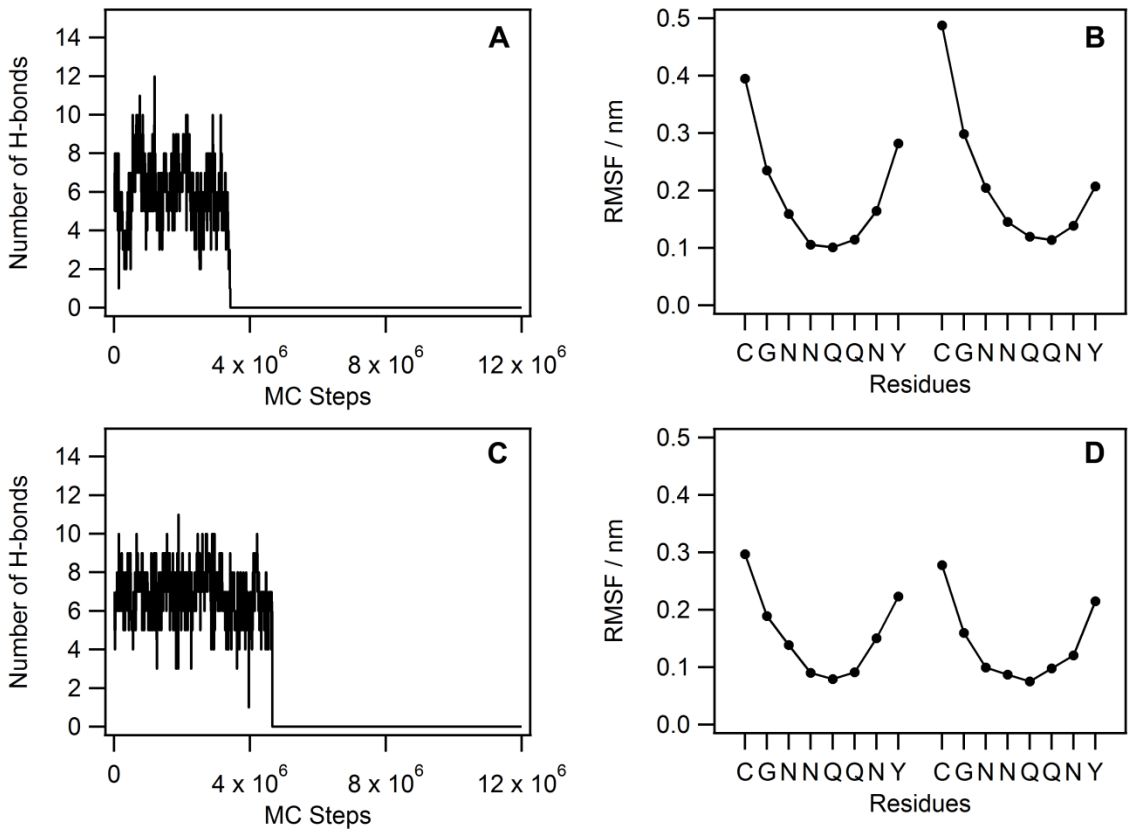

Figure 3.7. The results of the MCP simulation at 300 K for the pulling of Sup35 peptide with the out-of-register (A, B) and in-register (C, D) arrangements of the polypeptide chains. The number of hydrogen bonds within the main chain of the dimers during the pulling is calculated by using g_bonds from the Gromacs package (black lines in A and C). The graphs (B and D) are the root-mean-square fluctuation (RMSF) of the Cα atoms for each residue calculated by g_rmsf from the Gromacs package.

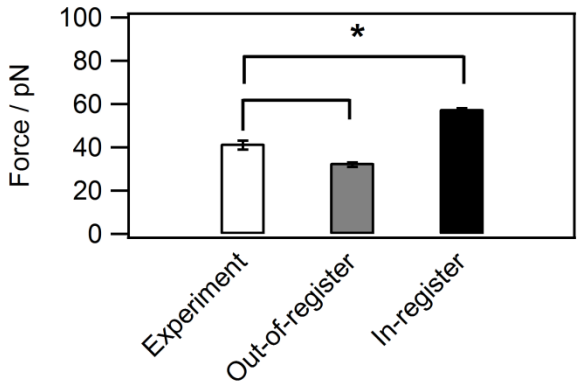

Figure 3.8. The statistical analysis of Sup35 dimer at 300 K. The difference of the pairwise datasets is estimated by the Kolmogorov-Smirnov test. A statistically significant difference corresponding to $p < 0.01$ is indicated with the asterisk. The data is shown as the geometric mean ± standard error of geometric mean. The white bar is the experimental data. The gray and black bars correspond to the simulations for the out-of-register and the in-register arrangements of the dimers, respectively.

Table 3.2. The peaks from PDF fit of the distributions for Sup 35 dimers.

	Main Peak (pN)	Shoulder peak (pN)	ΔF (pN)
Sup35[a]	32	50	18
Sup35[b]	40	92	52
Experiment	33	55	22

ΔF is the interval between main peak and shoulder peak.

[a]Simulations from the out-of-register structure.

[b]Simulations from the in-register structure.

3.3.5. Temperature dependence of stabilities of Sup35 and Aβ dimers

The increased mobility of the terminal residues identified in the comparative structural studies of the dimers under pulling stress indicates differences in the dimers' stabilities. In order to evaluate the thermodynamic stabilities of both types of Sup35 and Aβ dimers, we performed MCP simulations for the four structures at temperatures 288 K and 266 K. The force histograms for Aβ and Sup35 peptides are assembled in Figure 3.9 and Figure 3.10, respectively. There is a trend towards higher forces as the temperature decreases, suggesting that thermal fluctuations destabilize the dimers in the force probing. This assumption was confirmed by the analysis in which the fractions of dissociated dimers for both peptides, adopting in-register and out-of-register conformations, were determined from the ratio of the number of simulations with non-rupture events to the total number of simulations. The rupture events are shown in Table 3.1 and plotted in Fig. 11. They demonstrate that the dissociation fraction increases with temperature, but the association varies depending on the type of peptide and its conformation. The dependence on temperature is less steep for in-register conformations than for its out-of-register conformations, and the in-register Aβ dimer is not dependent on the temperatures used in this analysis (Figure 3.11A). This suggests that the in-register structure is stable with respect to the out-of-register structure. The temperature dependence for the out-of-register Sup35 peptide is the steepest (Figure 3.11B), suggesting that the dimer in this conformation is very dynamic.

The higher stability of the out-of-register Aβ dimer compared to the stability of the out-of-register Sup35 dimer can be explained by the elevated hydrophobicity of the Aβ peptide, in particular Class I, II, and the hydrophilic feature of the Sup35 peptide.

Additionally, Aβ contains three charged residues (Lys-16, Glu-22, and Asp-23) that interact within the dimer and contribute to dimer stability. The analysis performed in [1] identified the formation of salt bridges and aromatic interactions as additional stability factors for Aβ dimers.

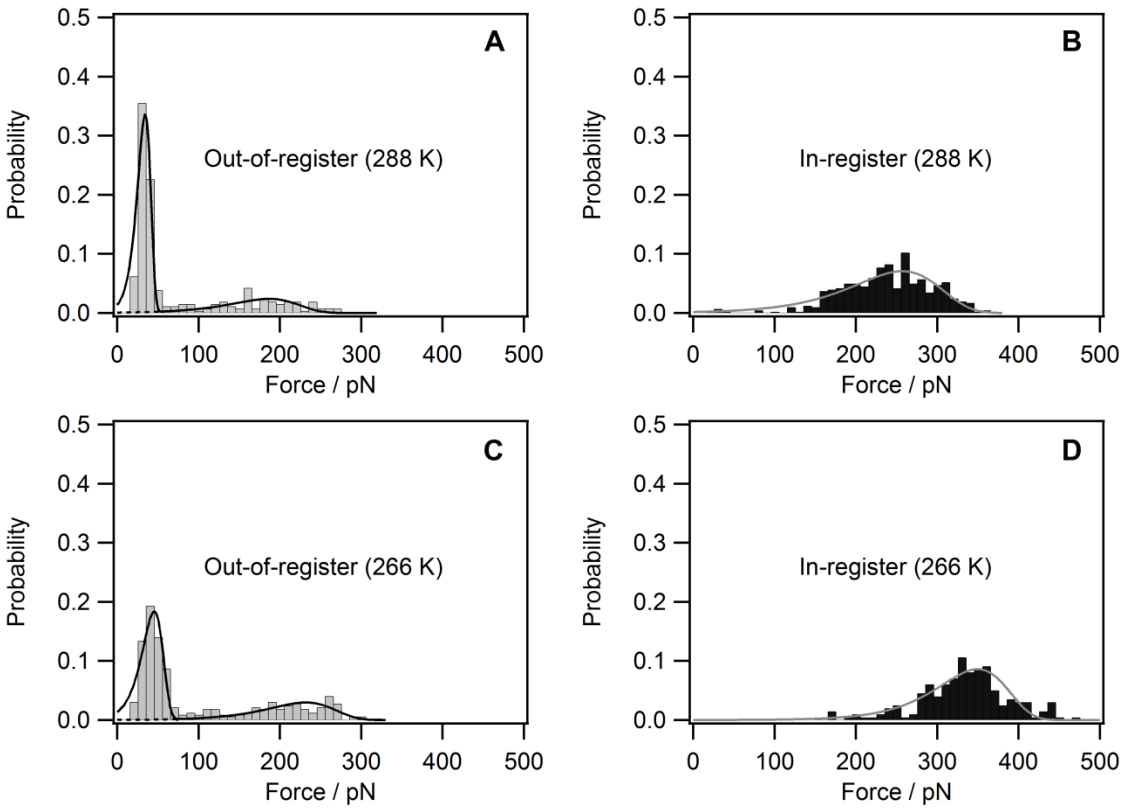

Figure 3.9. The rupture force distributions for Aβ peptide at temperatures of 288 K and 266 K. (A) and (B) are the force distributions at 288 K for out-of-register and in-register dimers arrangements, respectively. (C) and (D) are the force distributions at 266K for out-of-register and in-register dimers arrangements, respectively. The dashed lines represent the each unimodal PDF fit and solid lines indicate the overall fits.

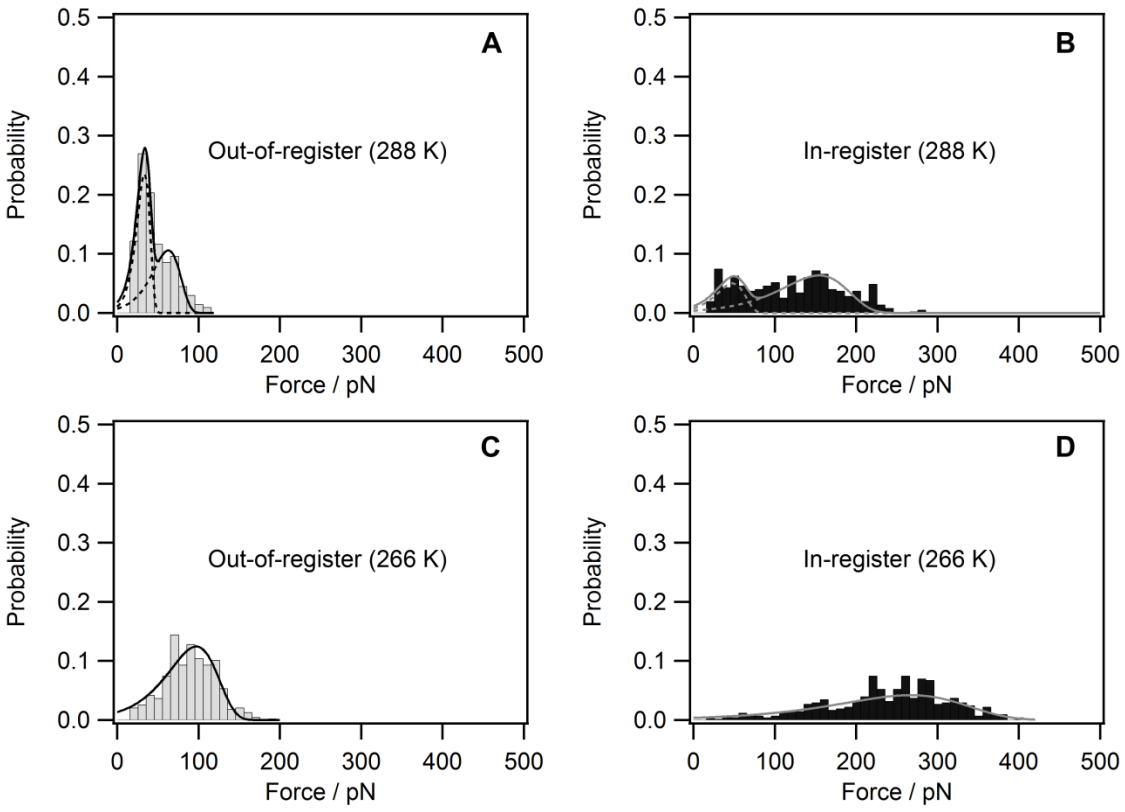

Figure 3.10. The rupture forces distributions for Sup35 peptide for temperatures of 288 K and 266 K. (A) and (B) are the force distributions at 288 K for out-of-register and in-register dimers arrangements, respectively. (C) and (D) are the force distributions at 266K for out-of-register and in-register dimers arrangements, respectively. The solid lines indicate the fits with bimodal PDF and the dashed lines represent the each unimodal PDF fit, which are overlaid by the solid lines.

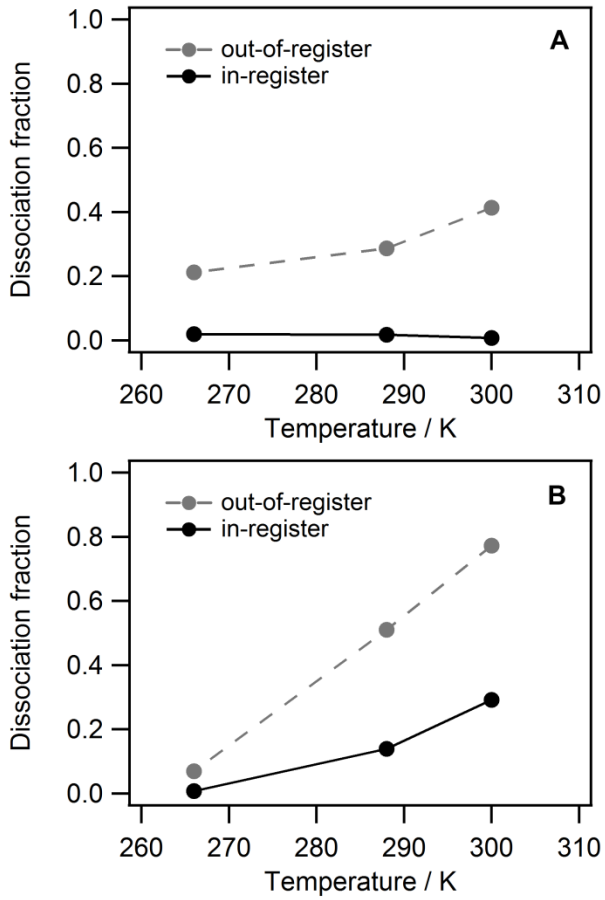

Figure 3.11. The temperature dependence of the fraction of dissociated dimers for the Aβ dimer (A) and the Sup35 dimer (B). The gray dashed lines represent the out-of-register dimers, and the black solid lines represent the in-register dimers.

3.3.6. Dynamics of Sup35 and Aβ dimers and the aggregation process

The MD and REMD simulations, respectively, for Aβ and Sup35 peptides showed that the dimers are capable of forming out-of-register and in-register arrangements. However, comparison with the experimental data led to the conclusion that both peptides in the AFM probing experiments assemble as dimers in an out-of-register alignment. Given the higher stability of the in-register dimer structure than the out-of-register structure, it would be expected that the formation with the most stable structure would occur in AFM probing experiments. The dimers could undergo the transition into the in-register conformation prior to their growth into larger oligomers. This is supported by the observation of rupture events with forces considerably exceeding that for the out-of-register conformation, although the yield of these events is very low, in the range of a percent [1, 21].

According to the contour plot from 2D projection of the free energy for Sup35 produced by the REMD simulation (Figure 3.2), there are two major local energy minima corresponding to the most stable configurations. Therefore, it is reasonable to assume that out-of-register structures are kinetically trapped, and the dimer can adopt the most stable conformation over time after passing a barrier between the two energy minima. We observed previously in the MD simulations of Aβ peptide, the formation of the in-register dimer configuration that began with the out-of-register conformation [1]. This transition required full dissociation of the dimer followed by the rearrangement of the peptide chains, enabling the in-register antiparallel orientation. This was observed in an extended MD simulation process, ~ 2 μs, confirming the kinetic trapping of the out-of-register conformations. Therefore, the kinetically trapped out-of-register conformation can self-

assemble and form higher order oligomers without changing the out-of-register conformation. Oligomers assembled with the in-register dimer should be structurally different. However, it is possible that the first types of oligomers can undergo structural transitions that form the second type of oligomers in the in-register conformation. This is supported by the recent publication that observed the out-of-register conformations of β2-microglobulin hexapeptide in crystals [26]. The model of conformational transitions within oligomers was proposed in a study of β-lactoglobulin aggregation [27].

Although we described above the analyses for antiparallel dimers, it would be interesting to compare this analysis with the one for the parallel arrangement of monomers. We also took the parallel β-sheet structure with same sequence from the two consecutive monomers on Aβ fibril as control case of Aβ dimer and performed the rupture simulations. A representative force curve is shown in Figure 3.12. There are peaks at ~ 2 nm, ~ 4 nm and ~ 6 nm corresponding to the step-wise dimer unzipping, but their amplitudes are slightly above the noise level. These data are very different from pulling of antiparallel dimers that do have well-defined peaks (Figures 3.4 and 3.6).

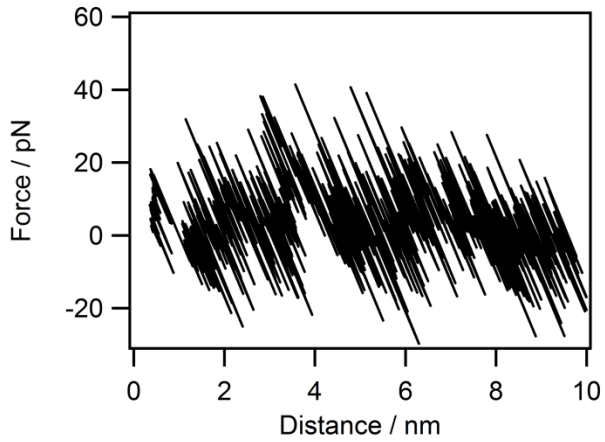

Figure 3.12. A typical rupture force curve of the parallel Aβ dimer with the in-register arrangement at 300 K. The distance in the graphs corresponds to the distances between the Cα atoms of the N-terminal Cys residues.

3.4. CONCLUSION

Overall, our simulations revealed that the dimers formed by Aβ and Sup35 have structural variability with different secondary structure and differences in their dynamics. However, we also identified some similarities in their structures. The formation of dimers with diverse structures can lead to different aggregation pathways and produce oligomers with different structures that may have physiological significance. Although we used the MCP approach to analyze short peptides, the application of the approach to larger systems is possible, as demonstrated by the analysis of titin and ubiquitin proteins. The development of the modified MCP computational approach opens prospects for the structural characterization of large protein systems probed by AFM.

REFERENCES

[1] Lovas, S., Y. Zhang, J. Yu, and Y. L. Lyubchenko. 2013. Molecular Mechanism of Misfolding and Aggregation of Aβ(13–23). J. Phys. Chem. B. 117:6175-6186.

[2] Lemkul, J. A., and D. R. Bevan. 2010. Assessing the Stability of Alzheimer's Amyloid Protofibrils Using Molecular Dynamics. J. Phys. Chem. B. 114:1652-1660.

[3] Lee, E. H., J. Hsin, M. Sotomayor, G. Comellas, and K. Schulten. 2009. Discovery Through the Computational Microscope. Structure. 17:1295-1306.

[4] Rico, F., L. Gonzalez, I. Casuso, M. Puig-Vidal, and S. Scheuring. 2013. High-Speed Force Spectroscopy Unfolds Titin at the Velocity of Molecular Dynamics Simulations. Science. 342:741-743.

[5] Jonsson, S. A. E., S. Mitternacht, and A. Irback. 2013. Mechanical resistance in unstructured proteins. Biophys. J. 104:2725-2732.

[6] Bernstein, F. C., T. F. Koetzle, G. J. Williams, E. F. Meyer, Jr., M. D. Brice, J. R. Rodgers, O. Kennard, T. Shimanouchi, and M. Tasumi. 1977. The Protein Data Bank: a computer-based archival file for macromolecular structures. J. Mol. Biol. 112:535-542.

[7] Irback, A., and S. Mohanty. 2006. PROFASI: A Monte Carlo simulation package for protein folding and aggregation. J. Comput. Chem. 27:1548-1555.

[8] Hess, B., C. Kutzner, D. van der Spoel, and E. Lindahl. 2008. GROMACS 4: Algorithms for Highly Efficient, Load-Balanced, and Scalable Molecular Simulation. J. Chem. Theory Comput. 4:435-447.

[9] Lindorff-Larsen, K., S. Piana, K. Palmo, P. Maragakis, J. L. Klepeis, R. O. Dror, and D. E. Shaw. 2010. Improved side-chain torsion potentials for the Amber ff99SB protein force field. Proteins. 78:1950-1958.

[10] Hess, B., H. Bekker, H. J. C. Berendsen, and J. G. E. M. Fraaije. 1997. LINCS: A linear constraint solver for molecular simulations. J. Comput. Chem. 18:1463-1472.

[11] Berendsen, H. J. C., J. P. M. Postma, W. F. van Gunsteren, A. DiNola, and J. R. Haak. 1984. Molecular dynamics with coupling to an external bath. J. Chem. Phys. 81:3684-3690.

[12] Mu, Y., P. H. Nguyen, and G. Stock. 2005. Energy landscape of a small peptide revealed by dihedral angle principal component analysis. Proteins: Structure, Function, and Bioinformatics. 58:45-52.

[13] Evans, E., and K. Ritchie. 1997. Dynamic strength of molecular adhesion bonds. Biophys. J. 72:1541-1555.

[14] Guo, S., N. Li, N. Lad, S. Desai, and B. B. Akhremitchev. 2010. Distributions of Parameters and Features of Multiple Bond Ruptures in Force Spectroscopy by Atomic Force Microscopy. J. Phys. Chem. C. 114:8755-8765.

[15] Carrion-Vazquez, M., A. F. Oberhauser, S. B. Fowler, P. E. Marszalek, S. E. Broedel, J. Clarke, and J. M. Fernandez. 1999. Mechanical and chemical unfolding of a single protein: A comparison. Proc. Natl. Acad. Sci. USA. 96:3694-3699.

[16] Fisher, T. E., P. E. Marszalek, and J. M. Fernandez. 2000. Stretching single molecules into novel conformations using the atomic force microscope. Nat. Struct. Mol. Biol. 7:719-724.

[17] Carrion-Vazquez, M., H. Li, H. Lu, P. E. Marszalek, A. F. Oberhauser, and J. M. Fernandez. 2003. The mechanical stability of ubiquitin is linkage dependent. Nat. Struct. Mol. Biol. 10:738-743.

[18] Improta, S., A. S. Politou, and A. Pastore. 1996. Immunoglobulin-like modules from titin I-band: extensible components of muscle elasticity. Structure. 4:323-337.

[19] Sikora, M., J. I. Sułkowska, and M. Cieplak. 2009. Mechanical Strength of 17 134 Model Proteins and Cysteine Slipknots. PLoS Comput. Biol. 5:e1000547.

[20] Vijay-Kumar, S., C. E. Bugg, and W. J. Cook. 1987. Structure of ubiquitin refined at 1.8Åresolution. Journal of molecular biology. 194:531-544.

[21] Portillo, A. M., A. V. Krasnoslobodtsev, and Y. L. Lyubchenko. 2012. Effect of electrostatics on aggregation of prion protein Sup35 peptide. J. Phys. Condens. Matter. 24:164205.

[22] Buzsaki, G., and K. Mizuseki. 2014. The log-dynamic brain: how skewed distributions affect network operations. Nat. Rev. Neurosci. 15:264-278.

[23] Kmiecik, S., M. Jamroz, and A. Kolinski. 2011. Multiscale Approach to Protein Folding Dynamics. In Multiscale Approaches to Protein Modeling. A. Kolinski, editor. Springer New York. 281-293.

[24] Srivastava, A., and P. V. Balaji. 2012. Size, orientation and organization of oligomers that nucleate amyloid fibrils: Clues from MD simulations of pre-formed aggregates. BBA-Proteins Proteom. 1824:963-973.

[25] Nelson, R., M. R. Sawaya, M. Balbirnie, A. O. Madsen, C. Riekel, R. Grothe, and D. Eisenberg. 2005. Structure of the cross-beta spine of amyloid-like fibrils. Nature. 435:773-778.

[26] Liu, C., M. Zhao, L. Jiang, P.-N. Cheng, J. Park, M. R. Sawaya, A. Pensalfini, D. Gou, A. J. Berk, C. G. Glabe, J. Nowick, and D. Eisenberg. 2012. Out-of-register β-sheets suggest a pathway to toxic amyloid aggregates. Proc. Natl. Acad. Sci. USA. 109:20913-20918.

[27] Giurleo, J. T., X. He, and D. S. Talaga. 2008. β-Lactoglobulin Assembles into Amyloid through Sequential Aggregated Intermediates. J. Mol. Biol. 381:1332-1348.

APPENDIX 3.1. C source code of the A2Aspring function in the modified PROFASI software package

```
/*************************************************************
   PROFASI: Protein Folding and Aggregation Simulator, Version 1.5
   Copyright (C) (2012)  Anders Irback and Sandipan Mohanty
   Email: profasi@thep.lu.se
   Home Page: http://cbbp.thep.lu.se/activities/profasi/
   Version control (git) : https://trac.version.fz-juelich.de/PROFASI

   This program is free software; you can redistribute it and/or modify
   it under the terms of the GNU General Public License
   (see PROFASI/gpl.txt).

   This program is distributed in the hope that it will be useful,
   but WITHOUT ANY WARRANTY; without even the implied warranty of
   MERCHANTABILITY or FITNESS FOR A PARTICULAR PURPOSE.  See the
   GNU General Public License for more details.
   A2Aspring function is added by Yuliang Zhang with permission.
 *************************************************************/
// A2Aspring function is added by Yuliang Zhang with permission, Aug, 28, 2013, UNMC, OMAHA.

#include "A2ASpring.hh"
#include <cmath>
#include <fstream>

using namespace std;
```

```
using UnivConstants::pi;

namespace prf {

   A2ASpring::A2ASpring() : Energy() {
      Name("A2ASpring");
      R = 0;
      k = 0;
      a1 = 0;
      a2 = 0;
   }

   A2ASpring::~A2ASpring() {
   }

   void A2ASpring::init() {
      R = AtomCoordinates::dist(a1,a2);
      initialized = true;
   }

   void A2ASpring::pull() {
      R += pullRate;
   }

   double A2ASpring::evaluate() {
      delv = 0;
      double r = AtomCoordinates::dist(a1,a2);
```

```
    vval = 0.5 * k * (R - r)*(R - r);
    return vval;
}

double A2ASpring::getForce() {
    double r = AtomCoordinates::dist(a1,a2);
    return k * (R - r);
}

double A2ASpring::deltaE(Update *updt) {
    double eold = vval;
    evaluate();
    delv = (vval - eold);
    vval = eold;
    return delv;
}

void A2ASpring::Accept(Update *updt) {
    vval += delv;
    pull();
}

void A2ASpring::Revert(Update *updt) {
    pull();
}

void A2ASpring::rangeEstimate(double &x1, double &x2) {
```

```
    x1 = 0.0;
    double maxLength = 2*3.6*p->Chain(0)->numAminoAcids();
        x2 = 0.5 * k * maxLength*maxLength;
}

void A2ASpring::forceRangeEstimate(double &x1, double &x2) {
    x1 = 0.0;
    double maxLength = 2*3.6*p->Chain(0)->numAminoAcids();
        x2 = k*maxLength;
}

void A2ASpring::saveState(std::string pullfile) {
    std::ofstream output_file(pullfile.c_str(), ios::binary);
    output_file.write((char*) &R, sizeof (R));
    output_file.close();

    prf::cout << "Stored pulling distance: " << R << "\n";
}

void A2ASpring::recoverState(std::string pullfile) {
    std::ifstream input_file(pullfile.c_str(), ios::binary);
    input_file.read((char*) &R, sizeof (R));
    prf::cout << "Recovered pulling distance: " << R << "\n";
}

}
```

Chapter 4

AMYLOID PROTEIN Aβ42 STRUCTURE, DYNAMICS AND SELF-ASSEMBLY IN DIMERS

4.1. INTRODUCTION

In Chapters 2 and 3, the goal to characterize the dimer characteristic from short amyloid peptide fragment has been successfully attained using the combination of AFM based single molecular force spectroscopy (SMFS), conventional MD (cMD) simulation [1] and Monte Carlo pulling (MCP) simulation [2]. However, it is still unknown whether the evidence from short peptide is appropriate to interpret the phenomenon in large system. In our setup, the MD simulation is necessary to obtain the meaningful structures. Due to the limitation of current computer resource, the simulation of large protein system, such as Aβ42 protein, α-Syn protein, is still a challenging. Fortunately, the specialized supercomputer—Anton—have been developed to achieve the goal of large biological system modeling [3, 4].

Here, we applied MD simulation to analyze the dimer formation of full-size Aβ42 protein using the most powerful supercomputer, the Anton [3, 4]. Two types of dimers were identified, and the structures of the monomers within the dimers were very different from those observed in fibrils. Validation of different dimer models using the MCP approach ruled out the formation of dimers with extended β-structures that exist in fibrils. To distinguish between the dimers identified by the MD simulations, we developed another approach enabling us to select the most appropriate dimer type. The role of dimer

structures and dynamics in further aggregation processes and possible dimer neurotoxicity are also discussed.

4.2. METHODS

4.2.1. Monomer simulation procedure:

To generate the initial structure of the monomers for the dimer simulation, we conducted conventional MD (cMD) simulation using GROMACS ver. 4.5.5 [5] using Amber ff99SB-ILDN force field [6] and the TIP3P water model [7]. The initial monomer structure (Figure 4.1A) was adopted from NMR data [8] (PDB ID: 1IYT) obtained in the presence of the hexafluoroisopropanol (HFIP) : water solvent ratio of 80 : 20. To mimic the experimental design, a Cys residue was added to the N-terminus. The index of this Cys residue was set to 0 to keep the original numbering of the other residues as the actual Aβ42 protein. Then, the structure was solvated in a truncated octahedron box with 10620 TIP3P water molecules. The minimum distance between the protein surface and the edges of the water box was 1.5 nm, so that any interactions from the structure and its own periodic copy, due to periodic boundary condition (PBC), are avoided. The Lys and Arg residues were treated at the protonation stage to mimic the neutral pH conditions,at which both Lys and Arg contain 1 positive charge. The nitrogen atoms at the δ position of the His residues were protonated as well. 32 Na^+ and 29 Cl^- ions were added to neutralize the system charges and keep the constant salt concentration of 150 mM. Other details of the simulations setup were described in our prior work [1]. The initial equilibration, 500 ns NPT — constant number, constant pressure (1 bar) and constant temperature (300 K) — cMD simulation was submitted to the Holland Computing Center (HCC). After a 500 ns

simulation time, a cluster analysis was performed through g_cluster command in the GROMACS package employing the GROMOS method of clustering and root-mean square deviation (RMSD) for protein backbone with a 3Å cut-off value, as previously described [1]. Due to large structural fluctuations of residues 1–9 and 36–42, only data for residues 10–35 were selected for cluster analysis.

Furthermore, we addressed secondary structure dynamics according to the method developed by Thirumalai's group [9]. Briefly, if the dihedral angles from two consecutive residues satisfy the definition of an α-helix (-80° ≤ ϕ ≤ -48° and -59°≤ ψ ≤ -27°) and β-strand (-150° ≤ ϕ ≤ -90° and 90 ≤ ψ ≤ 150°), the structures are considered to be α and β conformations, respectively. The $\alpha(t) = \frac{1}{\Delta}\int_t^{t+\Delta} \alpha_s(s)ds$ and $\beta(t) = \frac{1}{\Delta}\int_t^{t+\Delta} \beta_s(s)ds$ are defined as functions of time to monitor the changes of secondary structure, where $\alpha(s) = \frac{1}{41}\sum_{i=1}^{41} \delta_{i,\alpha}$ and $\beta(s) = \frac{1}{41}\sum_{i=1}^{41} \delta_{i,\beta}$ at t =s and the output frequency of MD trajectory Δ=1 ns. When the residues adopt the α or β conformations, the changes from i^{th} residue, $\delta_{i,\alpha} = 1$ or $\delta_{i,\beta} = 1$. The calculations from the first N- and C-terminal residues were not taking into account. Thus, the total number of residues in monomer is 41. The script example of relevant calculations is placed in appendix 4.1.

4.2.2. Dimer simulation on the specialized supercomputer Anton

For simulations on Anton, we used the Maestro-Desmond software package [10] to build the initial dimers, using the same force field and water model as for the monomer MD simulations. To enhance sampling within the finite cubic box, two dimers termed dimer 1 and dimer 2 were created from copies of monomers with different orientations from cluster 1 in Figure 4.1C: in dimer 1 the angle between the long axes of each

monomer was 90° and in dimer 2 a parallel orientation of monomers was built. The two dimers were solvated into the cubic box with the equal edges of 8.2 nm and 8.4 nm along with 18031 and 18397 TIP3P water molecules, respectively. The minimum distance between the proteins and the box edge was 1.5 nm. The initial the center of mass (COM) distance of two monomers was set to 4 nm. Na^+ (56 for dimer 1 and 57 for dimer 2) and Cl^-(50 for dimer 1 and 51 for dimer 2) ions were placed in the box to neutralize the protein charges as well as to maintain an ionic concentration of 150 mM. The protonation of charged residues was processed the same way as the monomer simulations. The viparr.py script from Maestro-Desmond package was employed to load the Amber ff99SB-ILDN force field and TIP3P water model and to constrain the mobility of the hydrogen atoms using the M-SHAKE algorithm [11]. Then, for each dimer case, the systems were equilibrated using 20 ns NPT cMD simulations on HCC cluster provided by University of Nebraska. The resulting systems from the last frame of the 20 ns simulations were chosen as the initial input for the 4 μs cMD simulation runs on Anton. The input parameters were optimized by the guess_chem command available on the Anton machine. The multigrator scheme from Anton was used to achieve the elevated flexibility of the setup in the integration steps. All simulations utilized the Martyna-Tobias-Klein (MTK) [12] and the Nosé-Hoover algorithms [13] for constant pressure of 1 bar and constant temperature of 300 K, respectively. The unbounded interactions beyond 9 Å were ignored and the long-range electrostatics were calculated by the particle-mesh Ewald (PME) algorithm [14] with 64×64×64 grids with 12 Å cut-off. The integration time step was 2 fs and the output frequency was 240 ps. After running 4 μs cMD simulation on Anton, the equilibrated structures of two dimers from last 150 ns

trajectories were used to determine the intermolecular contacts by g_mdmat command from GROMACS package [5].

The calculation of the time-dependent secondary structure changes is the same as in the aforementioned monomer simulation section. Here, $\alpha(s) = \frac{1}{82}\sum_{i=1}^{82}\delta_{i,\alpha}$ and $\beta(s) = \frac{1}{82}\sum_{i=1}^{82}\delta_{i,\beta}$ at t = s and Δ=1.2 ns. The calculations from the first N- and C-terminal residues were not taking into account. So, the total number of residues in dimer is 82.

4.2.3. Accelerated MD (aMD) simulation

The resulting dimer structures from the cMD simulations on Anton were selected to perform the Aβ42 dimer simulation by the accelerated MD (aMD) simulation method on GPUs using STAMPEDE at the Texas Advanced Computing Center (TACC) [15]. The simulation procedures were adapted from the description by Pierce, L.C. *et. al.* [16] and the website (URL: http://ambermd.org/tutorials/advanced/tutorial22/). Briefly, the 500 ns aMD simulation was performed via the Amber12 Package [17]. The dimers structures were extracted from the last frames in the cMD simulation on Anton and all the hydrogen atoms were removed to avoid conflicts within the conversion from different MD packages. Then, the tleap command from Ambertool [17] was used to solvate, neutralize, and make a 150 mM NaCl concentration within the dimer systems with the same force field and same solvent model condition as cMD simulations described above. Besides proteins, the final dimer 1 system contained 11480 water molecules, 38 Na^+ ions and 32 Cl^- ions while the final dimer 2 system was composed of 10542 water molecules, 36 Na^+ and 30 Cl^- ions. The charged residues, Lys, Arg and His, were processed in the

same way as described in monomer section. Then, the output products were taken as input files to run 6 step cMD simulations following the online tutorial prescriptions (URL: http://ambermd.org/tutorials/advanced/tutorial22/) for energy minimization and system relaxation.

According to the principle of aMD [16, 18], a bias (boost) potential ΔV(r) is introduced to the original potential energy V(r) to raise the energy surface, which is nearby the minima. Using this method, the proteins are able to escape from potential wells, thereby enhancing of the sampling of the conformational space that is equivalent to the sampling of much longer time scales in cMD simulations. Bias potential is applied conditionally, when the V(r) is smaller than the selected threshold level E, the simulation will be run on the modified potential $V^*(r) = V(r) + \Delta V(r)$; if the V(r) is larger than E, the simulation will be implemented on the true potential $V^*(r) = V(r)$. The ΔV(r) is defined as:

$$\Delta V(r) = \begin{cases} 0, & V(r) \geq E \\ \frac{(E - V(r))^2}{\alpha + (E - V(r))}, & V(r) < E \end{cases} \quad (1)$$

where, V(r) is the original potential energy; E is the predefined threshold for boost energy; and α is tuning parameter that administers the depth and roughness of modified potential energy. The smaller α is, the less rough the modified potential energy would be.

The dual boost approach, in which both torsional and total energies are taken into account [19], was utilized to explore the Aβ42 dimerization process. Parameters for aMD simulation were calculated based on the last step of the cMD relaxation simulation. The appropriate total boost parameters (E_{tot} and α_{tot}) and dihedral boost parameters (E_{dih} and α_{dih}) were calculated according to the procedure from Pierce *et al.* [16] as follows:

In the dimer 1 simulation,

EthreshP: E_{tot}= -118009 kcal mol-1 + (0.16kcal*mol^{-1} $atom^{-1}$ * 35786 atoms) = -112283 kcal mol^{-1}

αP: α_{tot}= (0.16kcal mol^{-1} $atom^{-1}$ * 35786 atoms) = 5726 kcal mol^{-1}

EthreshD: E_{dih}=796 kcal mol^{-1} + (4kcal mol^{-1} $residue^{-1}$ * 86 solute residues) = 1140 kcal mol^{-1}

αD: α_{dih}=(1/5)*(4kcal mol^{-1} $residues^{-1}$ * 86 solute residues) = 68.8 kcal mol^{-1}

In the dimer 2 simulation,

EthreshP: E_{tot}= -108802 kcal mol^{-1} + (0.16kcal*mol^{-1} $atom^{-1}$ * 32968 atoms) = -103527 kcal mol-1

αP: α_{tot}= (0.16kcal mol^{-1} $atom^{-1}$ * 32968 atoms) = 5275 kcal mol^{-1}

EthreshD: E_{dih}=803 kcal mol^{-1} + (4kcal mol^{-1} $residue^{-1}$ * 86 solute residues) = 1147 kcal mol^{-1}

αD: α_{dih}=(1/5)*(4kcal mol^{-1} $residues^{-1}$ * 86 solute residues) = 68.8 kcal mol^{-1}

The two dimers were submitted to STAMPEDE cluster for 500 ns NVT (constant Volume and constant Temperature) aMD simulation. In order to keep the temperature at 300K, the Langevin thermostat was used with collision frequency of 5 ps^{-1}. The cutoff for short-range non-bonded interactions was set to 12 Å. Over 500 ns aMD simulations, the trajectories were analyzed by dihedral Principal Component analysis of backbone (dPCA) [20], in which the artifacts from combining internal and overall motion are minimized,

were used to acquire the representative structures related to lowest energy minima in free energy landscape. The dihedral angles of the terminal residues are ignored. The script example for dihedral angle calculation can be found in appendix 4.2. The following equation for the free energy calculations was used:

$$\Delta G(V1, V2) = -k_B T[\mathrm{Ln}\, P(V1, V2) - P_{max})] \quad (2)$$

where V1 and V2 are the 1st and 2nd largest Principal Components; P(V1,V2) represents the distribution obtained from the histogram of MD data, P_{max} is the maximum value of the distribution, which is subtracted to make sure the $\Delta G=0$ for the lowest free energy minimum; and k_B and T are the Boltzmann constant and the absolute temperature, accordingly. The Fortran program written by Dr. Yuguang Mu was used to perform this analysis.

4.2.4. MC pulling simulation

The MC pulling method, via the modified PROFASI package, was the same as described in our previous publication [2]. Briefly, the two Cα of the N-terminal Cys residues of each monomer were defined as the pulling groups. A virtual spring was attached onto each pulling group and used to stretch them along a vector during the pulling process. The energy dynamics of the spring were calculated by the A2A spring function and the total energy in the course of pulling was described by the following equation,

$$E_{tot} = E(x) + \frac{k}{2}[L_0 + vt - L(x)]^2 \quad (3)$$

where E(x) indicates the energy without an external force, k and t are the spring constant of the virtual spring. L_0 is the initial distance between two Cα atoms of the N-terminal Cys residues of each monomer. L(x) represents the real-time distance between the Cα atoms of Cys residues during pulling and x denotes a protein conformation. When v = 0.1 fm per MC step, the value is equivalent to pulling rate of 600 nm/s. Here, v = 0.083, which is equivalent to pulling rate of 500 nm/s, was used for all of the MC pulling simulations.

4.2.5. Graphic software

The final cluster network in monomer simulations was plotted by Visone [21]. The figures of the contact map and the free energy landscape in the dPCA analysis were generated via Python2.7 [22-24]. The force curves were analyzed by Matlab 2013 (MathWorks Inc., Natick, MA, USA) and the script example is put in appendix 4.3. All of the line plots, scatter plots and distributions were produced by Igor Pro. 6.3.4 (WaveMetrics, Lake Oswego, OR, USA). The statistical significant differences between the force distributions were calculated using the Kolmogorov-Smirnov nonparametric test (SPSS 20.0; IBM Corp, Armonk, NY, USA). The dihedral angles were calculated through VMD software package [25], and the protein snapshots were generated by YASARA (www.yasara.org).

4.3. RESULTS

4.3.1. Equilibrated structures of Aβ42 monomer

Prior to the simulation of Aβ42 dimer structures, we performed MD simulations of Aβ42 monomer to identify equilibrated structures of monomers. We applied this approach in our recent simulations of the dimer structures for Aβ(14-23) peptide [1]. We have shown that the equilibrated structure of the monomer does not depend on the initial conformation of Aβ(14-23) peptide. The Aβ42 monomer candidates were obtained by running 500 ns MD simulations on HCC computer using the all-atom model in TIP3P water as described in Methods section. The initial structure was adopted from NMR coordinates of the Aβ42 monomer (Figure 4.1A, PDB ID: 1IYT) in an organic solution [8]. After the completion of the simulation, we performed cluster analysis to identify the most representative structures of Aβ42 monomers. The classification of clusters in the trajectory was performed with the approach described in paper [26] by calculating the root-mean-square deviation (RSMD) of backbone atoms between all pairs of structures with a cut-off at 0.3 nm. The results of the cluster analysis are shown in Figure 4.1B. Twelve clusters were identified with the 1^{st} cluster comprising 53.73% of the entire population. The 2^{nd} cluster is the next largest (35.61%), but this cluster can be linked to the 1^{st} cluster via the linker node 5. Frequent transitions are also observed between the 1^{st} cluster and a number of other less populated clusters. For example, the 4^{th} cluster (probability = 0.15) and the 6^{th} cluster (probability = 0.11), display the equilibrium between cluster 1 and other clusters. The conformational variability is primarily defined by the conversion of two stable helical conformations of the initial structure encompassing residues Ser8-Gly25 and Lys28-Met35 to the conformers with low α-helix and low β-strand contents.

To structurally characterize monomer dynamics, we monitored the overall secondary structure changes according to the method described in [9] (details in Methods section). The analysis of the time-dependent contents of α-helix and β-structures ($\alpha(t)$ and $\beta(t)$) reveals that the α-to-β transition occurs after 200 ns (Figure 4.1C**)** indicating that detection of such a conversion requires long simulation times. The monomer structure remains quite dynamic, so in the time-interval between 200 ns and 500 ns, the α-helix and β-strand contents (fractions) fluctuate rather broadly, 0.08 ± 0.05 and 0.03 ± 0.03, respectively. Based on the analysis of the Aβ42 monomer conformation and dynamics, we selected monomers from the 1st cluster to analyze the conformational dynamics of Aβ42 dimers with the Anton supercomputer.

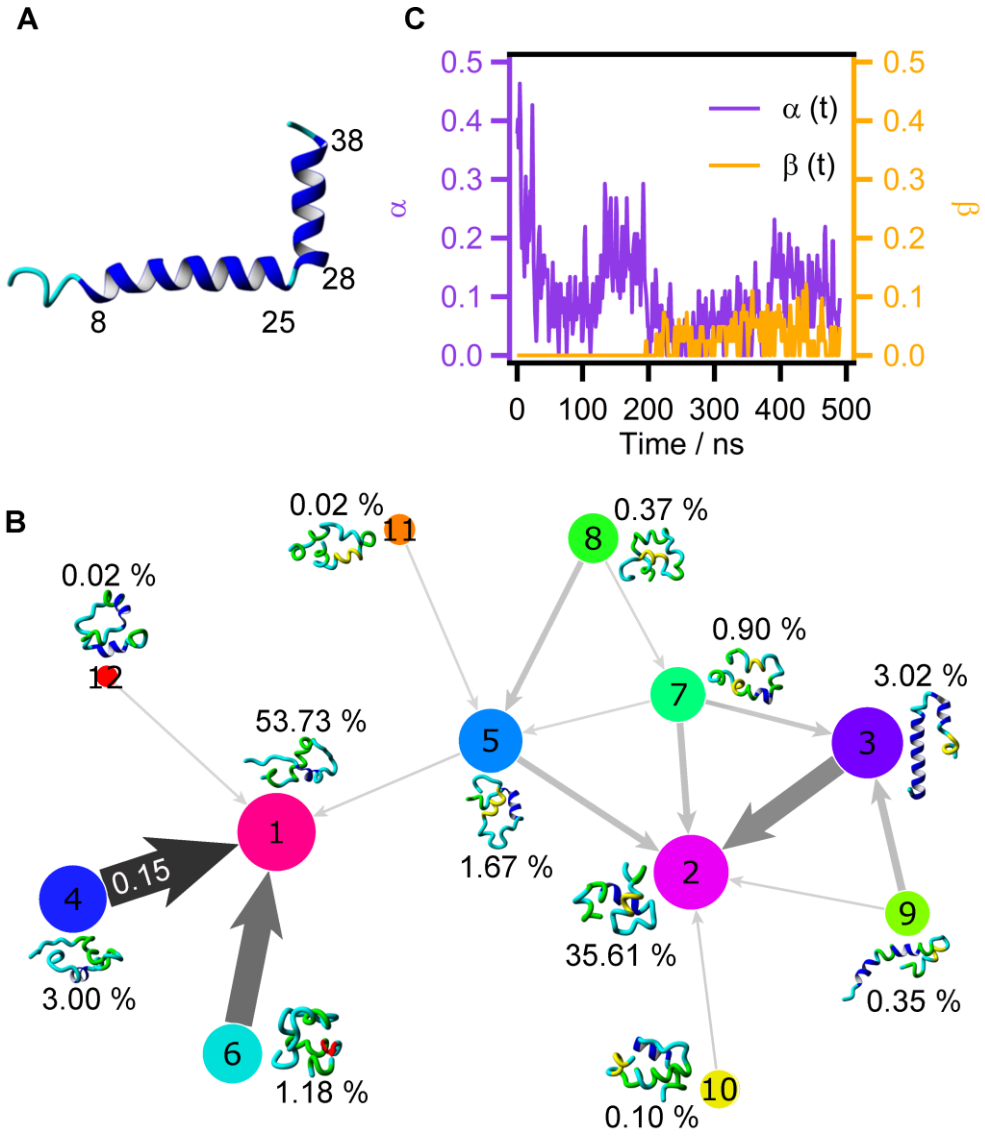

Figure 4.1. The Aβ42 monomer simulation. (A) The initial structure for Aβ42 monomer simulation. The coordinates of Aβ42 monomers were taken from Protein Database Bank (PDB ID: 1IYT. Two helical regions are represented by blue ribbon, encompassing residues 8-25 and 28-38. The rest of residues are shown as cyan tube. (B) The transition network for Aβ42 monomer. The colored nodes indicate the cluster structures based on the analysis of simulation trajectory. The circle sizes visually illustrate the node population (percentage). The snapshots of clusters are placed around the homologous nodes. Color-coding for the snapshots: blue indicate α-helix; green tubes stand for turn structure; cyan tubes represent random coil and red arrow denotes β-sheet. Transition between nodes is indicated with arrows with the width illustrating probabilities of transitions. The largest probability is 0.15 (black arrow). (C) Time dependent dynamics of secondary structures. The purple curves are from the fractions of α-helix content and the orange ones indicate the fluctuation of the fractions of β-strand content over time.

4.3.2. Structure of Aβ42 dimers

Two Aβ42 monomers were placed at a center of mass distance (COM) of ~4 nm and two types of the dimers differing by their relative monomer orientations were made (Figure 4.2A,B). To avoid contacts of monomers within dimer at initial step of MD simulation in such a limited space, two arrangements of the monomers within the initial dimeric complex were made. In dimer 1 (Figure 4.2A), the monomers were placed in an orthogonal configuration relative to the long axis of the monomers, whereas in dimer 2 (Figure 4.2B) a parallel orientation of the monomers was chosen. Two representative snapshots for dimers 1 and 2 are shown in Figure 4.2C and D, respectively. The simulation did not reveal the formation of long β-structures as it was found in the fibrillar structures of Aβ42 protein [27]. In the dimers, interactions between the monomers are limited to short stretches of the proteins, as depicted in the interaction maps for the dimers in Figure 4.2E, F. The primary interactions between the monomers for both types of dimers are within the Central Hydrophobic Cluster (CHC) region spanning from Leu17 to Ala21 and the C-terminal region between Ile31and Ala42 residues. Differences in the dimers structures were observed. Dimer 1 primarily contains hydrophobic interactions lacking intermolecular hydrogen bonding, while dimer 2 is stabilized by both hydrophobic interactions and a few intermolecular hydrogen bonds from residues on CHC regions. The time dependent change of the dimers secondary structure were calculated and the variably of α-helix ($\alpha(t)$) and β-structure ($\beta(t)$) is shown in Figure 4.3A,B for dimers 1 and 2, respectively. The graphs show that both parameters in the dimers initially (200 ns - 500 ns) fluctuate in the range of 50% or above, but remain constant after the 2 μs simulation time, which is an additional evidence for reaching

equilibrium. However, regardless of this fact we cannot exclude the possibility that the dimers are trapped in local energy minima, meaning that the conformational space is not sufficiently sampled during the simulations.

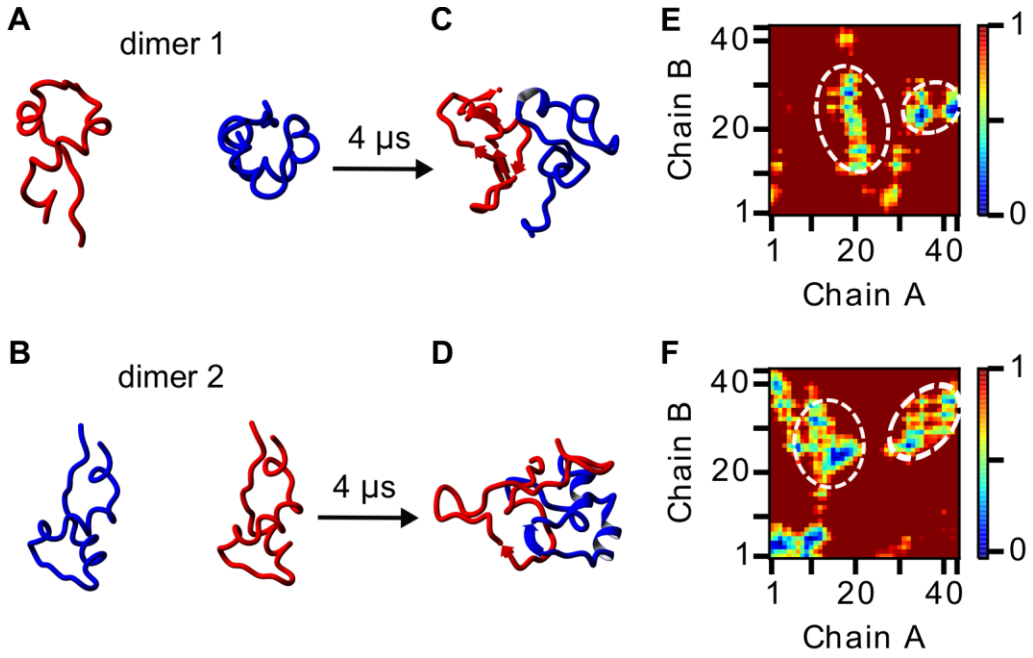

Figure 4.2. The Aβ42 dimer simulation on specialized supper computer Anton. Two copies of monomers from node 1 are selected to build the two initial dimers: (A) Schematic for assembly dimer 1 in which one monomer is rotated by 90° relative to another; (B) In dimer 2, two monomers are placed in the parallel orientation. (C,D) The snapshots of dimers corresponding to the last frames of the 4 μs simulation runs. In all snapshots (A-D), the red and blue indicate monomer A and B, respectively. (E,F) The contact maps of each dimer. The colors in the contact maps represent the distance in nm between pairwise residues. The regions of interest are encircled with dashed lines.

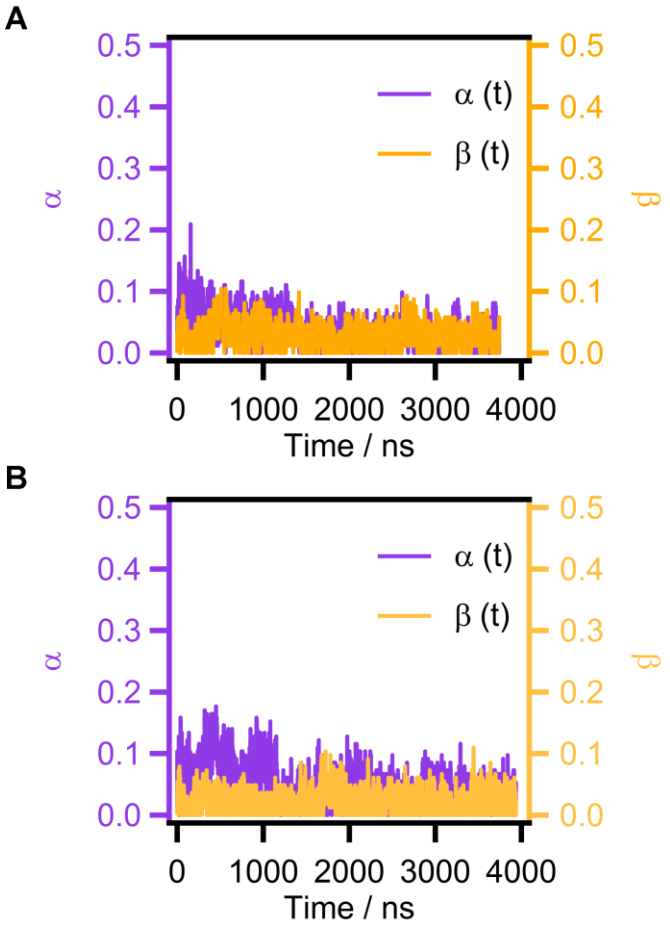

Figure 4.3. Time-dependent dynamics of the α-helix and β-strand contents in dimer 1 (A) and dimer 2 (B) obtained from cMD simulations (Anton computer). The purple and orange correspond to the α-helix and β-strand contents variations over time.

To address this issue, we extended the dimer simulation using accelerated MD (aMD) simulation (Methods section), in which two boost energies are introduced to the whole system to enhance conformational sampling [18, 28, 29]. According to ref. [16], sampling during several hundred nanoseconds of aMD simulation is equivalent to sampling in the millisecond time scale for cMD simulation, suggesting that with aMD we should be able to extend the sampling period over several orders of magnitude. Note a recent application of the aMD approach to the larger Aβ-αSyn co-assembly system [30], thereby justifying the suitability of this approach for Aβ42 dimer simulation.

The results of the 500 ns aMD simulations for dimers 1 and 2 depicted as energy landscapes are shown in Figure 4.4A and B, respectively, in which the dihedral Principle Component Analysis (dPCA) was applied [20]. A series of energy minima shown in blue color are seen for the both dimers. Snapshots of representative structures corresponding to these local minima are indicated in the plots. As seen from the structures, even such an extended MD simulation did not lead to dimers structures with extended β-sheet formations. Consistent with the cMD Anton simulations, the CHC regions (Leu17-Ala21) and the C-terminal hydrophobic regions of two monomers participate in the dimer formation and maintaining the dimers stability. Notably, the extended simulation did not eliminate structural differences between the both dimers. Dimer 1 is stabilized by intermolecular β-sheet structures (Figure 4.4A), whereas one monomer in dimer 2 tends to form an α-helix structure (Figure 4.4B). Conformational analysis in which the content of α-helixes and β-strands were calculated as functions of time was performed and the results are shown in Figure 4.5A,B for dimers 1 and 2, respectively. A slightly higher β-strand content (~0.05 vs. ~ 0.02) was observed for dimer 1, but dimer 2 was characterized

by the elevated α-helix content (~0.14 vs. ~0.06). The α-helix content in dimer 2 is 0.14 ± 0.04, which is twice that of dimer 1, 0.06 ± 0.02 (Figure 4.5A,B).

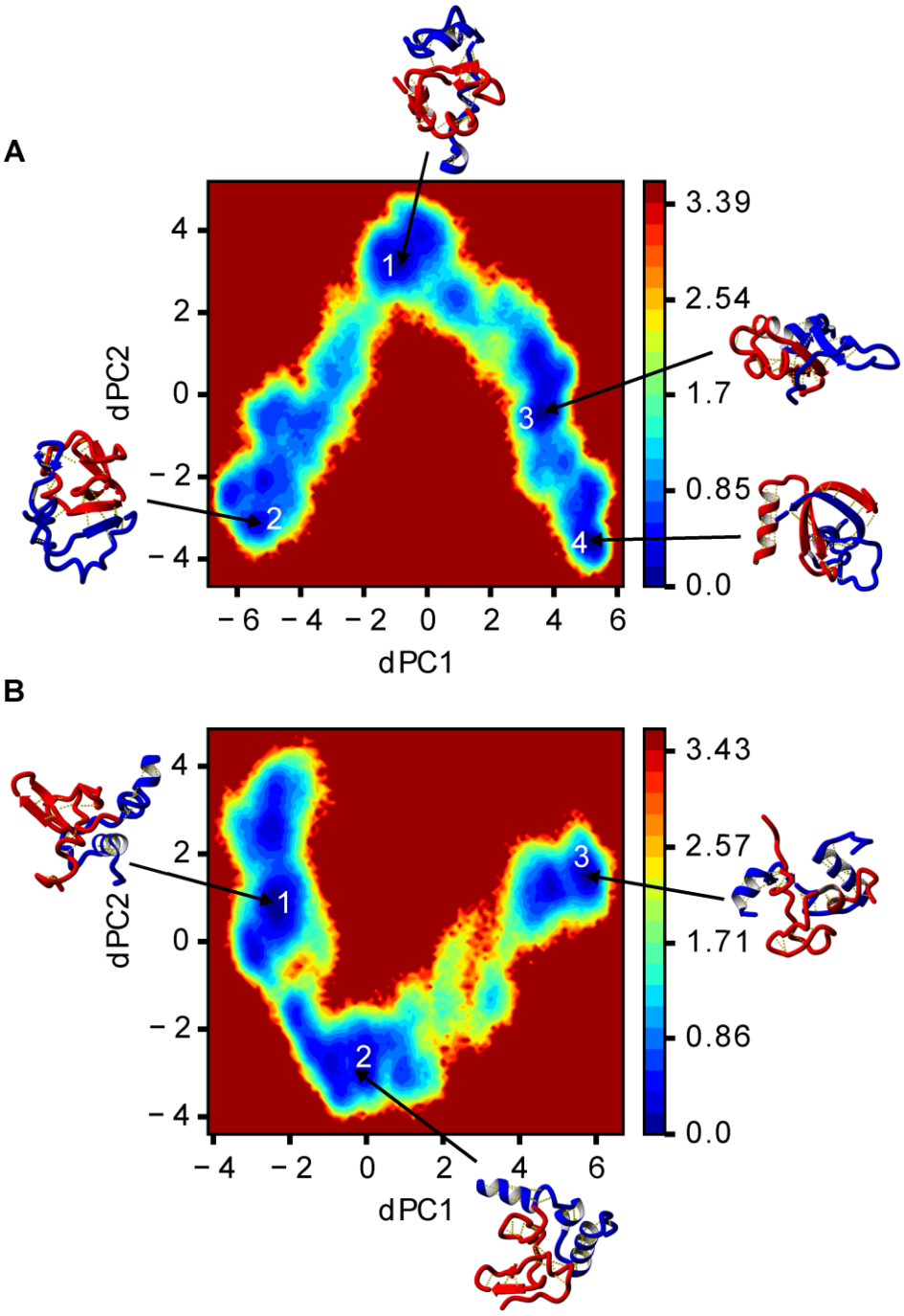

Figure 4.4. The results of accelerated MD (aMD) simulation of Aβ42 dimer 1 (A) and dimer 2 (B). The free energy landscapes were constructed after 500 ns aMD simulations. Four local energy minima (A) and threes local energy minima (B) for both dimers are indicated with arrows. The corresponding snapshots are shown. In the snapshots, monomers A and B are colored with red and blue, respectively.

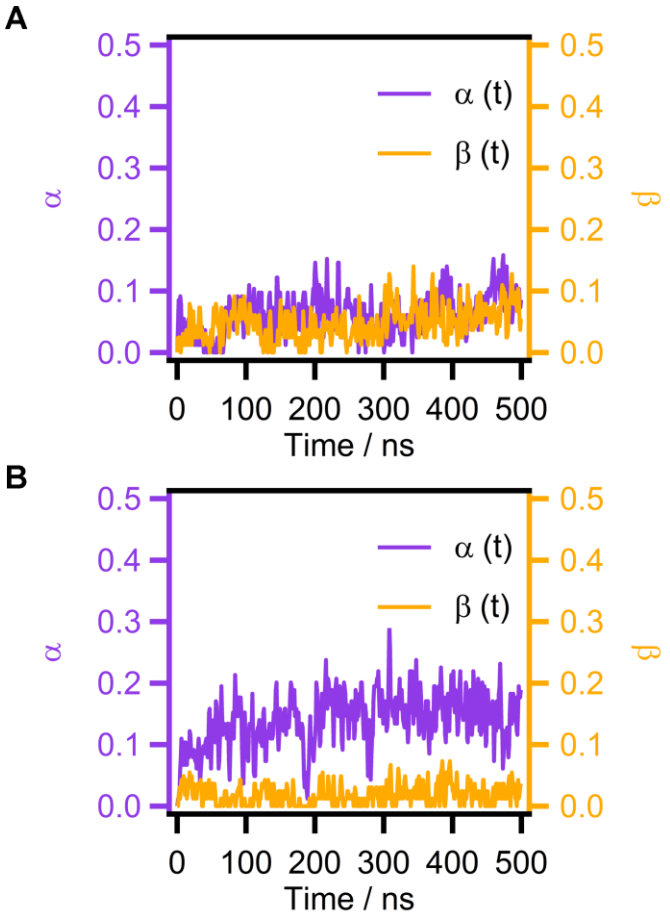

Figure 4.5. The time dependent changes of α-helix (purple) and β-strand contents (orange) from aMD simulations for dimer 1 (A) and dimer 2 (B).

4.3.3. Validation of MD simulations

To validate the MD simulation data, we used our recently developed approach [2] (details in chapter 3), in which the simulated structures are ranked by comparing the rupture force values calculated for the simulated dimer structures with experimental results. The rupture process is simulated with the use of the MCP approach that allows the simulation of the rupture process at pulling rates similar to those used in the experiment. The latter is a critical issue because the rupture value depends on the pulling rate [1]. Seven initial configurations were chosen from the representative dimer 1 and dimer 2 aMD simulations (Figure 4.4) and MCP simulations for each dimer configuration, and MCP probing was repeated 500 times to obtain a statistically significant dataset.

The results for MCP simulations for both dimers are shown in Figure 4.6 along with experimental results obtained from our paper [31]. . The data demonstrate that distributions for simulated dimers are very similar to the mean rupture force values of ~50 pN and the width of the force distributions (Figure 4.6A,B) and both results are very close to the force distributions of the experimental data (Figure 4.6C). Additionally, statistical analysis with the use of Kolmogorov-Smirnov nonparametric test was performed (Figure 4.6D). The geometric mean force value of 57.1 ± 1 pN from experiment is very close to the force value for the structure in the No.1 energy minimum of dimer 1 (Figure 4.4A), 58.1 ± 1 pN ($p = 0.346$). The force value for the structure in the No.1 energy minima of dimer 2 is 55.3 ± 1 pN, which is slightly different from the experimental data ($p = 0.032$).

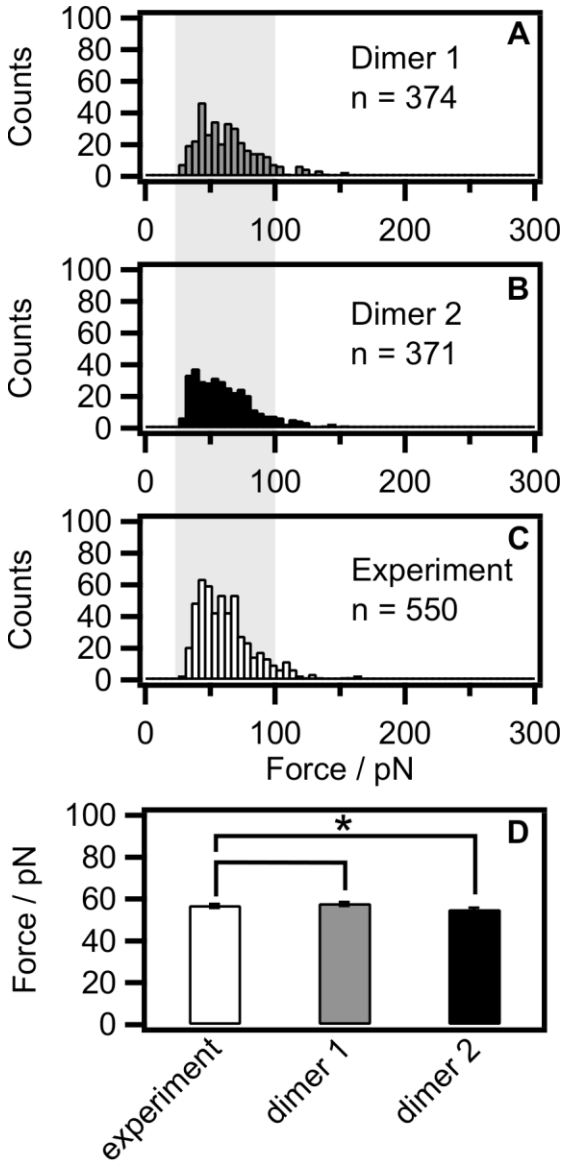

Figure 4.6. The histograms for rupture force distributions for simulations (A, B) and experiment (C). The number of force curves analyzed (n) is indicated. (D) The statistical analysis utilizing Kolmogorov-Smirnov nonparametric test. The * symbol indicates the significant difference ($p<0.05$). Error bars are S.E. values.

For structural comparison, a similar MCP analysis was performed for tAβ42 protein dimers with structures taken from the fibrils. Along with the dimer structures for U-shaped fibrils [27], we tested the dimer structure for the recently published S-shaped fibrils [32] schematically shown as U-shaped and S-shaped dimers in Figure 4.7A-D, in which cases the N-terminal residues were added and prior to the MCP simulations, the equilibrated structures of dimers were obtained by regularize function in PROFASI software [33]. The results for the rupture force distributions are shown in Figure 4.7E,F. The mean values of the rupture forces were 130.4 ± 1 pN and 107.4 ± 1 pN for U-shaped and S-shaped dimers, respectively. Both values are significantly different from the experimental data (Figure 4.7G), suggesting that the probability of formation of these types of dimers is very low.

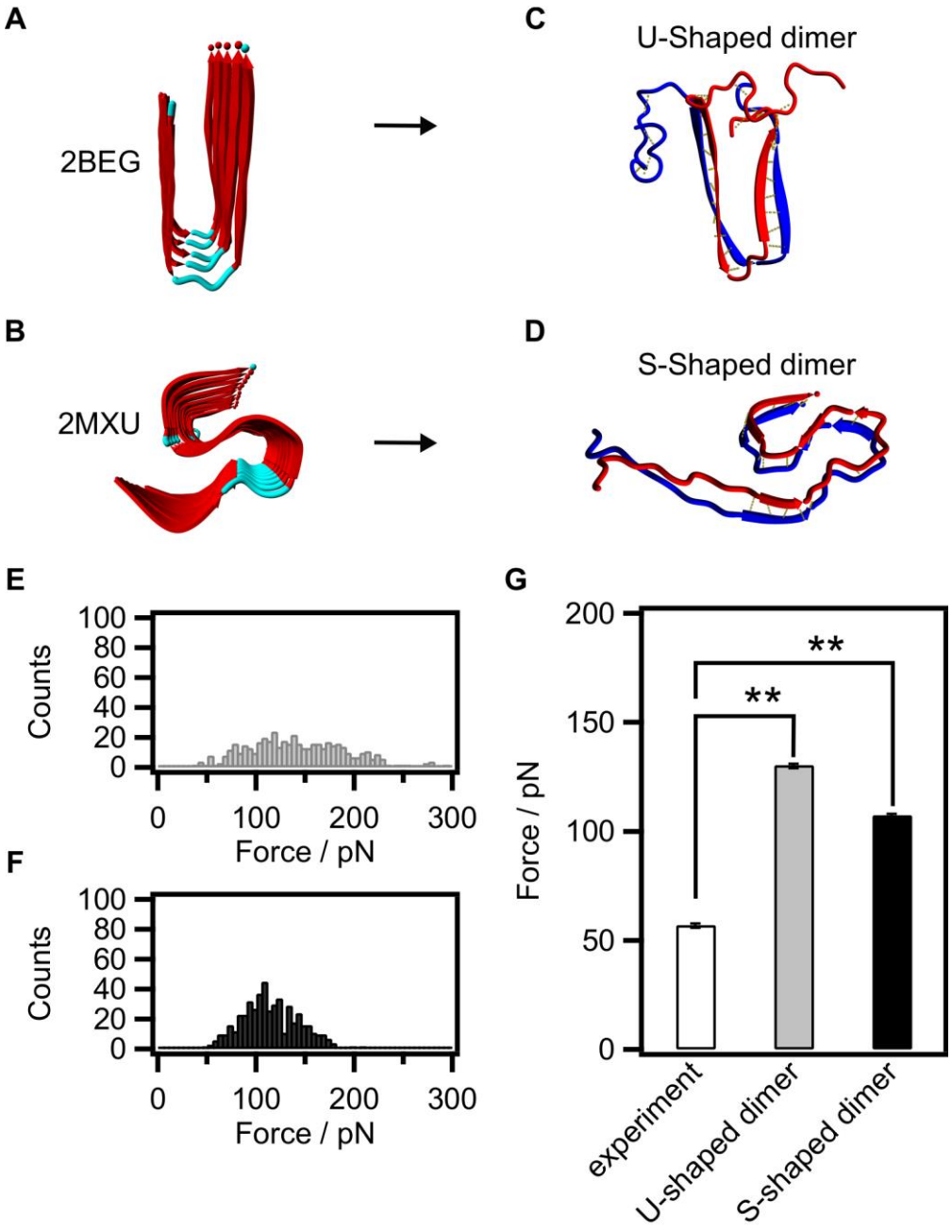

Figure 4.7. The pulling (MCP) simulation of Aβ42 dimers from two fibrillar structures - U-shaped (A; PDB ID: 2BEG) and S-shaped (B; PDB ID: 2MXU). The corresponding structures of dimers are shown in (C) and (D). The monomers in (C) and (D) are shown in different colors. The rupture forces histograms are shown in (F) and (F) for U-shaped and S-shaped dimers, respectively. (G) The Kolmogorov-Smirnov non-parametric statistical analysis for the correlation between experiment and simulations. The ** symbols indicate that $p < 0.01$. Error bars are S.E. values.

AFM force spectroscopy probing of Aβ42 dimers and rupture force data allow the measurement of contour lengths that provides information regarding the interaction pattern of monomers [31]. The experiments revealed non-monotonous three-peak rupture lengths distributions suggesting that the C-terminal residues provide an important contribution to Aβ42 dimer stability [31]. We simulated the interaction profiles for dimers 1 and 2 using the force curve analysis, similar to the one used in the experiment (Methods section). The results are summarized in Figures 4.8 and 4.9. In this figure, plots (Figure 4.8) and (Figure 4.9) are the 2D scattered plots for dimers 1 and 2, respectively. The rupture force values for each rupture length are shown as green dots. The distributions of the rupture distances obtained from this dataset are shown as red histogram on the top. The rupture forces distributions are shown in blue to the right of the scattered plots. The scattered data are grouped as evidenced by three peaks on the rupture length histograms (red), suggesting that there are three distinct interacting regions, corresponding to the rupture distances of ~4 nm, ~8 nm, and ~12 nm for both dimers (Figures 4.8 and 4.9). Both distributions are rather similar, although populations of the long-rupture events (~12 nm) are the most populated ones whereas the rupture lengths distributions for dimer 2 are of similar size (Figures 4.8 and 4.9). The experimental results in paper [31] show very similar three-peak distributions in which peak three is the most representative one, suggesting that dimer 1 is the best candidate for the experimental probing of Aβ42 dimers.

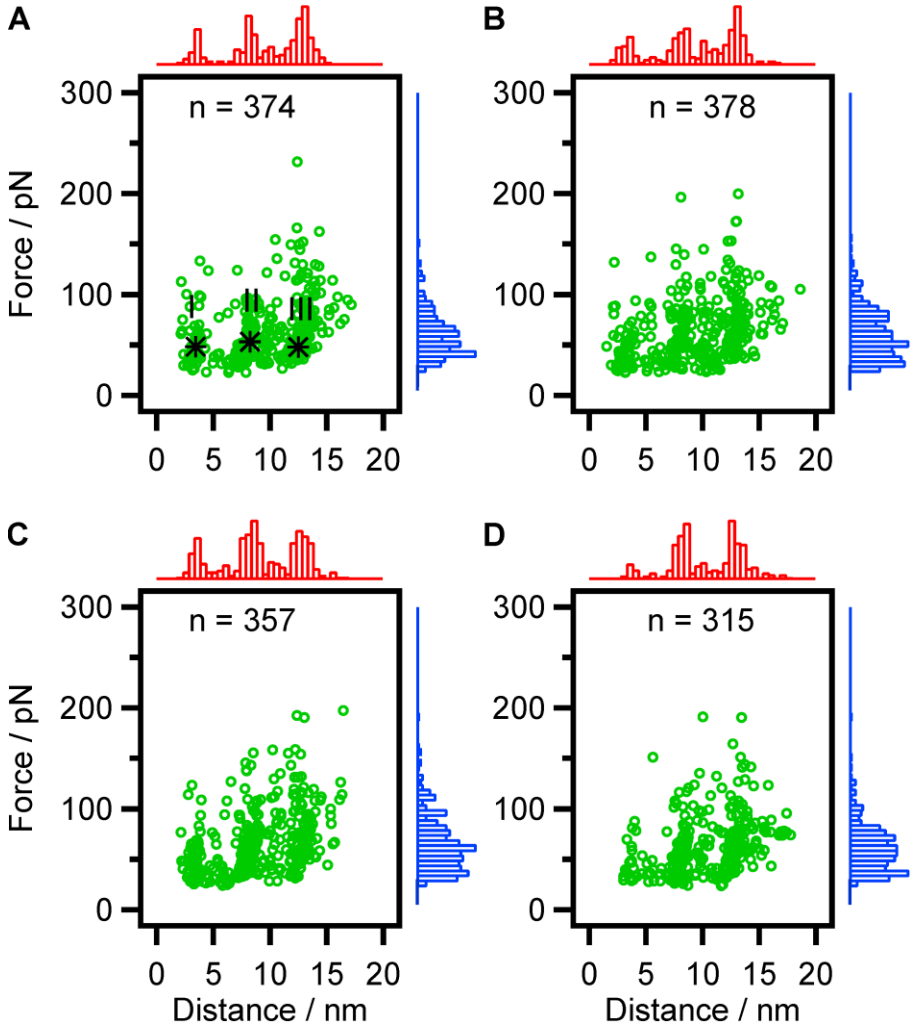

Figure 4.8. The rupture patterns (A-D) of additional major structures for Aβ42 dimer 1 in Figure 4.4A (structures 1-4) obtained by MCP simulations. Each rupture force and the corresponding rupture length are indicated with green circles. The distributions of forces are shown as blue histogram and placed on the right side of the scatter plot. The rupture lengths distributions (red histogram) are placed at top of the plot. The black * symbols in A are the centroids from highest density areas of scatter points indicating the different pattern regions, labeled by I to III.

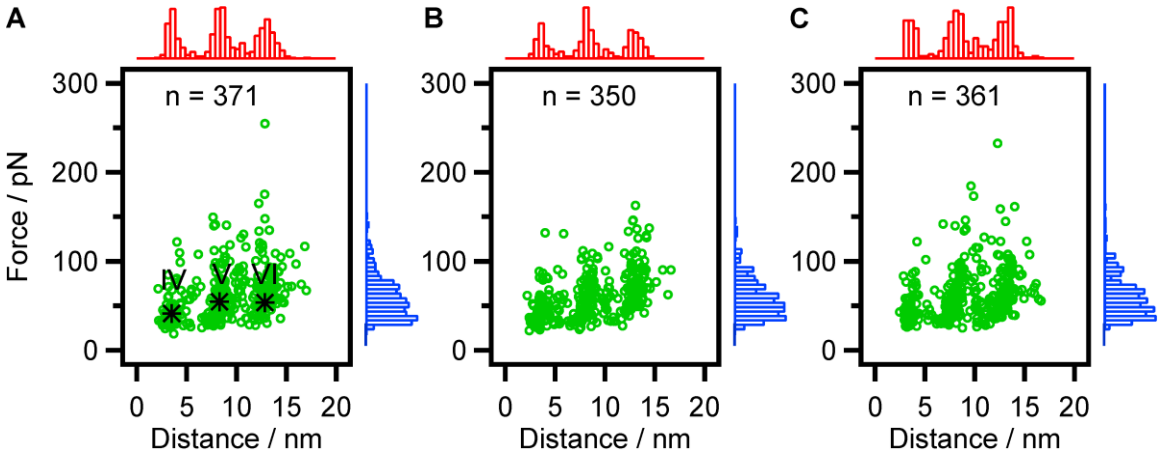

Figure 4.9. The rupture patterns (A-C) of additional major structures for Aβ42 dimer 2 in Figure 4.4B (structures 2 and 3) obtained by MCP simulations. Each rupture force and the corresponding rupture length are indicated with green circles. The distributions of forces are shown as blue histogram and placed on the right side of the scatter plot. The rupture lengths distributions (red histogram) are placed at top of the plot. The black * symbols in A are the centroids from highest density areas of scatter points indicating the different pattern regions, labeled by IV to VI.

We took advantages of MCP to visualize the pulling process and characterize rupture events corresponding to the three clusters identified in the scatter plots in Figure 4.8A and Figure 4.9A. The analysis was performed for the rupture events circled around the regions defined the by maxima on the rupture length plots in Figure 4.8A and Figure 4.9A. The results for typical events for both dimers are shown in Figure 4.10. The left column corresponds to the data for dimer 1 and the right column corresponds to dimer 2. The black lines show the force curves and snapshots of the dimer structures prior to the rupture are indicated above the force curves. Figure 4.10A and B illustrate the dimer dissociation process corresponding to the shortest rupture distance events for dimers 1 and 2, respectively (class I events). The analysis shows that the rupture process for dimer 1 occurs after the partial unraveling of both N-termini region (Figure 4.10A), while the rupture process for dimer 2 occurs as a non-symmetric unraveling of the N-termini with a higher extension of the monomer shown in red (Figure 4.10B).

The asymmetry in the dissociation process is more pronounced in Type II events, and typical results are shown in Figure 4.10C and D for dimers 1 and 2, respectively. During this process, the N-terminal region gradually unfolds; therefore, the total length of the extended N-terminal region (Asp1–Lys16) becomes as long as ~5 nm. The rest of protein remains a compact globule with a diameter of ~2–3 nm. During the dissociation, this core remains compact and stabilized by hydrophobic interactions. The eventual rupture distance is ~8 nm, calculated from the combined length of the extended N-terminal region (Asp1–Lys16; ~5 nm) and the diameter (~3 nm) of the compact cluster. Typically, when the asymmetric unraveling occurs, one monomer maintains the compact

conformation while the other monomer gradually unfolds accompanied by an increase in the Radius of gyration (Rg) (Figure 4.11A**)**.

The dimers dissociation for the longest rupture events (type III rupture processes) for dimers 1 and 2 are illustrated by Figure 4.10E and F, respectively. These events are characterized by the extension of almost the entire Aβ42 protein starting from the N-termini. The dimer at the end of the rupture process is stabilized by interacting hydrophobic segments of the C-termini. During the dissociation process, the unfolding of monomers unfolding is accompanied by the gradual increase in Rg values for both monomers (Figure 4.11B). The total length of the dimer prior to separation is ~12 nm, composed of the length of two extended N-termini (10 nm) and the diameter of the hydrophobic cluster (~2 nm).

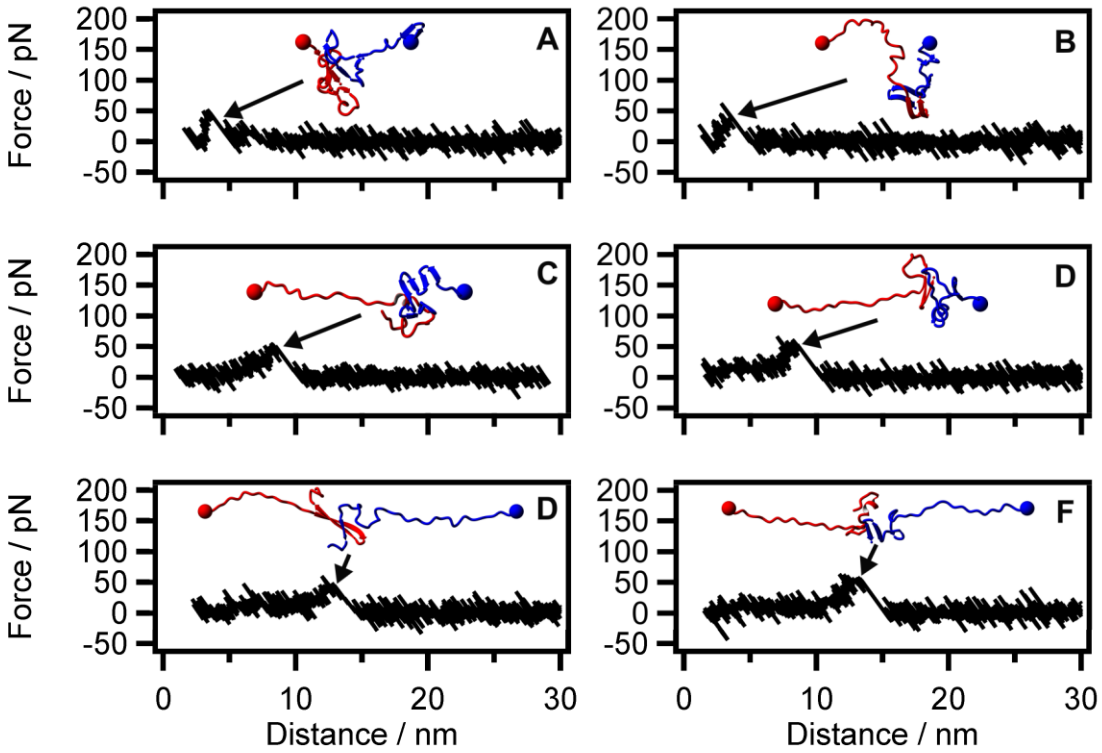

Figure 4.10. The typical rupture events for simulations of dimers dissociation. The force curves (black lines in A-F) are taken from the different pattern regions I-VI (Figure 4.8A and 4.9A), respectively. The snapshots corresponding to the structures prior to the dissociation are indicated with arrows. The monomer color-coding is the same as above. The colored balls represent the N-terminal residues.

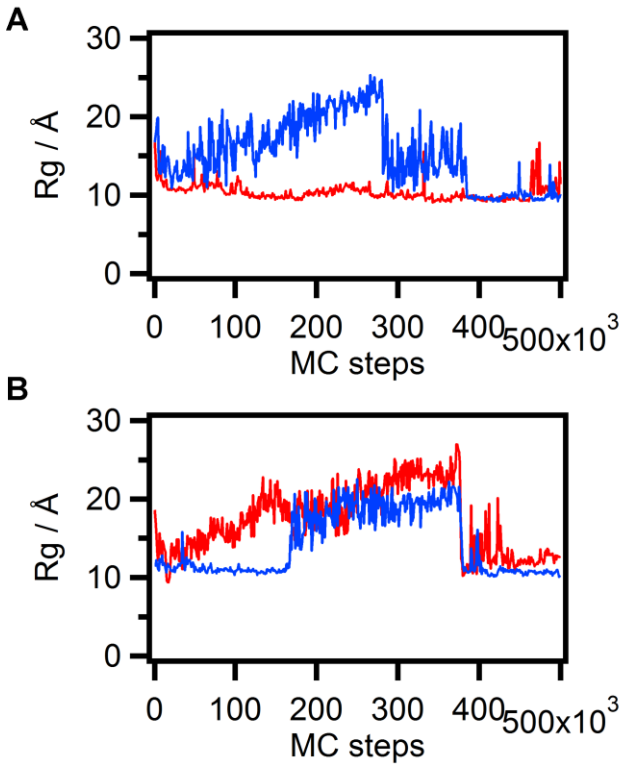

Figure 4.11. The fluctuation of Radius of Gyration (Rg) in the course of asymmetric and symmetric unravelling. (A) Rg fluctuation of the typical asymmetric unravelling process. (B) Rg fluctuation during symmetrically unravelling the dimer. The red line is from monomer A and blue line is used to monitor the changes of monomer B.

In contrast, the dimer structures from U-shaped fibrils [27] and the new emerging S-shaped fibrils [34], termed as U-shaped dimer and S-shaped dimer, respectively (Figure 4.7C,D), demonstrate distinct force-induced pathways in terms of rupture pattern analysis. Strikingly, for U-shaped dimer case, the majority of rupture distances are concentrated at approximately 10 nm (Figure 4.12A), which is explicitly different from the results from dimer 1 and dimer 2 simulations. Moreover, the hairpins on both monomers of the U-shaped dimer are prone to form intermediate species in which shearing processes are predominant in the course of pulling. The rupture force uncovers a strong correlation with the length of adjacent β-strand, as shown in Figure 4.12B and C, associated with the VII and VIII region in Figure 4.12A. In the S-shaped dimer case, the triple β motif and intramolecular salt bridge (Lys28-Ala42) have been observed [34]. Due to the presence of multiple β motifs, the rupture events are a mixture of both asymmetric and symmetric processes (IX, X in Figure 4.13). This complexity of structure contributes to the fact that multiple peaks in the rupture curves are very common (Figure 4.13B,C). Based on the results from the MC pulling experiments, we conclude that the interaction strength of Aβ42 dimers depend on the β content as well as the pattern present in the dimer. Altogether, based on the force induced dissociation, the order of strength in dimers is experiment, dimer 1, dimer 2 < S-shaped dimer < U-shaped dimer. This discrepancy in forces between the U-shaped dimer and experimentally observed values also evidences that the early stage of Aβ42 aggregation does not contain highly ordered high β content conformations.

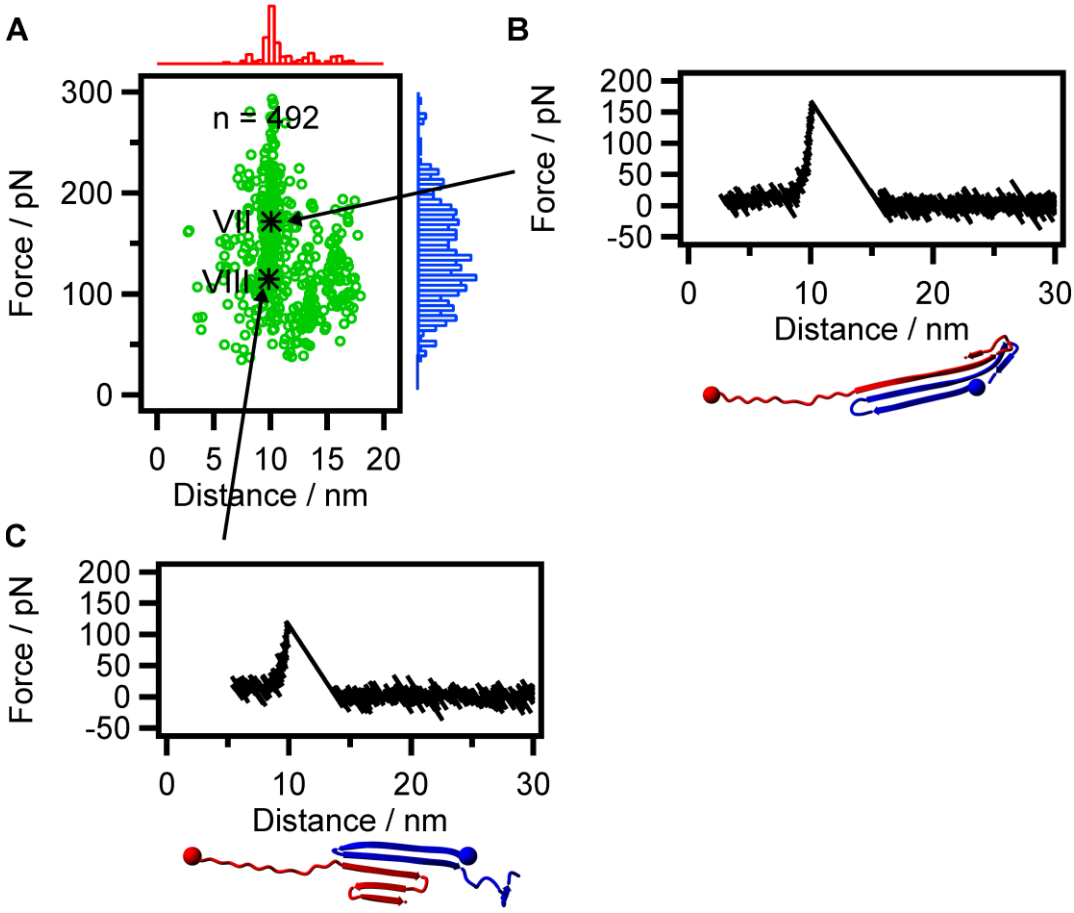

Figure 4.12. The rupture pattern of U-shaped dimers. (A) The distributions of forces (blue) and distances (red) from each simulation are placed on the right side and top side with respect to scatter plots, accordingly. The black * symbols are the centroids from highest density areas of scatter points indicating the different pattern regions, labeled by letters from VII to VIII. (B,C) Two force curves are taken from VII and VIII regions, respectively. The snapshots at the maximum force are put at the bottom of force curve. The red color indicate the monomer A and blue is monomer B. The colorful balls are the N-terminal residues.

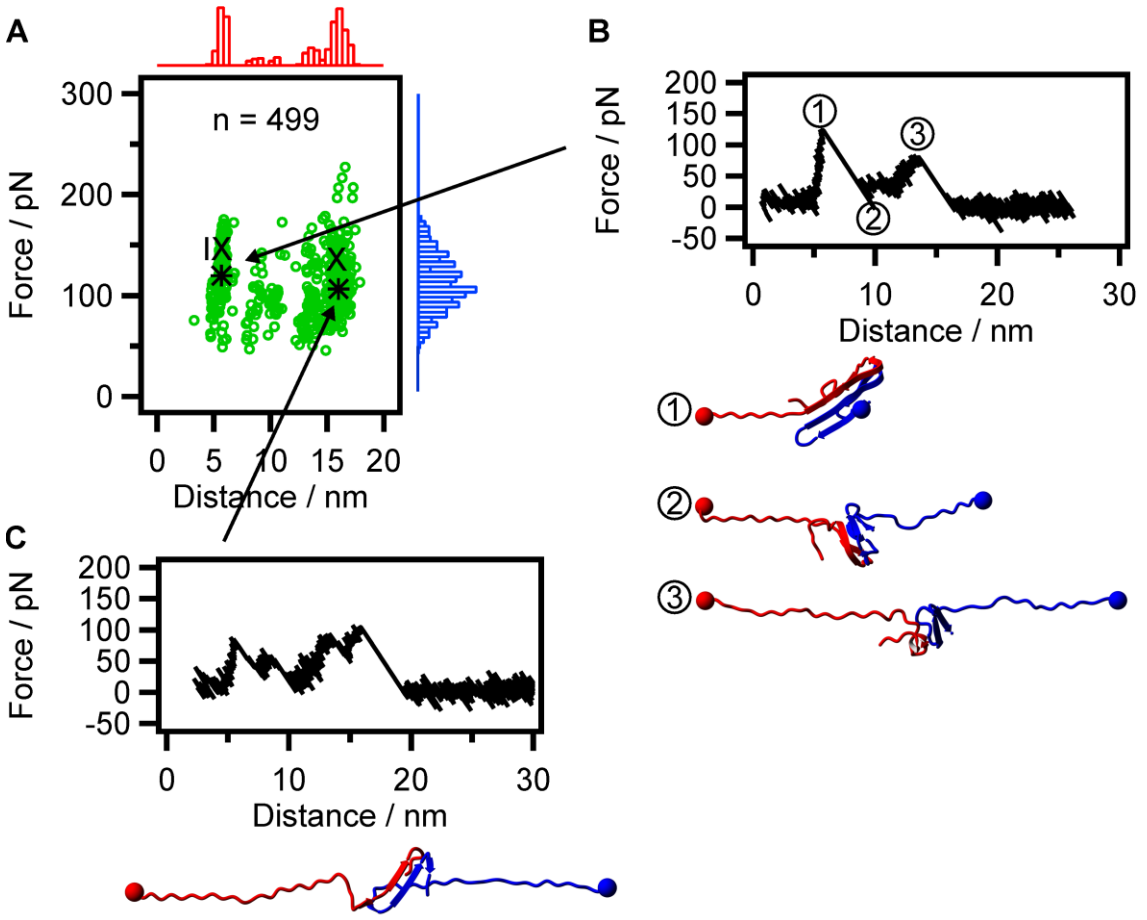

Figure 4.13. The rupture pattern of S-shaped dimers. (A) The scatter plots (green circles) of rupture forces versus distances from MC pulling simulations. The distributions of forces (blue) and distances (red) from each simulation are placed on the right side and top side related to scatter plots, respectively. The black * symbols are the centroids from highest density areas of scatter points representing the different pattern regions, termed as IX and X. (B,C) Two force curves from IX and X regions, respectively. In B, three relevant snapshots around the rupture events (1-3) are extracted and placed underneath the force curve. In C**,** the snapshots at the maximum force are put at the bottom of force curve. The red color indicates the monomer A and blue is monomer B. The colorful balls are the N-terminal residues.

4.4 DISCUSSION

Our comprehensive computer simulation was able to produce the atomic structure of Aβ42 dimers and reveal their dynamic properties. The monomers in their initial equilibrated states are capable of forming dimers that are stabilized primarily by interactions of the central hydrophobic CHC segments (Leu17 through Ala21) as well as the C-terminal regions without the formation of high β content structures (Figure 4.3). Dimer formation is accompanied by conformational changes of monomers with the formation of α-helixes and β-structures (Figure 4.1C), but these are local structural transitions. There is no indication to the formation of extended β-structures as observed in Aβ42 fibrils [27, 32]. Our findings are in agreement with the characterization of early-stage Aβ42 aggregates by CD and ThT fluorescence that show that the oligomers have a low β content [35, 36]. However, the strongest support for the simulated structures of dimers comes from the direct comparison of the AFM pulling results for Aβ42 dimers with the simulations performed at conditions identical to the experimental ones. . Importantly, the comparison was made over large data sets, enabling the comparison of both the mean rupture forces values and the force distributions, as shown in Figure 4.6. Both parameters for the simulations are in a perfect coincidence with experimental results, providing a strong validation of the Aβ42 dimer structures. Moreover, we performed pulling simulations for dimers with extended β structures that are found in fibrils [27, 32]. The rupture force data for these dimers (Figure 4.7) are considerably larger than experimental results, allowing us to rule out the possibility that Aβ42 dimers contain fibril-like structures. The rupture patterns are also dramatically different from simulated

dimers, as shown in Figure 4.12 and 4.13. Therefore, we conclude that isolated Aβ42 monomers can assemble into dimers, but their structure is entirely different from the structure that Aβ42 forms within fibrils.

In fact, the dimers do not adopt well-defined structures; rather the free energy landscapes have sets of local minima as shown in Figure 4.4. The roughness of the free energy landscape suggests that the structures of Aβ42 dimers are very dynamic; therefore, various stable states are probed by monomers. These states cannot be reliably distinguished by the rupture forces, although the minima depths vary. Due to MD sample volumes that restrict the relative motilities of monomers and limit sampling, two different orientations of the monomers were selected in the initial arrangement of the monomers. Given the roughness of the energy landscape and the high dynamics of the dimers, a transition between the two orientations was expected; however, we did not observe this phenomenon. This can be explained by the relatively small cube volume present in simulations in relation to the size of Aβ42 that restricts the range of the translational mobility of the monomer. The volume is defined by the computational resources of the Anton computer, which was close to the limit of the computer. Although two types of dimers were obtained, they have major structural similarities and produce rupture forces with very close values in the MCP simulations. The difference between dimers 1 and 2 was identified by comparing the rupture patterns (Figure 4.8 and 4.9). Interestingly, the dimer 1 rupture pattern fits better with the experimental pattern than dimer 2; therefore we consider dimer 1 as the most appropriate model for Aβ42 dimers.

The existence of multiple energy minima on the energy landscape of the dimers has a number of biological implications. Aggregation of Aβ42 and other amyloids is the process in which aggregates with different morphologies are formed. One model suggests the existence of different aggregation pathways for aggregates with different morphologies [37-43] with the structure specific dimers serving as origins for these pathways. It is widely accepted that oligomers are the most neurotoxic species of amyloids. This is supported by the evidence that Aβ42 dimers are neurotoxic as well [44, 45]. The neurotoxic effect of Aβ42 dimers assumes that dimers interact with a multitude of other proteins and cellular membranes; therefore, the structural plasticity of Aβ42 dimers should facilitate these interactions.

Aβ42 dimerization has been modeled in the past [46-51], and we note the differences between our data and prior computational analyses. In other studies, the various conformations, including α-helix as well as anti-parallel β-sheets, have been identified within dimers. There are two major factors explaining the differences. First, we assembled dimers by using equilibrated monomer structures, which was not performed in any of these publications. Second, our dimers formation was performed on the long-time scale: ~4 μs for the initial conventional MD simulation with the Anton supercomputer, followed by accelerated MD simulation. As a result, a total sampling equivalent to a millisecond simulation timescale was used to analyze Aβ42 dimerization.

MD simulations are widely applied to model various systems, including amyloid aggregates. A major concern in these modeling approaches is the validation of the obtained structure. Comparing simulations with experiments is typically required, but the

selection of the experimentally testable parameter is problematic. To validate our simulated structures, we used the complex stability characterized by the rupture force as a quantitative parameter to compare with the experimentally determined values. The key to our approach is the MCP method, which allows the rupture force for the dimer model to be obtained. Importantly, these data are simulated at conditions identical to those in AFM force spectroscopy experiments [2]. Additionally, we developed and analyzed another validation test in which a different experimental parameter of the AFM force experiment, the rupture pattern, is simulated and compared with the experimental value. The combination of the two validation criteria allowed us to increase the stringency in the selection of the computational models. The proposed approach can be extended to other complexes that can be probed by AFM force spectroscopy experiments.

REFERENCES

[1] Lovas, S., Y. Zhang, J. Yu, and Y. L. Lyubchenko. 2013. Molecular Mechanism of Misfolding and Aggregation of Aβ(13–23). J. Phys. Chem. B. 117:6175-6186.

[2] Zhang, Y., and Yuri L. Lyubchenko. 2014. The Structure of Misfolded Amyloidogenic Dimers: Computational Analysis of Force Spectroscopy Data. Biophys. J. 107:2903-2910.

[3] Shaw, D. E., R. O. Dror, J. K. Salmon, J. P. Grossman, K. M. Mackenzie, J. A. Bank, Y. Cliff, M. M. Deneroff, B. Batson, K. J. Bowers, E. Chow, M. P. Eastwood, D. J. Ierardi, J. L. Klepeis, J. S. Kuskin, R. H. Larson, K. Lindorff-Larsen, P. Maragakis, M. A. Moraes, S. Piana, Y. Shan, and B. Towles. 2009. Millisecond-scale molecular dynamics simulations on Anton. In Proceedings of the Conference on High Performance Computing Networking, Storage and Analysis. ACM, Portland, Oregon. 1-11.

[4] Shaw, D. E., P. Maragakis, K. Lindorff-Larsen, S. Piana, R. O. Dror, M. P. Eastwood, J. A. Bank, J. M. Jumper, J. K. Salmon, Y. Shan, and W. Wriggers. 2010. Atomic-Level Characterization of the Structural Dynamics of Proteins. Science. 330:341-346.

[5] Hess, B., C. Kutzner, D. van der Spoel, and E. Lindahl. 2008. GROMACS 4: Algorithms for Highly Efficient, Load-Balanced, and Scalable Molecular Simulation. J. Chem. Theory Comput. 4:435-447.

[6] Lindorff-Larsen, K., S. Piana, K. Palmo, P. Maragakis, J. L. Klepeis, R. O. Dror, and D. E. Shaw. 2010. Improved side-chain torsion potentials for the Amber ff99SB protein force field. Proteins. 78:1950-1958.

[7] Jorgensen, W. L., J. Chandrasekhar, J. D. Madura, R. W. Impey, and M. L. Klein. 1983. Comparison of simple potential functions for simulating liquid water. J. Chem. Phys. 79:926-935.

[8] Crescenzi, O., S. Tomaselli, R. Guerrini, S. Salvadori, A. M. D'Ursi, P. A. Temussi, and D. Picone. 2002. Solution structure of the Alzheimer amyloid β-peptide (1–42) in an apolar microenvironment. Eur. J. Biochem. 269:5642-5648.

[9] Reddy, G., J. E. Straub, and D. Thirumalai. 2009. Dynamics of locking of peptides onto growing amyloid fibrils. Proc. Natl. Acad. Sci. USA. 106:11948-11953.

[10] Schrödinger Release 2014-4: Desmond Molecular Dynamics System, version 4.0, D. E. Shaw Research, New York, NY, 2014. Maestro-Desmond Interoperability Tools, version 4.0, Schrödinger, New York, NY, 2014.

[11] Kräutler, V., W. F. van Gunsteren, and P. H. Hünenberger. 2001. A fast SHAKE algorithm to solve distance constraint equations for small molecules in molecular dynamics simulations. J. Comput. Chem. 22:501-508.

[12] Martyna, G. J., D. J. Tobias, and M. L. Klein. 1994. Constant pressure molecular dynamics algorithms. The Journal of chemical physics. 101:4177-4189.

[13] Martyna, G. J., M. L. Klein, and M. Tuckerman. 1992. Nosé–Hoover chains: The canonical ensemble via continuous dynamics. The Journal of chemical physics. 97:2635-2643.

[14] Darden, T., D. York, and L. Pedersen. 1993. Particle mesh Ewald: An N·log(N) method for Ewald sums in large systems. J. Chem. Phys. 98:10089-10092.

[15] Texas Advanced Computing Center (TACC). The University of Texas at Austin

[16] Pierce, L. C., R. Salomon-Ferrer, F. d. O. C. Augusto, J. A. McCammon, and R. C. Walker. 2012. Routine Access to Millisecond Time Scale Events with Accelerated Molecular Dynamics. J. Chem. Theory Comput. 8:2997-3002.

[17] Case, D. A. D., T. A.; Cheatham, T. E., III Simmerling, C., J. D. L.; Wang, R. E.; Luo, R.; Walker, R. C.; Zhang, W.; Merz, K., B. H. M.; Roberts, S.; Roitberg, A.; Seabra, G.; Swails, J.; Goetz, A., I. W. W.; Kolossvai, K. F.; Paesani, F.; Vanicek, J.; Wolf, R. M.;, J. W. Liu, X.; Brozell, S.R.; Steinbrecher, T.; Gohlke, H.; Cai, Q.; Ye,, J. H. X.; Wang, M.-J.; Cui, G.; Roe, D.R.; Mathews, D.H.; Seetin,, R. S. M.G.; Salomon-Ferrer, C.; Babin, V.; Luchko, T.; Gusarov,, and A. K. S.; Kovalenko, P. A. . Amber 12; University of California:San Francisco, CA, 2012.

[18] Hamelberg, D., J. Mongan, and J. A. McCammon. 2004. Accelerated molecular dynamics: A promising and efficient simulation method for biomolecules. J. Chem. Phys. 120:11919-11929.

[19] Hamelberg, D., C. A. F. de Oliveira, and J. A. McCammon. 2007. Sampling of slow diffusive conformational transitions with accelerated molecular dynamics. J. Chem. Phys. 127:155102.

[20] Mu, Y., P. H. Nguyen, and G. Stock. 2005. Energy landscape of a small peptide revealed by dihedral angle principal component analysis. Proteins: Structure, Function, and Bioinformatics. 58:45-52.

[21] Brandes, U., and D. Wagner. 2004. Analysis and Visualization of Social Networks. In Graph. Drawing Software. M. Jünger, and P. Mutzel, editors. Springer Berlin Heidelberg. 321-340.

[22] Python Software Foundation. Python Language Reference, version 2.7. Available at http://www.python.org.

[23] Hunter, J. D. 2007. Matplotlib: A 2D Graphics Environment. Comput. Sci. Eng. 9:90-95.

[24] Oliphant, T. E. 2007. Python for Scientific Computing. Comput. Sci. Eng. 9:10-20.

[25] Humphrey, W., A. Dalke, and K. Schulten. 1996. VMD: visual molecular dynamics. J. Mol. Graph. Model. 14:33-38.

[26] Daura, X., K. Gademann, B. Jaun, D. Seebach, W. F. van Gunsteren, and A. E. Mark. 1999. Peptide Folding: When Simulation Meets Experiment. Angew. Chem. Int. Edit. 38:236-240.

[27] Lührs, T., C. Ritter, M. Adrian, D. Riek-Loher, B. Bohrmann, H. Döbeli, D. Schubert, and R. Riek. 2005. 3D structure of Alzheimer's amyloid-β(1–42) fibrils. Proc. Natl. Acad. Sci. USA. 102:17342-17347.

[28] Wereszczynski, J., and J. A. McCammon. 2010. Using Selectively Applied Accelerated Molecular Dynamics to Enhance Free Energy Calculations. J. Chem. Theory Comput. 6:3285-3292.

[29] Wang, Y., C. B. Harrison, K. Schulten, and J. A. McCammon. 2011. Implementation of Accelerated Molecular Dynamics in NAMD. Comput. Sci. Discov. 4:015002.

[30] Jose, J. C., P. Chatterjee, and N. Sengupta. 2014. Cross dimerization of amyloid-beta and alphasynuclein proteins in aqueous environment: a molecular dynamics simulations study. PLoS One. 9:e106883.

[31] Lv, Z., R. Roychaudhuri, M. M. Condron, D. B. Teplow, and Y. L. Lyubchenko. 2013. Mechanism of amyloid beta protein dimerization determined using single-molecule AFM force spectroscopy. Sci. Rep. 3:2880

[32] Xiao, Y., B. Ma, D. McElheny, S. Parthasarathy, F. Long, M. Hoshi, R. Nussinov, and Y. Ishii. 2015. Aβ(1-42) fibril structure illuminates self-recognition and replication of amyloid in Alzheimer's disease. Nature structural & molecular biology. 22:499-505.

[33] Irback, A., and S. Mohanty. 2006. PROFASI: A Monte Carlo simulation package for protein folding and aggregation. J. Comput. Chem. 27:1548-1555.

[34] Xiao, Y., B. Ma, D. McElheny, S. Parthasarathy, F. Long, M. Hoshi, R. Nussinov, and Y. Ishii. 2015. Aβ(1-42) fibril structure illuminates self-recognition and replication of amyloid in Alzheimer's disease. Nat. Struct. Mol. Biol. 22:499–505.

[35] Meisl, G., X. Yang, E. Hellstrand, B. Frohm, J. B. Kirkegaard, S. I. Cohen, C. M. Dobson, S. Linse, and T. P. Knowles. 2014. Differences in nucleation behavior underlie the contrasting aggregation kinetics of the Abeta40 and Abeta42 peptides. Proc. Natl. Acad. Sci. USA. 111:9384-9389.

[36] Ruggeri, F. S., J. Adamcik, J. S. Jeong, H. A. Lashuel, R. Mezzenga, and G. Dietler. 2015. Influence of the beta-sheet content on the mechanical properties of aggregates during amyloid fibrillization. Angew. Chem. 54:2462-2466.

[37] Miller, Y., B. Ma, C.-J. Tsai, and R. Nussinov. 2010. Hollow core of Alzheimer's Aβ42 amyloid observed by cryoEM is relevant at physiological pH. Proc. Natl. Acad. Sci. USA. 107:14128-14133.

[38] Lyubchenko, Y. L. 2013. Nanoimaging for Molecular Pharmaceutics of Alzheimer's and other Neurodegenerative Disorders. J. Mol. Pharm. Org. Process Res. 1:e107.

[39] Huang, D., M. I. Zimmerman, P. K. Martin, A. J. Nix, T. L. Rosenberry, and A. K. Paravastu. 2015. Antiparallel beta-sheet structure within the C-terminal region of 42-residue Alzheimer's beta-amyloid peptides when they form 150 kDa oligomers. J. Mol. Biol. 427:2319-2328.

[40] Stroud, J. C., C. Liu, P. K. Teng, and D. Eisenberg. 2012. Toxic fibrillar oligomers of amyloid-beta have cross-beta structure. Proc. Natl. Acad. Sci. USA. 109:7717-7722.

[41] Laganowsky, A., C. Liu, M. R. Sawaya, J. P. Whitelegge, J. Park, M. Zhao, A. Pensalfini, A. B. Soriaga, M. Landau, P. K. Teng, D. Cascio, C. Glabe, and D. Eisenberg. 2012. Atomic view of a toxic amyloid small oligomer. Science. 335:1228-1231.

[42] Cerf, E., R. Sarroukh, S. Tamamizu-Kato, L. Breydo, S. Derclaye, Y. F. Dufrene, V. Narayanaswami, E. Goormaghtigh, J. M. Ruysschaert, and V. Raussens. 2009. Antiparallel beta-sheet: a signature structure of the oligomeric amyloid beta-peptide. The Biochemical journal. 421:415-423.

[43] Liu, C., M. Zhao, L. Jiang, P.-N. Cheng, J. Park, M. R. Sawaya, A. Pensalfini, D. Gou, A. J. Berk, C. G. Glabe, J. Nowick, and D. Eisenberg. 2012. Out-of-register β-sheets suggest a pathway to toxic amyloid aggregates. Proc. Natl. Acad. Sci. USA. 109:20913-20918.

[44] Shankar, G. M., S. Li, T. H. Mehta, A. Garcia-Munoz, N. E. Shepardson, I. Smith, F. M. Brett, M. A. Farrell, M. J. Rowan, C. A. Lemere, C. M. Regan, D. M. Walsh, B. L. Sabatini, and D. J. Selkoe. 2008. Amyloid-beta protein dimers isolated directly from Alzheimer's brains impair synaptic plasticity and memory. Nat. Med. 14:837-842.

[45] Jin, M., N. Shepardson, T. Yang, G. Chen, D. Walsh, and D. J. Selkoe. 2011. Soluble amyloid beta-protein dimers isolated from Alzheimer cortex directly induce Tau hyperphosphorylation and neuritic degeneration. Proc. Natl. Acad. Sci. USA. 108:5819-5824.

[46] Urbanc, B., L. Cruz, F. Ding, D. Sammond, S. Khare, S. V. Buldyrev, H. E. Stanley, and N. V. Dokholyan. 2004. Molecular dynamics simulation of amyloid beta dimer formation. Biophys. J. 87:2310-2321.

[47] Mitternacht, S., I. Staneva, T. Hard, and A. Irback. 2011. Monte Carlo study of the formation and conformational properties of dimers of Abeta42 variants. J. Mol. Biol. 410:357-367.

[48] Barz, B., and B. Urbanc. 2012. Dimer Formation Enhances Structural Differences between Amyloid β-Protein (1–40) and (1–42): An Explicit-Solvent Molecular Dynamics Study. PLoS One. 7:e34345.

[49] Zhu, X., R. P. Bora, A. Barman, R. Singh, and R. Prabhakar. 2012. Dimerization of the Full-Length Alzheimer Amyloid β-Peptide (Aβ42) in Explicit Aqueous Solution: A Molecular Dynamics Study. J. Phys. Chem. B. 116:4405-4416.

[50] Zhang, T., J. Zhang, P. Derreumaux, and Y. Mu. 2013. Molecular Mechanism of the Inhibition of EGCG on the Alzheimer Aβ1–42 Dimer. J. Phys. Chem. B. 117:3993-4002.

[51] Viet, M. H., P. H. Nguyen, P. Derreumaux, and M. S. Li. 2014. Effect of the English Familial Disease Mutation (H6R) on the Monomers and Dimers of Aβ40 and Aβ42. ACS Chem. Neurosci. 5:646-657.

APPENDIX 4.1. The matlab script example for the analysis of time-dependent dynamics of the β-strand contents

```
%=======================

%Following the method in the paper 'Reddy, G., Straub, J.E. & Thirumalai, D. Dynamics
%of locking of peptides onto growing amyloid fibrils. Proceedings of the National
%Academy of Sciences 106, 11948-11953 (2009).'

%=======================

clc;clear all;

delete('betaintegration.txt')

data=importdata('bcounts.txt');

t=data(:,1)*.01;

probability=data(:,2)/41;

intdata=[];

totalt=t(1:100:end);% using 1 ns as interval

totalp=probability(1:100:end);

for i=1:length(totalt)-1

   intdata1=trapz(totalt(i:i+1),totalp(i:i+1));

   intdata=[intdata, intdata1];

end

intdata=[0,intdata]';

intdata=intdata/1;

hold on;

plot(totalt(2:end),intdata(2:end),'r-');

ylim([0,0.2])

totaldata=[totalt intdata];

save('betaintegration.txt', 'totaldata', '-ASCII')
```

APPENDIX 4.2. The tcl script example for dihedral angle calculation

```
# The original script was provided by Dr. Klaus Schulten's group.
# Modified by Yuliang, Zhang
# Using TK console or vmd -dispdev text -e *.tcl'
   set mol [mol new "dimer_nowater.dms" waitfor all]
   mol addfile "nowater.dcd" molid $mol waitfor all
   set fp [ open "phi-psi.dat" w ]
   set fp2 [ open "phi-psi2.dat" w ]
   set sel [ atomselect $mol "alpha" ]
   set n [ molinfo $mol get numframes ]

   for {set i 0 } { $i < $n } { incr i } {
      $sel frame $i
      $sel update
      set a [ $sel num ]
      for {set j 1 } { $j < [expr $a/2-1] } { incr j } {
         puts -nonewline $fp [format "%.4f %.4f " [lindex [$sel get {phi psi}] $j 0] [lindex
[$sel get {phi psi}] $j 1]]
      }
      puts -nonewline $fp "\n"
   }
    for {set i 0 } { $i < $n } { incr i } {
      $sel frame $i
      $sel update
      set a [ $sel num ]
      for {set j [expr $a/2+1] } { $j < [expr $a-1] } { incr j } {
         puts -nonewline $fp2 [format "%.4f %.4f " [lindex [$sel get {phi psi}] $j 0]
[lindex [$sel get {phi psi}] $j 1]]
```

```
    }
    puts -nonewline $fp2 "\n"
}
$sel delete
close $fp
close $fp2
exit
```

APPENDIX 4.3. The matlab script example for analyzed force curves from MCP simulation

```
%Yuliang Zhang
%Jul,2015, UNMC, Omaha.
function extractForce
clc;
clear all;
tempName='rt-';
first=1;
last=500;
for i=first:last;
    filename=strcat(tempName, num2str(i));
    total=importdata(filename);
    force=total(:,13)*92.1;
    d=total(:,19)./10;
    x=total(:,14)./10;
    y=force;
    pt_end=find(d==max(d(d<30)));
    x=x(1:pt_end);
    y=y(1:pt_end);
    yy1 = smooth(x,y,0.02,'loess');
    [xx,ind] = sort(x);
    smoothyy1= yy1(50:1:end);
    f1d=diff(smoothyy1);
    minf1d=find(f1d==min(f1d));
    maxF1=max(yy1);
    pt1=find(yy1==maxF1);
```

```
    pt2=find(yy1==smoothyy1(minf1d));
    maxyy1=max(yy1(pt2-10:pt2));%find the maximum value of smooth data with diff
    pt=find(yy1==maxyy1);
    maxF=mean(yy1(pt-10:pt));
    maxnoise=20;
    if maxF >maxnoise
    outfilename='force.txt';
    fidout=fopen(outfilename,'at');
    fseek(fidout,1,1);
    fprintf(fidout,'%10f ',i);
    fprintf(fidout,'%10.5f ',d(pt1));
    fprintf(fidout,'%10.5f ',maxF1);
    fprintf(fidout,'%10.5f ',maxyy1);
    fclose(fidout);
    else;
    maxF=[];
    maxBeta=[];
    maxHbnum=[];
    end;
end;
```

Chapter 5

REAL TIME STRUCTURAL DYNAMICS OF WILD TYPE α-SYNUCLEIN

5.1. INTRODUCTION

In previous chapters novel results on characterization of the self-assembly of amyloid peptides and full-size Aβ42 protein were described. In theory, such a combined experimental and computational approach can be applied to any proteins, however, in reality MD simulation is limited by the protein size, so currently analysis of protein with size larger than Aβ42 is limited to relatively short computational time and would not reveal the necessary dynamics information. Here we describe an alternative combined approach where high-speed AFM (HS-AFM) was applied to characterization of dynamics of dimers formed by α-Syn protein (140 amino acids). The self-assembly of α-Syn is associated with Parkinson's disease (PD), which affects approximately millions people in the world [1]. The widely accepted aggregation model considers that fibrillary aggregates of α-Syn can form intracellular Lewy bodies [2], which are the pathological hallmark lesions of PD and causes neurodegeneration. Recently, evidence suggests that small amount of α-Syn can also be secreted from neuronal cells by unconventional exocytosis [3, 4], which may also play a crucial role in neurodegeneration, reviewed in reference [5].

Similar to the other amyloid peptides and proteins, due to intrinsic heterogeneity, it is still not well understood how α-Syn monomers self-assemble into high order

aggregates. Thus, in this chapter, we performed HS-AFM to visualize the structural dynamics of wild type α-Syn protein in real time. The resulting AFM images were interpreted by appropriate computational modeling.

5.2. METHODS

5.2.1. Sample preparation from AFM imaging

A freshly cleaved mica substrate was glued to the glass rods and modified by 167 μM APS for 30 minutes. After rinsing with 20 μl milli-Q water and then with 20 μl PBS buffer, pH 7.4 for three times, 30 nM of Wild-type α-Syn sample in the same buffer were deposited on the mica surface. After 5 minutes of incubation, the surface was rinsed with the same buffer that was used for imaging.

5.2.2. HS-AFM procedure

The HS-AFM images were acquired using the HS-AFM instrument (RIBM, Tsukuba, Japan) developed by the Ando group. BL-AC10DS-A2 cantilevers (Olympus) with carbon tips obtained by electron beam deposition (EBD) method were used for imaging. The EBD carbon tips were grown on the top of silicon nitride AFM tips in the electron beam and were sharpened with the PE 2000 plasma etcher. The spring constant of the AFM probes was between 0.1 and 0.2 N/m, with the resonance frequency between 400 and 1000 kHz in water. Continuous scanning over the selected area (50 nm × 50 nm) with the scan rate is ~ 5 frames / second was performed. The number of pixels for each image was 128 × 128.

The volume of compact structures was calculated through Femtoscan Software. The the stiffness between tails formed on the peptide was identified according to the equation described in [6-9].

$$\langle r^2(l)\rangle_{2D} = 4pl\left[1 - \frac{2p}{l}\left(1 - e^{-l/2p}\right)\right] \qquad (1)$$

where l is the contour length between two points on the strings, r is end to end distance between l. The persistence length (p) represents the stiffness of a macroscopic string structure.

5.2.3. Aggregation propensity

The aggregation propensity was calculated using Zyggregator through the website (http://www-mvsoftware.ch.cam.ac.uk/index.php/zyggregator). If the value was above the line at $Z_{agg}^{prof} = 1$, it was determined as the aggregation-prone regions [10].

5.2.4. Graphic and Modeling Software

All the figures were plotted by Igor Pro. 6.3.4 (WaveMetrics, Lake Oswego, OR, USA). The snapshots were generated by VMD software [11]. The structures were predicted using DMD simulations provided by Dr. Dokholyan's group and MC simulation in PROFASI software package.

The MCP simulations were implemented by using the PROFASI package [12] with the implicit water model and an all-atom FF08 force field [12, 13]. In the PROFASI software package, the bond lengths, bond angles, and peptide torsion angles are assumed to be fixed. The interaction potential consists of the following four terms:

$$E = E_{loc} + E_{ev} + E_{hb} + E_{hp} \quad (2)$$

The E_{loc} term is the backbone potential from the adjacent peptide units along the chain; E_{ev} represents a $1/r^{12}$ repulsion between a pair of atoms; E_{hb} and E_{hp} indicate the hydrogen binding energy and hydrophobic energy, respectively.

5.3. RESULTS

5.3.1. Dynamics of α-synuclein monomers

Rationale. The conventional AFM is a powerful tool to evaluate the α-Syn structure without any need for labeling. However, several limitations are present in the conventional AFM experiment. The first limitation is that such experiments are performed for dried samples condition rather than aqueous condition, resulting in the deformation of samples and possible artifacts in the images obtained, especially in height and volume. Although the experiment can be done in aqueous solution, the scan rate is too low to capture the biological processes on second or milli-second time scale. Usually, acquiring one frame requires 5 min using conventional AFM. Moreover, the radius of tip, used in conventional AFM, is usually larger than 10 nm. Due to tip convolution effect, it is problematic to obtain high-resolution images and achieve high temporal resolution.

To overcome these problems, HS-AFM [8, 14] was selected here. With this technique, the maximum scan rate that can be reached with HS AFM is 16 frames per second allowing one to visualize dynamics of molecules at the millisecond time frame. Additionally, high resolution is made possible using an Electron Beam Deposition (EBD)

tip with radius ranging from 0.5 to 5 nm. The EBD tip not only provides high resolution but also minimizes the tip-sample interaction [15]. To study protein dynamics, HS AFM has recently been successfully applied for the visualization of intrinsically disordered properties of biological samples under aqueous conditions [7, 16].

Dynamics of α-Syn monomers elucidated with HS AFM. Samples of wild-type α-Syn in PBS buffer (pH 7.4) were deposited on mica surfaces and directly visualized by HS-AFM. The experimental details are described in methods section. The HS-AFM results show that the majority (75%) of the monomers assume compact structures (Figure 5.1). Some of the compact structures are of globular shape (diameter, ~5 nm; height, ~2nm) (Figure 5.1A) and remain stable over time without significant structural changes. Other compact structures display one tail (Figure 5.1B) or two tails (Figure 5.1C) with height of ~1 nm (Figure 5.1).

We modeled the α-Syn monomers structures using Monte Carlo (MC) approach. In this approach, all-atom description with implicit water is used for the protein modeling. The bond lengths and bond angles are fixed. The local potential related to electrostatic interaction, energy for hydrogen bonds and hydrophobic interaction are taken into account for the total energy calculation. Comparison with the structural models, obtained from MC simulations, indicate that the tails are comprised of N-C terminal residues, as shown in the Figure 5.1 together with HS-AFM images. A minority of monomers contains extended structures, occupying 25 % of total population (Figure 5.3) that we analyzed separately. The contour lengths of this type of monomer are varied. To further emphasize the length dynamics, we selected one monomer and followed its dynamics analyzing the length of extended regions in different frames. As is shown in Figure 5.4,

the length in the first selected frame is approximately 44.1 nm (Figure 5.4 0 s). It is shorter than the theoretical length (~50 nm) of α-Syn, possibly due to a partially folded region within the peptide chain. After 20 s, terminal parts of the monomer form compact structures, indicated by two peaks (height > 0.9 nm) followed by the decrease in length of the central part to 22.7 nm (frame 21.4 s in Figure 5.4). This structure remains stable for ~160 s, after which the compact region is unraveled and length increases to 38.7 nm (Figure 5.4, frame 180.2 s). We analyzed the stiffness of extended structure using approach described in [6, 7]. This approach characterizes the dynamics of the polymer on the 2D surface. The persistence length estimated in this analysis is 28.6 nm (Figure 5.5), which is 2 folds higher than previously reported for the intrinsically disordered heterodimeric chromatin transcription (FACT) protein with capability of spontaneous stretching on the surface [7]. It is reasonable to assume that the interaction of the protein with the surface contributes to the dynamics of the monomer extension.

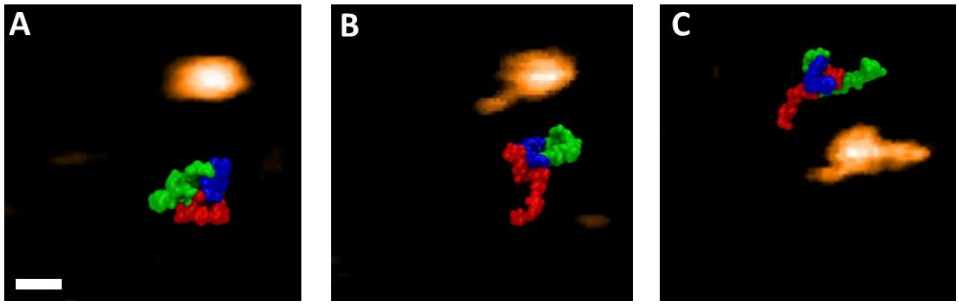

Figure 5.1. HS-AFM of wild-type α-Syn monomer. Three compact monomers: the globular structure (A), one tail structure (B) and two tails structures (C) The scale bar is 5 nm. Selected snapshots of α-Syn are taken from Monte Carlo (MC) simulations corresponding to the images.

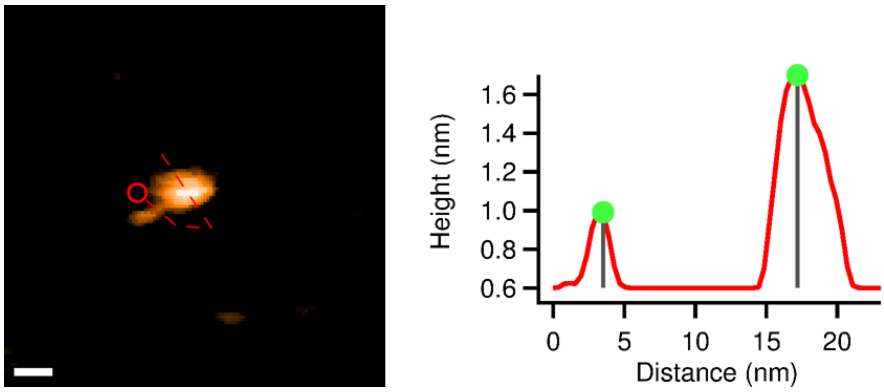

Figure 5.2. The difference between compact region and tail region. The starting point is indicates by red circle and contour length are represented by red dashed line in the image and solid line in the underneath curves, respectively. The green dots are the maximum of peaks.

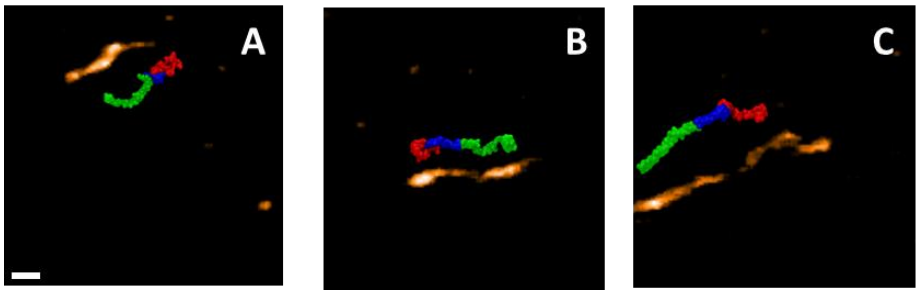

Figure 5.3. Selected extended monomers with different length. The snapshots of α-Syn are taken from MC simulation and put in the relevant images. The scale bar is 5 nm.

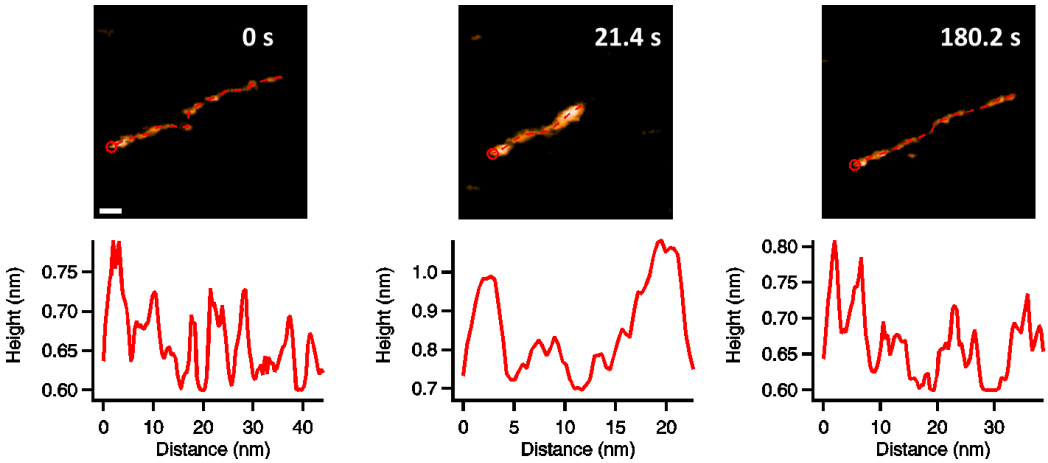

Figure 5.4. The selected frames of length analysis of extended α-Syn monomers. The starting point is indicates by red circle and contour length are represented by red dashed line in the image and solid line in the underneath curves, respectively.

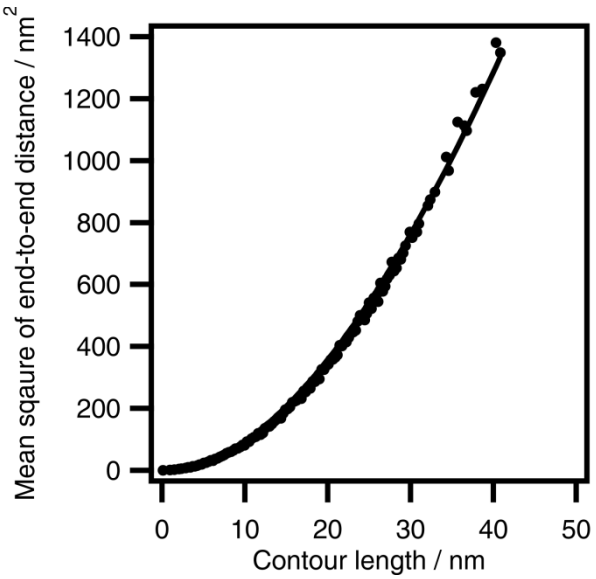

Figure 5.5. The stiffness of extended α-Syn monomer. The black dots are raw data and solid line is fitting curve. The persistence length is 28.6 nm.

The transition from compact structures to extended ones was also visualized and the dataset is shown in Figure 5.6a. These frames indicate the change of monomers conformation over time. Initially globular in shape (Figure 5.6, frame 0 s), the protein adopts one tail structures (Figure 5.6, frame 13.8 s) and fluctuates between globular and one tail structures (Figure 5.6, frames 0 s, 13.8 s, 16.8 s and 26 s). The changes are followed by the formation of two tails (Figure 5.6, frame 27.4 s) and the conversion between the globular and two tails are also observed (Figure 5.6, frames 27.4 s, 33.6 s, 62.6 s and 100.2 s). Afterwards, extended structure with two heads (Figure 5.6, frame 102.2 s) are formed followed by transition between the different length of extended structures (Figure 5.6, frames 125.6 s, 129.6 s, 130.4 s) and two tails structure. Eventually, the monomer adopts an extended structure (Figure 5.6, frames 133.6 s and 161.2 s). Furthermore, the shape of α-Syn monomer in selected frame at 133.6 s (Figure 5.6, frame 132.6 s) shows a similar dynamics for extended structure of other monomers as in Figure 5.3A,B.

To quantitatively describe this dynamics, we measured the time-dependent volume changes of compact region. The volume calculation from specific frames in the whole dataset of Figure 5.6, in which the compact structure can easily be distinguished, is shown in Figure 5.7A. Briefly, the volumes of the compact structures are ~70 nm^3 (Figure 5.7A, 0 s and 19.8 s). When the compact structure partially converts to the tail-like structure, the volume drops to ~60 nm^3 (Figure 5.7A, 62.6 s). With further unraveling of compact structures, the volumes drop to ~20 nm^3 (Figure 5.7A, 97.8 s, 106 s, 112.8 s and 161.2 s). While the tails became shorter, the volume demonstrates a slight increase (Figure 5.7A, 132.6 s). Similar to previous section, 200 structures containing tail

shapes were submitted to stiffness analysis. In Figure 5.7B, the results reveal that the persistence length of tails structure is 2.9 nm, which is smaller than the one from the other IDP proteins [7] as well as the fibrillary structures [9], suggesting that the tail is probably a flexible peptide chain. Conversely, on the grounds of this observation, we can also confirm that the structures in the other images and movies (Figure 5.1) are monomers, if they are similar to the ones in Figure 5.6.

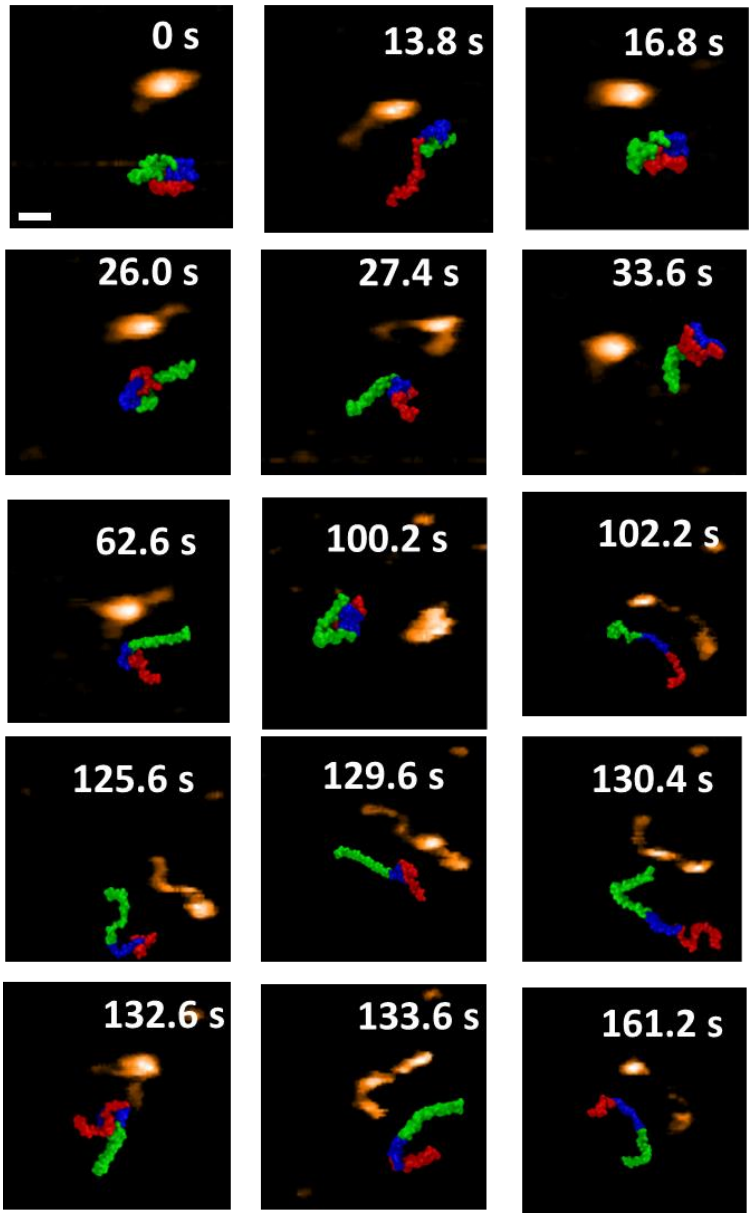

Figure 5.6. The selected frames of the structural transition of α-Syn monomer over scanning time. The globular structures (0 s, 16.8 s and 100.2 s), one tail structures (13.8s, 26.0 s, 33.6 s and 125.6 s), two tails structure (27.4 s, 62.6 s, 129.6 s and 132.6 s) and two heads structure (102.2 s and 161.2) and extended structure (130.4 s and 133.6 s). The snapshots of α-Syn are taken from MC simulation and put in the relevant images. The green color indicates the residues from 1 to 60. The blue color is the NAC region. The red color is residues from 96 to 140. The scale bar is 5 nm.

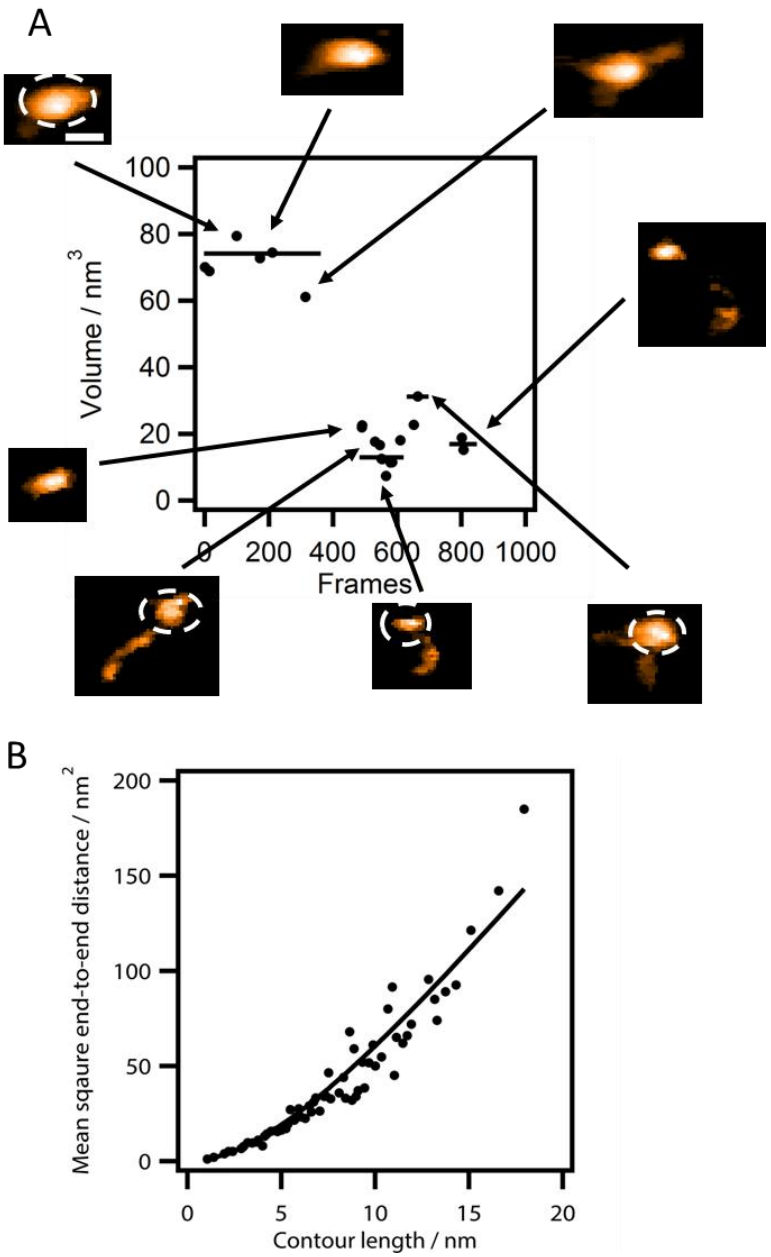

Figure 5.7. The analysis of α-Syn under structural transition. (A) The volume calculation (black dots) and several estimated states (black lines). The images at specific time points are put inset of the figure and dashed circles indicate the pattern for volume analysis. (B) The stiffness of tail-like structure of α-Syn. The black dots are raw data and solid line is fitting curve. The contour length and end to end distance are taken along tail-like structure.

5.3.2. Dynamics and structure of α-Syn dimers

Beside monomers, we also observed some larger oligomers including dimer, trimer and so forth. We characterized the dimers dynamics dividing, them in two types of structures. In the first type of dimer, shown in Figure 5.8, two compact monomers interact with each other and the entire assembly remains stable during the 3.2 s observation period, indicated by the consistent center distance of 7.5 nm. In another type, the dimers contain one monomer with compact shape and another with flexible tail, indicated by fluctuation of total length from ~15 nm to ~25 nm (Figure 5.9). The center distance of 8.4 nm is slightly larger than for the compact dimer. Interestingly, the total length of one monomer fluctuates dramatically. At 0s and 2.6 s from the selected frames, the length is approximately 10 nm. Afterwards, the monomer converts into a compact structure at 2.8 s. Subsequently, the long tail-like structure with length of 17 nm appears at 4 s.

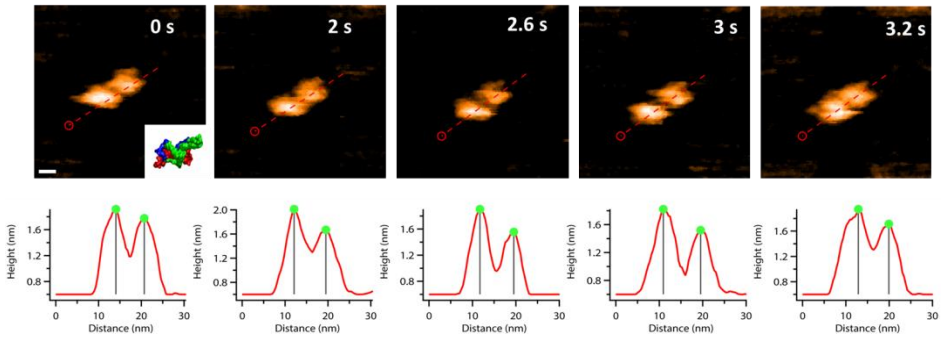

Figure 5.8. HS-AFM of WT α-Syn dimer (compact monomers). The Height and length analysis are under the frames. The snapshot from simulation result is shown in the right low corner in the frames at 0 s.

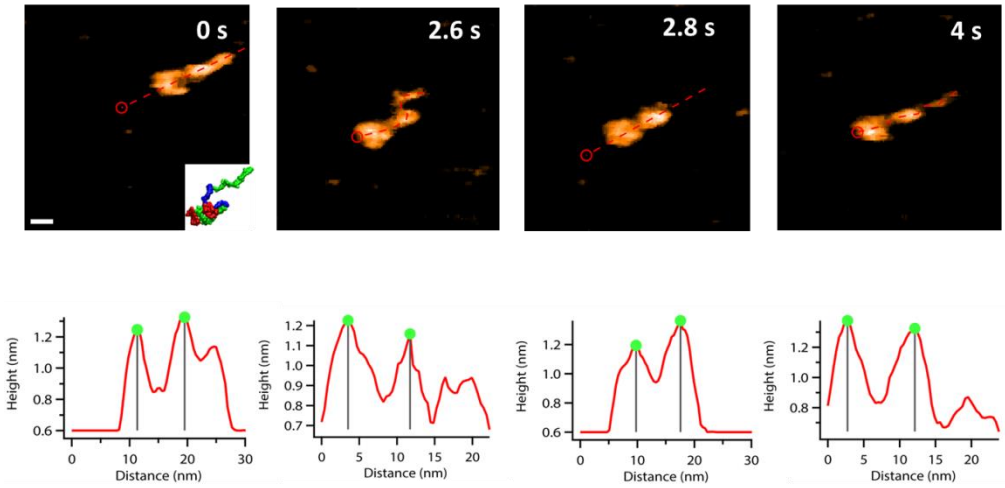

Figure 5.9. HS-AFM of WT α-Syn dimer (one is compact, another is unstructured). The Height and contour length analysis are under the frames. The simulation result shows that one monomer looks like the tail (right low corner in the frames at 0 s).

5.4. DISCUSSION

The comparison of HS-AFM images with MC provides insight into the structural dynamics of α-Syn monomer as well as dimer at nano-scale. Previously the study of 3D structure of α-Syn monomer, in the presence of micelles, suggested that residues 3-37 and 45-92 are prone to form two helical conformations while residues 98-140 are unstructured [17]. In comparison, in absence of binding partners free α-Syn monomer, in solution under physiological conditions, is considered intrinsically unstructured protein [18-20]. Our HS-AFM results demonstrate that the WT α-Syn monomer adopts a compact configuration, which is different from the one in fibrils [21-23]. Similar to our previous chapters, it suggests that the extended β-sheet pattern is not favorable at monomer state. It is instructive to analyze α-Syn primary structure to understand the monomers compaction. There are three regions in α-Syn monomer: region 1, amphipathic α-helices (with repeated KTKEGV motif) from residue 1 to 60; region 2, the hydrophobic and highly amyloidogenic non-Aβ component (NAC) from residues 61 to 95; region 3, highly enriched in acidic residues and prolines, especially from residues 120-140 (8 negative charges) [24]. The former two regions show high aggregation propensities (Figure 5.10) and contain the membrane binding domains [25, 26]. Mutations, A30P, E46K, and A53T, important for the disease development are found in the first region [27-29], altering the structure of α-Syn in different ways [30]. Region 3 participates in the protein-protein interaction. Therefore, based on the HS-AFM images and MC modeling, we speculate that the hydrophobic interaction facilitates the compact monomer formation, seen as the blue region in Figure 10. Indeed, deletion of central

residues from α-Syn can interfere with the fibril formation [31]. The N and C terminal segments are incorporated into the compact structure and we speculate that the long-range electrostatic interaction via the charged residues is responsible for this compaction which is supported by papers [18, 32].

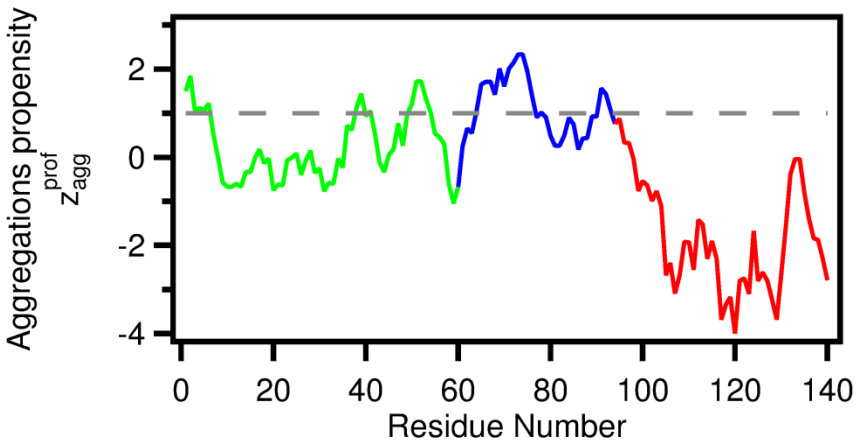

Figure 5.10. Aggregation propensity profile of α-Syn based on Zagg calculation at pH 7. There are three different regions of α-Syn on amino acid sequence level: Green indicates residue 1-60, which contains repeating KTKEGV fragment; Blue is NAC region; Red is charged region. The dashed line at $Z_{agg}^{prof} = 1$ is used to determine the aggregation-prone regions.

Furthermore, the remarkable conversion between compact morphology and the extended one have been observed in both monomer and dimer states. In particular, as shown in Figure 5.6 (monomer case), over long observation period (160 s) the monomer fluctuates between the compact, tail-like structures, and an extended conformation. So far, several studies have proposed to characterize the possibility of intermediate states of α-Syn proteins [23, 33, 34]. Specially, tail-like intermediate structures of α-Syn have been suggested based on MD simulations, EM, and SAXS experiments [35, 36]. It is well known that tail-like structures implicate several biological functions in the intrinsically disordered proteins [37]. Probably, in the absence of lipids, residues within region 1 and region 3 (Figure 5.10) are flexible. On the other hand, the interaction from the termini is not as strong as the hydrophobic interaction from NAC region. Therefore, we infer that the unstructured monomers are prone to form intermediate stage and the frequent structural conversion occurs at the early stage. It is interesting that the compact structures are to some extent stabilized when the dimer is formed (Figure 5.9). The structures are also consistent with the MC simulation, in which the dimers adopt several configurations, shown in the modeling structures in Figures 5.8 and 5.9. Altogether, the variety of monomer and dimer structures can further prove the intrinsic heterogeneity of α-Syn protein that can explain conformational transitions in the course of the aggregation process and formation of highly ordered fibrillar structure.

It is noteworthy that, depending on the interaction type, the dynamics process of α-Syn can be accelerated or retarded in presence of substrate surface instead of in bulk solution. Thus, the observed behavior of α-Syn might be slightly different from actual case, as illustrated in the previous fibril elongation studies via a “stop-and-go”

mechanism [38-40]. The interaction of the protein with the surface can lead to the protein extension retarding the α-Syn fibril elongation. At the same time, other morphologies were observed, so the monomers can move on the surface randomly and also freely convert into several states (Figure 5.6). Interestingly, a few extended monomers were observed attaching to the surface and exhibiting low mobility (Figure 5.3). Herein, we should point out that the scope of current work is not to explore all observed structures and conformations but to evaluate the range of α-Syn dynamics.

In the current study, we use a weakly positively charged APS mica surface as a substrate for HS-AFM samples [41]. On this surface, we were able to visualize a structural dynamics and transitions of monomer as well as dimer (Figures 5.1 and Figure 5.9). The use of surfaces of different types would allow us to evaluate the role of the surface effect on the α-Syn dynamics.

REFERENCES

[1] Huse, D. M., K. Schulman, L. Orsini, J. Castelli-Haley, S. Kennedy, and G. Lenhart. 2005. Burden of illness in Parkinson's disease. Movement Disord. 20:1449-1454.

[2] Spillantini, M. G., M. L. Schmidt, V. M. Y. Lee, J. Q. Trojanowski, R. Jakes, and M. Goedert. 1997. alpha-Synuclein in Lewy bodies. Nature. 388:839-840.

[3] Jang, A., H. J. Lee, J. E. Suk, J. W. Jung, K. P. Kim, and S. J. Lee. 2010. Non-classical exocytosis of alpha-synuclein is sensitive to folding states and promoted under stress conditions. J. Neurochem. 113:1263-1274.

[4] Lee, H. J., S. Patel, and S. J. Lee. 2005. Intravesicular localization and exocytosis of alpha-synuclein and its aggregates. J. Neurosci. 25:6016-6024.

[5] Lee, H. J., E. J. Bae, and S. J. Lee. 2014. Extracellular alpha-synuclein-a novel and crucial factor in Lewy body diseases. Nat. Rev. Neurol. 10:92-98.

[6] Rivetti, C., M. Guthold, and C. Bustamante. 1996. Scanning Force Microscopy of DNA Deposited onto Mica: EquilibrationversusKinetic Trapping Studied by Statistical Polymer Chain Analysis. J. Mol. Biol. 264:919-932.

[7] Miyagi, A., Y. Tsunaka, T. Uchihashi, K. Mayanagi, S. Hirose, K. Morikawa, and T. Ando. 2008. Visualization of intrinsically disordered regions of proteins by high-speed atomic force microscopy. Chemphyschem. 9:1859-1866.

[8] Ando, T., and N. Kodera. 2012. Visualization of mobility by atomic force microscopy. Methods Mol. Biol. 896:57-69.

[9] Lamour, G., C. K. Yip, H. Li, and J. Gsponer. 2014. High Intrinsic Mechanical Flexibility of Mouse Prion Nanofibrils Revealed by Measurements of Axial and Radial Young's Moduli. ACS Nano. 8:3851–3861.

[10] Pawar, A. P., K. F. DuBay, J. Zurdo, F. Chiti, M. Vendruscolo, and C. M. Dobson. 2005. Prediction of "Aggregation-prone" and "Aggregation-susceptible" Regions in Proteins Associated with Neurodegenerative Diseases. J. Mol. Biol. 350:379-392.

[11] Humphrey, W., A. Dalke, and K. Schulten. 1996. VMD: visual molecular dynamics. J. Mol. Graph. Model. 14:33-38.

[12] Irback, A., and S. Mohanty. 2006. PROFASI: A Monte Carlo simulation package for protein folding and aggregation. J. Comput. Chem. 27:1548-1555.

[13] Jonsson, S. A. E., S. Mitternacht, and A. Irback. 2013. Mechanical resistance in unstructured proteins. Biophys. J. 104:2725-2732.

[14] Ando, T., T. Uchihashi, N. Kodera, D. Yamamoto, M. Taniguchi, A. Miyagi, and H. Yamashita. 2007. High-speed atomic force microscopy for observing dynamic biomolecular processes. J. Mol. Recognit. 20:448-458.

[15] Ando, T., T. Uchihashi, and N. Kodera. 2013. High-Speed AFM and Applications to Biomolecular Systems. Annu. Rev. Biophys. 42:393-414.

[16] Hashimoto, M., N. Kodera, Y. Tsunaka, M. Oda, M. Tanimoto, T. Ando, K. Morikawa, and S. Tate. 2013. Phosphorylation-coupled intramolecular dynamics of unstructured regions in chromatin remodeler FACT. Biophys. J. 104:2222-2234.

[17] Ulmer, T. S., A. Bax, N. B. Cole, and R. L. Nussbaum. 2005. Structure and dynamics of micelle-bound human alpha-synuclein. J. Biol. Chem. 280:9595-9603.

[18] Dedmon, M. M., K. Lindorff-Larsen, J. Christodoulou, M. Vendruscolo, and C. M. Dobson. 2005. Mapping long-range interactions in alpha-synuclein using spin-label NMR and ensemble molecular dynamics simulations. J. Am. Chem. Soc. 127:476-477.

[19] Bernadó, P., C. W. Bertoncini, C. Griesinger, M. Zweckstetter, and M. Blackledge. 2005. Defining Long-Range Order and Local Disorder in Native α-Synuclein Using Residual Dipolar Couplings. J. Am. Chem. Soc. 127:17968-17969.

[20] Eliezer, D., E. Kutluay, R. Bussell, Jr., and G. Browne. 2001. Conformational properties of alpha-synuclein in its free and lipid-associated states. J. Mol. Biol. 307:1061-1073.

[21] Vilar, M., H.-T. Chou, T. Lührs, S. K. Maji, D. Riek-Loher, R. Verel, G. Manning, H. Stahlberg, and R. Riek. 2008. The fold of α-synuclein fibrils. Proc. Natl. Acad. Sci. USA. 105:8637-8642.

[22] Heise, H., W. Hoyer, S. Becker, O. C. Andronesi, D. Riedel, and M. Baldus. 2005. Molecular-level secondary structure, polymorphism, and dynamics of full-length α-synuclein fibrils studied by solid-state NMR. Proc. Natl. Acad. Sci. USA. 102:15871-15876.

[23] Uversky, V. N., J. Li, and A. L. Fink. 2001. Evidence for a partially folded intermediate in alpha-synuclein fibril formation. J. Biol. Chem. 276:10737-10744.

[24] Breydo, L., J. W. Wu, and V. N. Uversky. 2012. Alpha-synuclein misfolding and Parkinson's disease. BBA-Mol. Basis Dis. 1822:261-285.

[25] Fusco, G., A. De Simone, T. Gopinath, V. Vostrikov, M. Vendruscolo, C. M. Dobson, and G. Veglia. 2014. Direct observation of the three regions in α-synuclein that determine its membrane-bound behaviour. Nat. Commun. 5:3827.

[26] Braun, A. R., M. M. Lacy, V. C. Ducas, E. Rhoades, and J. N. Sachs. 2014. α-Synuclein-Induced Membrane Remodeling Is Driven by Binding Affinity, Partition Depth, and Interleaflet Order Asymmetry. J. Am. Chem. Soc. 136:9962-9972.

[27] Zarranz, J. J., J. Alegre, J. C. Gómez-Esteban, E. Lezcano, R. Ros, I. Ampuero, L. Vidal, J. Hoenicka, O. Rodriguez, B. Atarés, V. Llorens, E. G. Tortosa, T. del Ser, D. G. Muñoz, and J. G. de Yebenes. 2004. The new mutation, E46K, of α-synuclein causes parkinson and Lewy body dementia. Ann. Neurol. 55:164-173.

[28] Kruger, R., W. Kuhn, T. Muller, D. Woitalla, M. Graeber, S. Kosel, H. Przuntek, J. T. Epplen, L. Schols, and O. Riess. 1998. Ala30Pro mutation in the gene encoding alpha-synuclein in Parkinson's disease. Nat. Genet. 18:106-108.

[29] Polymeropoulos, M. H., C. Lavedan, E. Leroy, S. E. Ide, A. Dehejia, A. Dutra, B. Pike, H. Root, J. Rubenstein, R. Boyer, E. S. Stenroos, S. Chandrasekharappa, A. Athanassiadou, T. Papapetropoulos, W. G. Johnson, A. M. Lazzarini, R. C. Duvoisin, G. Di Iorio, L. I. Golbe, and R. L. Nussbaum. 1997. Mutation in the alpha-synuclein gene identified in families with Parkinson's disease. Science. 276:2045-2047.

[30] Auluck, P. K., G. Caraveo, and S. Lindquist. 2010. alpha-Synuclein: membrane interactions and toxicity in Parkinson's disease. Annu. Rev. Cell Dev. Biol. 26:211-233.

[31] Giasson, B. I., I. V. J. Murray, J. Q. Trojanowski, and V. M.-Y. Lee. 2001. A Hydrophobic Stretch of 12 Amino Acid Residues in the Middle of α-Synuclein Is Essential for Filament Assembly. J. Biol. Chem. 276:2380-2386.

[32] Bertoncini, C. W., Y.-S. Jung, C. O. Fernandez, W. Hoyer, C. Griesinger, T. M. Jovin, and M. Zweckstetter. 2005. Release of long-range tertiary interactions potentiates

aggregation of natively unstructured α-synuclein. Proc. Natl. Acad. Sci. USA. 102:1430-1435.

[33] Comellas, G., L. R. Lemkau, D. H. Zhou, J. M. George, and C. M. Rienstra. 2012. Structural Intermediates during α-Synuclein Fibrillogenesis on Phospholipid Vesicles. J. Am. Chem. Soc. 134:5090-5099.

[34] Zhao, M., D. Cascio, M. R. Sawaya, and D. Eisenberg. 2011. Structures of segments of alpha-synuclein fused to maltose-binding protein suggest intermediate states during amyloid formation. Protein Sci. 20:996-1004.

[35] Lorenzen, N., S. B. Nielsen, A. K. Buell, J. D. Kaspersen, P. Arosio, B. S. Vad, W. Paslawski, G. Christiansen, Z. Valnickova-Hansen, M. Andreasen, J. J. Enghild, J. S. Pedersen, C. M. Dobson, T. P. Knowles, and D. E. Otzen. 2014. The role of stable alpha-synuclein oligomers in the molecular events underlying amyloid formation. J. Am. Chem. Soc. 136:3859–3868.

[36] Tsigelny, I. F., Y. Sharikov, W. Wrasidlo, T. Gonzalez, P. A. Desplats, L. Crews, B. Spencer, and E. Masliah. 2012. Role of α-synuclein penetration into the membrane in the mechanisms of oligomer pore formation. FEBS J. 279:1000-1013.

[37] Uversky, V. N. 2013. The most important thing is the tail: Multitudinous functionalities of intrinsically disordered protein termini. FEBS Lett. 587:1891-1901.

[38] Wördehoff, M. M., O. Bannach, H. Shaykhalishahi, A. Kulawik, S. Schiefer, D. Willbold, W. Hoyer, and E. Birkmann. 2015. Single Fibril Growth Kinetics of α-Synuclein. J. Mol. Biol. 427:1428-1435.

[39] Pinotsi, D., A. K. Buell, C. Galvagnion, C. M. Dobson, G. S. Kaminski Schierle, and C. F. Kaminski. 2014. Direct Observation of Heterogeneous Amyloid Fibril Growth Kinetics via Two-Color Super-Resolution Microscopy. Nano Lett. 14:339-345.

[40] Hoyer, W., D. Cherny, V. Subramaniam, and T. M. Jovin. 2004. Rapid Self-assembly of α-Synuclein Observed by In Situ Atomic Force Microscopy. J. Mol. Biol. 340:127-139.

[41] Lyubchenko, Y., A. Gall, and L. Shlyakhtenko. 2014. Visualization of DNA and Protein–DNA Complexes with Atomic Force Microscopy. In Electron Microscopy. J. Kuo, editor. Humana Press. 367-384.

Chapter 6

CONCLUSIONS

The research described above has a number of significant contributions for understanding the molecular mechanism of the initial self-assembly of amyloid proteins. One of these contributions is the deciphering of the structure and dynamics of amyloid dimers which are the first oligomeric species along the self-assembly pathway. The biomedical significance of the studies of oligomers can be seen in the fact that amyloid oligomers including dimers rather than fibrils are the most neurotoxic species [1-6]. There has been growing interest surrounding peptide self-assembly in fibrillar aggregates for use in the designing of biomaterials for various biomedical applications such as tissue regeneration. Understanding the assembly process with structural characterization of transient species is critical for the success of these applications. So far the structural data are available for amyloid proteins and peptide structure in fibrils, however the use of this structural information for designing oligomers is not well justified. Moreover, research has been done that suggests that this is not the case and that the structure of amyloids in oligomers can be different from that seen in fibrils [7-11]. The transient existence of oligomers is one of the most complicating factors surrounding these studies, presenting a need for non-traditional approaches. The research presented here describes the use of such approaches and new results emerging from these studies.

We first observed that the dimers assembly follows a path unlike that which has been predicted based on the amyloid structures found in fibrils. We discovered that even short amyloid peptides do not assemble as a β-structure array as they found in fibrils for Aβ(14-23) or crystals for Sup35 heptapeptide. This information was later useful in the designing of drugs that targeted the dimers. The computational data suggests that the structure of dimers is of a dynamic nature and it further allowed us to characterize the range of dimer conformations. The information provided by these studies proved critical in the characterization of the full-size Aβ42 proteins, which was found to have no structural similarity in its fibril form to that of the dimeric species. This conclusion was confirmed by direct computational analyses of Aβ42 protein structures in fibrils and validation of the simulation results by experimental AFM probing data. Given the fact that Aβ42 dimers are neurotoxic species that are desirable targets for the drug design studies, the information we obtained for the Aβ42 dimers is of great significance. The structural information of Aβ42 dimers and their dynamics is important for the understanding of the Aβ42 self-assembly process. We hypothesize that stable conformations of the dimer play roles of origins for different aggregation pathways and this hypothesis will be tested in our future studies.

Along accomplishing this work, we developed a number of novel approaches and validation tests for the most significant simulated structures. Indeed, the computational analyses including various types of MD simulations are widely used in structural analysis of numerous biological systems and the question of rigorous testing of computational results is the most critical one. The comparison of results by MD with those found in experiment is the only way to truly compare the validity of the study, however the

transient nature of amyloid dimers made such a comparison almost impossible. An approach in which such characteristics of dimer stability is tangibly compared is through the analysis of data obtained with AFM force spectroscopy experiments. The developed MCP approach described in this dissertation is adjusted to the conditions of the AFM experiment, which allows one to validate the dimers structure based on the rupture force value, the major characteristic of the AFM experiment. As a result, a number of simulated structures were rejected and the most suitable ones were identified. Moreover, we extended the MCP approach using another experimental parameter, rupture length as additional validation criteria. As a result, the set of Aβ42 dimers conformations was further narrowed. Although we applied the developed validation approach to simulations of dimers, there is no limit to applying it to other types of complexes probed with AFM force spectroscopy, so we anticipate a wider use of this technique.

The use of High-speed AFM (HS-AFM) made the direct imaging of α-synuclein monomers and dimers an attainable feat which proved very successful in our studies. This novel imaging instrumentation has a number of advantages over regular time-lapse AFM which made many of these findings possible. Although the α-syn monomer is considered to be an intrinsically disordered protein, the range of structural dynamics was found to be very high, which was evident through the discovery of full stretching of this protein. The dynamics of the dimers were also found to be quite large, but less than that of the monomers, which falls closely in line with measurements made in AFM force spectroscopy experiments. The novel component of these studies is the computational modeling of AFM images of α-syn that allowed us to identify interaction regions of the

protein. These studies set the foundation for more rigorous modeling which was done in collaboration with Dr. N. Dokholyan from UNC.

Overall, the studies described in this thesis provid a novel understanding of the very early stages of assembly of Aβ42 and a number of amyloid peptides and proteins. They led to the development of novel approaches and together with the obtained results made a foundation for the next step in elucidation of the oligomerization process. We believe that such studies will eventually lead to understanding of the entire self-assembly process and molecular mechanism of development of neurodegenerative disorders associated with aggregation of specific amyloid proteins.

Prospects

Deregulation of the self-assembly process of proteins, as well as failure of cells to metabolize protein aggregates, results in amyloid formation and is associated with a wide range of human diseases, termed *protein misfolding (deposition) disorders.* Such disorders include Alzheimer's disease (AD), Parkinson's disease (PD), and Huntington's disease, as well as systemic and localized amyloidosis, and transmissible encephalopathies. Still, a fundamental lack of knowledge on the protein self-assembly process impedes progress in the treatment of these diseases. Fortunately, as a result of studies included in this thesis, we advance the knowledge on the mechanism of amyloid assembly and specifically identified the structure of transient dimeric spices. Combined experimental and computational studies led us to model the early stages of protein aggregation, in which interaction between monomers is the key to the formation of aggregation-prone misfolded states of proteins.

Our long-term goal is to unravel molecular mechanisms of the self-assembly of proteins into the disease-prone nano-oligomers. *Our ultimate goal* is to translate this knowledge for preventive and therapeutic purposes as understanding the fundamental mechanisms of protein misfolding and aggregation will guide the development of approaches to control the aggregation process. A couple of potential avenues are described below.

1. *The rational strategy for drug development.* Our model for dimers provides atomic-level details for interaction of monomers. Inhibition of these interactions will be therapeutic strategy aimed to prevention of the dimer formation and hence other toxic oligomeric species. Over past decade, the evidence has turned out several compounds can be considered as potential inhibitors to reduce the neurotoxicity of amyloid proteins. For instance, epigallocatechin-3-gallate (EGCG), a natural compound extracted from green tea, can directly bind to the unfolded amyloid polypeptides to inhibit the formation of toxic intermediates [12]. Upon the binding of EGCG, the hydrophobic interaction of amyloid protein substantially decreased along with reducing of β content [13, 14]. The synthetic compound, 1,4-naphthoquinon-2-yl-$_{L}$-tryptophan (NQTrp), can also provide amazing inhibition of neurotoxicity towards cultured neuronal cell line and transgenic Alzheimer's disease *Drosophila* model [15]. The computational studies also revealed that NQTrp tends to bind the hydrophobic regions of amyloid protein [16]. By taking advantage of the described approaches, the interaction strength within amyloid monomers in presence of these small-molecule drugs can be easily detected. With the development of the force field of various compounds, the interaction strength of different compounds can be determined via our novel validation methods as well. Additionally, with

comparison of the complex consisting of amyloid protein and different compounds, our approaches can be taken as potential screen method to rank the new compound.

2. *Elucidation the mechanism of interaction between amyloid protein and membrane.* In current project, we proposed models for α-Syn dimers. These dimers are in the interaction with the surface. Therefore, extension of such studies for dimers complexes with membrane surfaces is another potential for future studies. As described in Chapter 1, a plausible mechanism of neurotoxicity induced by amyloid protein is interaction with membrane phospholipids or receptor on cell membrane [17-21]. A monomeric α-Syn protein tends to adopt a partially folded structure with transition from a random coil to α-helix in the presence of membrane [22-25]. The N-terminal residues serve as anchors in these interactions with membranes. At the same time, the central region determines the membrane binding affinity whereas the C-terminal region shows weak binding propensity [26]. The self-assembly from monomer to dimer and to high order oligomers is accelerated upon the binding to membrane [27]. Although the high order oligomers within cell membranes have been identified by EM and MD simulations [28-30], the structural dynamics of α-Syn protein remains unclear. Hence, combined computational and experimental studies will enable us to obtain the dynamics process of α-Syn oligomer in the presence of membrane. Therefore, investigation of the interaction between amyloid oligomers and membrane will shed much needed light on intervening into this pathogenic pathway of PD and other neurodegenerative diseases.

REFERENCES

[1] Glabe, C. G. 2006. Common mechanisms of amyloid oligomer pathogenesis in degenerative disease. Neurobiol. Aging. 27:570-575.

[2] Glabe, C. G. 2008. Structural Classification of Toxic Amyloid Oligomers. J. Biol. Chem. 283:29639-29643.

[3] Ono, K., M. M. Condron, and D. B. Teplow. 2009. Structure–neurotoxicity relationships of amyloid β-protein oligomers. Proc. Natl. Acad. Sci. USA. 106:14745-14750.

[4] Tomic, J. L., A. Pensalfini, E. Head, and C. G. Glabe. 2009. Soluble fibrillar oligomer levels are elevated in Alzheimer's disease brain and correlate with cognitive dysfunction. Neurobiol. Dis. 35:352-358.

[5] Yu, L., R. Edalji, J. E. Harlan, T. F. Holzman, A. P. Lopez, B. Labkovsky, H. Hillen, S. Barghorn, U. Ebert, P. L. Richardson, L. Miesbauer, L. Solomon, D. Bartley, K. Walter, R. W. Johnson, P. J. Hajduk, and E. T. Olejniczak. 2009. Structural Characterization of a Soluble Amyloid β-Peptide Oligomer. Biochemistry. 48:1870-1877.

[6] Laganowsky, A., C. Liu, M. R. Sawaya, J. P. Whitelegge, J. Park, M. Zhao, A. Pensalfini, A. B. Soriaga, M. Landau, P. K. Teng, D. Cascio, C. Glabe, and D. Eisenberg. 2012. Atomic view of a toxic amyloid small oligomer. Science. 335:1228-1231.

[7] Xiao, Y., B. Ma, D. McElheny, S. Parthasarathy, F. Long, M. Hoshi, R. Nussinov, and Y. Ishii. 2015. Aβ(1-42) fibril structure illuminates self-recognition and replication of amyloid in Alzheimer's disease. Nat. Struct. Mol. Biol. 22:499–505.

[8] Lührs, T., C. Ritter, M. Adrian, D. Riek-Loher, B. Bohrmann, H. Döbeli, D. Schubert, and R. Riek. 2005. 3D structure of Alzheimer's amyloid-β(1–42) fibrils. Proc. Natl. Acad. Sci. USA. 102:17342-17347.

[9] Tjernberg, L. O., D. J. Callaway, A. Tjernberg, S. Hahne, C. Lilliehöök, L. Terenius, J. Thyberg, and C. Nordstedt. 1999. A molecular model of Alzheimer amyloid beta-peptide fibril formation. J. Biol. Chem. 274:12619-12625.

[10] Petkova, A. T., W. M. Yau, and R. Tycko. 2006. Experimental constraints on quaternary structure in Alzheimer's beta-amyloid fibrils. Biochemistry. 45:498-512.

[11] Uversky, V. N., J. Li, and A. L. Fink. 2001. Evidence for a partially folded intermediate in alpha-synuclein fibril formation. J. Biol. Chem. 276:10737-10744.

[12] Ehrnhoefer, D. E., J. Bieschke, A. Boeddrich, M. Herbst, L. Masino, R. Lurz, S. Engemann, A. Pastore, and E. E. Wanker. 2008. EGCG redirects amyloidogenic polypeptides into unstructured, off-pathway oligomers. Nat. Struct. Mol. Biol. 15:558-566.

[13] Nguyen, P., and P. Derreumaux. 2014. Understanding Amyloid Fibril Nucleation and Aβ Oligomer/Drug Interactions from Computer Simulations. Acc. Chem. Res. 47:603-611.

[14] Zhang, T., J. Zhang, P. Derreumaux, and Y. Mu. 2013. Molecular Mechanism of the Inhibition of EGCG on the Alzheimer Aβ1–42 Dimer. J. Phys. Chem. B. 117:3993-4002.

[15] Scherzer-Attali, R., R. Pellarin, M. Convertino, A. Frydman-Marom, N. Egoz-Matia, S. Peled, M. Levy-Sakin, D. E. Shalev, A. Caflisch, E. Gazit, and D. Segal. 2010. Complete Phenotypic Recovery of an Alzheimer's Disease Model by a Quinone-Tryptophan Hybrid Aggregation Inhibitor. PLoS One. 5:e11101.

[16] Zhang, T., W. Xu, Y. Mu, and P. Derreumaux. 2014. Atomic and Dynamic Insights into the Beneficial Effect of the 1,4-Naphthoquinon-2-yl-l-tryptophan Inhibitor on Alzheimer's Aβ1–42 Dimer in Terms of Aggregation and Toxicity. ACS Chem. Neurosci. 5:148-159.

[17] Mucke, L., and D. J. Selkoe. 2012. Neurotoxicity of Amyloid β-Protein: Synaptic and Network Dysfunction. CSH Perspect. Med. 2:a006338.

[18] Snyder, E. M., Y. Nong, C. G. Almeida, S. Paul, T. Moran, E. Y. Choi, A. C. Nairn, M. W. Salter, P. J. Lombroso, G. K. Gouras, and P. Greengard. 2005. Regulation of NMDA receptor trafficking by amyloid β. Nat. Neurosci. 8:1051-1058.

[19] Sakono, M., and T. Zako. 2010. Amyloid oligomers: formation and toxicity of Abeta oligomers. FEBS J. 277:1348-1358.

[20] Bodner, C. R., A. S. Maltsev, C. M. Dobson, and A. Bax. 2009. Differential Phospholipid Binding of α-Synuclein Variants Implicated in Parkinson's Disease Revealed by Solution NMR Spectroscopy. Biochemistry. 49:862-871.

[21] Lorenzen, N., L. Lemminger, J. N. Pedersen, S. B. Nielsen, and D. E. Otzen. 2014. The N-terminus of alpha-synuclein is essential for both monomeric and oligomeric interactions with membranes. FEBS Lett. 588:497-502.

[22] Lokappa, S. B., J.-E. Suk, A. Balasubramanian, S. Samanta, A. J. Situ, and T. S. Ulmer. 2014. Sequence and Membrane Determinants of the Random Coil–Helix Transition of α-Synuclein. J. Mol. Biol. 426:2130-2144.

[23] Maltsev, A. S., J. Ying, and A. Bax. 2012. Impact of N-Terminal Acetylation of α-Synuclein on Its Random Coil and Lipid Binding Properties. Biochemistry. 51:5004-5013.

[24] Auluck, P. K., G. Caraveo, and S. Lindquist. 2010. alpha-Synuclein: membrane interactions and toxicity in Parkinson's disease. Annu. Rev. Cell Dev. Biol. 26:211-233.

[25] Davidson, W. S., A. Jonas, D. F. Clayton, and J. M. George. 1998. Stabilization of α-Synuclein Secondary Structure upon Binding to Synthetic Membranes. J. Biol. Chem. 273:9443-9449.

[26] Fusco, G., A. De Simone, T. Gopinath, V. Vostrikov, M. Vendruscolo, C. M. Dobson, and G. Veglia. 2014. Direct observation of the three regions in α-synuclein that determine its membrane-bound behaviour. Nat. Commun. 5:3827.

[27] Perrin, R. J., W. S. Woods, D. F. Clayton, and J. M. George. 2001. Exposure to Long Chain Polyunsaturated Fatty Acids Triggers Rapid Multimerization of Synucleins. J. Biol. Chem. 276:41958-41962.

[28] Jiang, Z., M. de Messieres, and J. C. Lee. 2013. Membrane Remodeling by alpha-Synuclein and Effects on Amyloid Formation. J. Am. Chem. Soc. 135:15970-15973.

[29] Tsigelny, I. F., P. Bar-On, Y. Sharikov, L. Crews, M. Hashimoto, M. A. Miller, S. H. Keller, O. Platoshyn, J. X. J. Yuan, and E. Masliah. 2007. Dynamics of α-synuclein aggregation and inhibition of pore-like oligomer development by β-synuclein. FEBS J. 274:1862-1877.

[30] Tsigelny, I. F., Y. Sharikov, W. Wrasidlo, T. Gonzalez, P. A. Desplats, L. Crews, B. Spencer, and E. Masliah. 2012. Role of α-synuclein penetration into the membrane in the mechanisms of oligomer pore formation. FEBS J. 279:1000-1013.